Diego Misseroni

EXPERIMENTAL MODELS OF
ELASTIC STRUCTURES:
TENSILE BUCKLING AND ESHELBY-LIKE FORCES

December, 2013

Diego Misseroni

Experimental Models of Elastic Structures: Tensile Buckling and Eshelby-Like Forces

Advisor: Prof. Davide Bigoni
Co-Advisor: Dr. Francesco Dal Corso

2013

UNIVERSITY OF TRENTO

Engineering of Civil and Mechanical Structural Systems

XXVI cycle

Ph.D. Program Head: Prof. Davide Bigoni

Final Examination: December 9, 2013

Alla mia famiglia.

Summary

Mechanical models have been invented, designed and realized to experimentally confirm unexpected behaviours theoretically predicted in elasticity:

- instabilities and bifurcations occurring in structures under 'tensile dead load' and the influence of the constraint's curvature;

- the presence of an 'Eshelby-like' or 'configurational' force in structures with movable constraints.

Furthermore, 'classical' features in elasticity have been substantied by testing small-scale models and observing:

- linearity in the mechanical response of a truss-structure, confirming the usual assumption of linear elasticity when small displacements are considered;

- stress singular fields near stiff quadrilateral inclusions embedded in a 'soft' elastic plate, validating the model of rigid inclusion.

All the experiments have been performed at the Laboratory for Physical Modeling of Structures and Photoelasticity of the Department of Civil, Environmental and Mechanical Engineering of the University of Trento.

Acknowledgements

First and foremost, I would like to express my gratitude to Professor Davide Bigoni for the constant and fundamental encouragements, suggestions and support gave me throughout this research work.

I am also deeply grateful to Dr. Francesco Dal Corso for the help, encouragements, patience and motivation on both an academic and personal level at all times.

Furthermore, I am highly thankful to Dr. Giovanni Noselli and Federico Bosi for the constructive feedback and their cooperation.

Moreover, I would like to thank Luca Argani for the friendship.

I would also like to thank all members of the Solid and Structural Mechanics Group at the University of Trento, as well as the teams of the Mechanical and Electronic Services.

Last but not the least, I would like to thank my family for their constant support during these years.

Trento, October 25, 2013
Diego Misseroni

Published papers

The main results presented in this thesis have been summarized in the following papers:

1. Zaccaria, D., Bigoni, D., Noselli, G., and Misseroni, D.
   Structures buckling under tensile dead load. *Proceedings of the Royal Society A*, 2011, 467, 1686-1700;

2. Bigoni, D., Misseroni, D., Noselli, G., and Zaccaria, D.
   Effects of the constraintŠs curvature on structural instability: tensile buckling and multiple bifurcations. *Proceedings of the Royal Society A*, 2012, 468, 2191-2209;

3. Bigoni, D., Misseroni, D., Noselli, G., and Zaccaria, D.
   Surprising instabilities of simple elastic structures. Chapter in the book: *Nonlinear Physical Systems - Spectral Analysis, Stability and Bifurcations - BIRS Workshop* , 2013, *in press*;

4. Bigoni, D., Bosi, F., Dal Corso, F., and Misseroni, D.
   Eshelby-like forces acting on elastic structures: theoretical and experimental proof. *Mechanics of Materials*, 2013, *accepted*;

5. Bigoni, D., Bosi, F., Dal Corso, F., and Misseroni, D.
   Instability of a penetrating blade. 2013, *submitted*;

6. Bigoni, D., Dal Corso, F., Misseroni, D., and Tommasini, M.
   A teaching model for truss structures. *European Journal of Physics*, 2012, 33, 1179-1186.

7. Misseroni, D., Dal Corso, F., Shahzad, S., Bigoni, D.
   Stress concentration near stiff inclusions: validation of rigid inclusion model and boundary layers by means of photoelasticity.
   http://arxiv.org/abs/1309.1091, 2013.

Contents

Introduction

Validation of a theoretical model through experiments is a fundamental step for the mechanical description of materials and structures. In this thesis unexpected features (tensile buckling load, Chapter 1- 2, and Eshelby-like force, Chapter 3- 4) of simple mechanical elastic systems are derived and confirmed by experimental tests on small-scale models, and experimental evidence of 'classical' features in elasticity (linear elastic assumption for truss structures, Chapter 5, and singular stress near stiff polygonal inclusions, Chapter 6) is presented.

In Chapter 1 it is shown both theoretically and experimentally that it is possible to design structures that exhibit bifurcations and instabilities under tensile dead load without any compressed elements, see Fig. 1. This behavior is possible in elementary structures with a single degree of freedom and in more complex mechanical systems, as related to the presence of a structural junction, called 'slider', allowing only relative transversal displacement between the connected elements. In continuous systems, where the slider connects two elastic thin rods, bifurcations occur both in tension and compression.

In Chapter 2 it is shown that bifurcation of an elastic structure crucially depends on the curvature of the constraints against which the ends of the structure are prescribed to move, see Fig. 2. These simple structures exhibit interesting features: tensile buckling, designed postcritical behaviour and multiple bifurcations, determining for instance two bifurca-
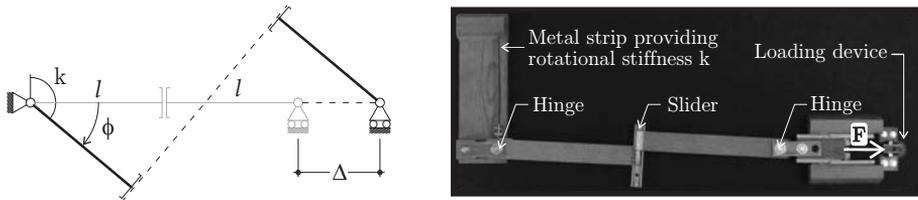
Fig. 1: A scheme (on the left) and a real model (on the right) of a single-degree-of-freedom elastic structure exhibiting bifurcation for tensile dead loading. The rods of length l are rigid and jointed together through a slider, a device allowing only for relative sliding between the two connected pieces). A rotational elastic spring of stiffness k, attached at the hinge on the left, provides the elastic stiffness to the system.

tion loads (one tensile and one compressive) in a single-degree-of-freedom elastic system.
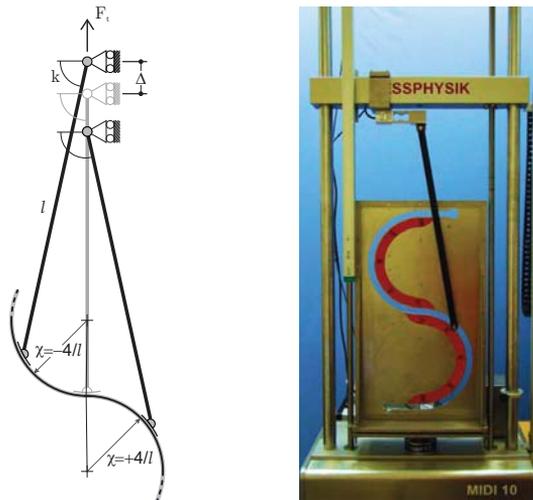
Fig. 2: A scheme (on the left) and a real model (on the right) of a one-degree-of-freedom structure (with a rotational elastic spring at its left end) evidencing compressive or tensile buckling as a function of the curvature of the constraint (a circular profile with constant curvature, $\chi = \pm 4/l$) on which the hinge on the right of the structure is constrained to slide.

In Chapter 3 it is shown that in an elastic structure as sketched in

Fig. 3, where a (smooth and bilateral) constraint leaves the elastic rod the possibility of sliding thus releasing energy, an 'Eshelby-like' or 'configurational' force is generated. This unexpected force (generated by a special movable constraint) is derived analytically and experimentally measured on a model structure that we have designed, realized and tested.
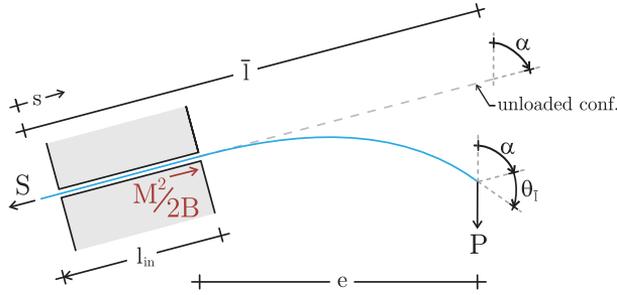
Fig. 3: Structural scheme of the elastic system employed to disclose a Eshelby-like force. The elastic rod of total length $\bar{l}$ is subject to a dead vertical load P on its right end, is constrained with an inclined sliding sleeve and has a axial dead force S applied at its left end. The presence of the Eshelby-like force $M^2/(2B)$ influences the force S at equilibrium, which results different from $P\cos\alpha$.

Chapter 4 is devoted to the stability of an elastic rod penetrating into a sliding sleeve ending with a linear elastic spring. This simple elastic system, sketched Fig. 4, shows several unexpected behaviours including a finite number of buckling loads for a system with infinite degrees of freedom (leading to a non-standard Sturm-Liouville problem), more than one bifurcation loads associated to each bifurcation mode, a restabilization of the straight configuration after the second bifurcation load associated to the first instability mode and the presence of an Eshelby-like (or configurational) force, deeply influencing stability.

A classroom demonstration model for a Warren truss structure (see Fig. 5) is shown in Chapter 5. Our aim is to develop a teaching model to facilitate understanding of the mechanics of truss structures, in which struts are subject to purely axial load and deformation. The demonstration model has been proved to exemplify the way a truss structure is designed and deforms, and have been used during undergraduate class to experimentally assess the validity of structural modeling via linear elastic-

3
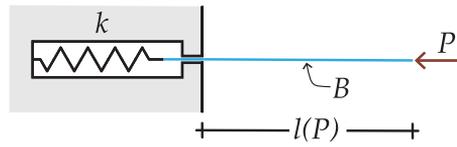
Fig. 4: The penetrating blade is an elastic rod whose free length l is a function of the applied axial load P. The blade has a free end subject to the dead load P, while at the other edge the blade slides into a frictionless sleeve and is restrained by an axial linear spring.

ity.
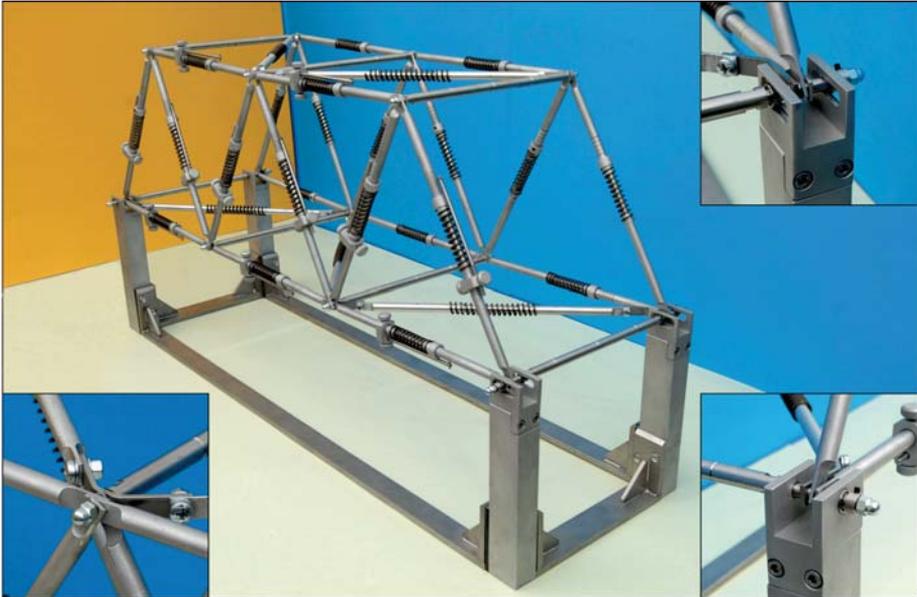
Fig. 5: View of the (unloaded) spatial Warren truss model, with details (an internal node on the left, two external nodes on the right: a roller and a hinge).

Finally, photoelastic investigations of the stress state near stiff quadrilateral inclusions embedded in a 'soft' elastic plate are provided in Chapter 6. These experiments confirm the theoretical singular stress field up to a distance so close to the inclusion edges that fringes become unreadable

4

(even with the aid of an optical microscope), as shown in Fig. 6.
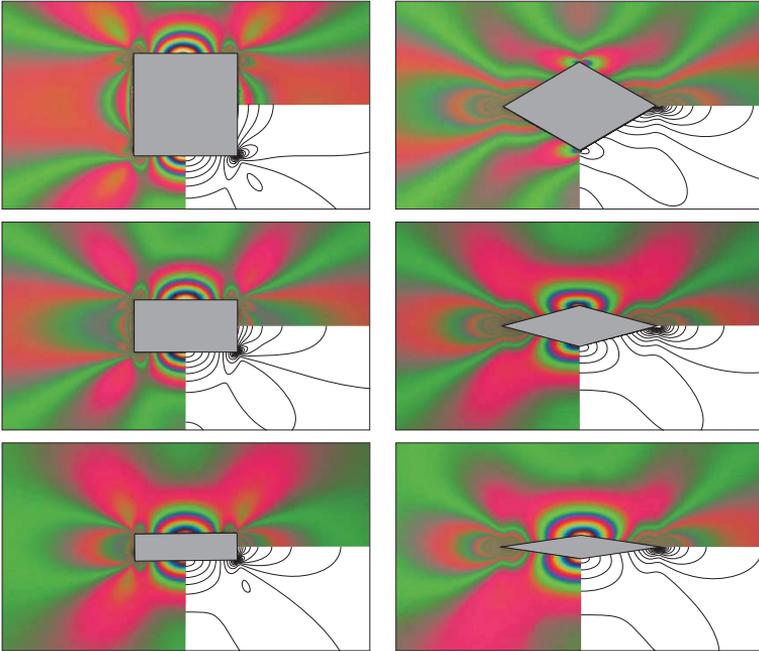
Fig. 6: Photoelastic fringes revealing the stress field near stiff (made up of polycarbonate, Young modulus 2350 MPa) rectangular (large edge $l_x =$20 mm, edges aspect ratios 1, 1/2, 1/4) and rhombohedral (large axis $l_x =$30 mm, axis aspect ratios 2/15, 4/15, 9/15) inclusions embedded in an elastic matrix (a two-component epoxy resin, Young modulus 22 MPa, approximatively 100 times less stiff than the inclusions) and loaded with uniaxial tensile stress $\sigma_{xx}^{\infty} =$0.28 MPa, compared to the elastic solution for rigid inclusions (in plane stress, with Poisson's ratio equal to 0.49).

All the experiments have been performed at the Laboratory for Physical Modeling of Structures and Photoelasticity of the Department of Mechanical and Structural Engineering of the University of Trento.

1

Structures buckling under tensile dead load

After the systematic experiments by Musschenbroek and their rationalization by Euler, for the first time it is shown that it is possible to design structures (i.e. mechanical systems whose elements are governed by the equations of the elastica) exhibiting bifurcations and instabilities ('buckling') under tensile load of constant direction and point of application ('dead'). It is shown both theoretically and experimentally that the behaviour is possible in elementary structures with a single degree of freedom and in more complex mechanical systems, as related to the presence of a structural junction, called 'slider', allowing only relative transversal displacement between the connected elements. In continuous systems where the slider connects two elastic thin rods, bifurcations occur both in tension and compression and are governed by the equation of the elastica, employed here for tensile loading, so that the deformed rods take the form of the capillary curve in a liquid, which is in fact governed by the equation of the elastica under tension. Since axial load in structural elements deeply influences dynamics, our results may provide application to innovative actuators for mechanical wave control, moreover, they open a new perspective in the understanding of failure within structural elements.

Buckling of a straight elastic column subject to *compressive* end thrust occurs at a critical load for which the straight configuration of the column becomes unstable and simultaneously ceases to be the unique solution of the elastic problem (so that instability and bifurcation are concomitant phenomena). Buckling is known from ancient times: it has been experimentally investigated in a systematic way by Pieter van Musschenbrok (1692-1761) and mathematically solved by Leonhard Euler (1707-1783), who derived the differential equation governing the behaviour of a thin elastic rod suffering a large bending, the so-called 'elastica' (see Love,

1927).
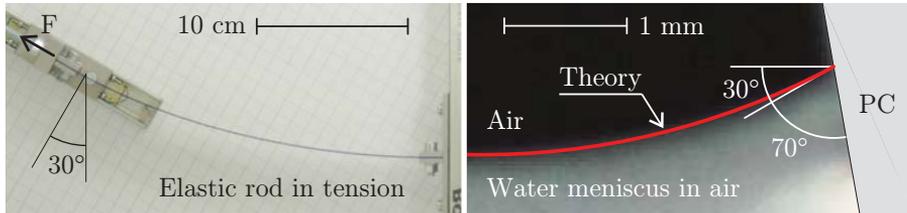
Fig. 1.1: Analogy between an elastic rod buckled under tensile force (left) and a water meniscus in a capillary channel (right, superimposed to the solution of the elastica, marked in red): the deflection of the rod and the surface of the liquid have the same shape, see Section 1.3.

Through centuries, engineers have experimented and calculated complex structures, such as frames, plates and cylinders, manifesting instabilities and bifurcations of various forms (Timoshenko and Gere, 1961), so that certain instabilities have been found involving tensile loads. For instance, there are examples classified by Ziegler (1977) as 'buckling by tension' where a tensile loading is applied to a system in which a compressed member is always present, so that they do not represent true bifurcations under tensile loads. Other examples given by Gajewski and Palej (1974) are all related to the complex *live* (as opposed to 'dead') loading system, for instance, loading through a vessel filled with a liquid, so that Zyczkowski (1991) points out that 'With Eulerian behaviour of loading (materially fixed point of application, direction fixed in space), the bar cannot lose stability at all [...].' Note finally that necking of a circular bar represents a bifurcation of a material element under tension, not of a structure.

It can be concluded that until now *structures made up of line elements (each governed by the equation of the elastica) exhibiting bifurcation and instability under tensile load of fixed direction and point of application (in other words 'dead') have never been found*, so that the word 'buckling' is commonly associated to compressive loads.

In the present chapter we show that:

- simple structures can be designed evidencing bifurcation (buckling)

and instability under tensile dead loading;

- the deformed shapes of these structures can be calculated using the equation of the elastica, but under tension, so that the deflection of the rod is identical to the shape of a capillary curve in a liquid, which is governed by the same equation, see Fig. 1.1 and Sections 1.2.2 and 1.3;

- experiments show that elastic structures buckling under tension can be realized in practice and that they closely follow theory predictions, Sections 1.1 and 1.3.

The above findings are complemented by a series of minor new results for which our system behaves differently from other systems made up of elastic rods, but with the usual end conditions. First, our system evidences load decrease with increase of axial displacement (the so-called 'softening'), second, the bifurcated paths involving relative displacement at the slider terminate at an unloaded limit configuration, for both tension and compression.

We will see that the above results follow from a novel use of a junction between mechanical parts, namely, a *slider* or, in other words, a connection allowing only relative sliding (transverse displacement) between the connected pieces and therefore constraining the relative rotation and axial displacement to remain null.

Vibrations of structures are deeply influenced by axial load, so that the speed of flexural waves vanishes at bifurcation (Bigoni *et al.* 2008; Gei *et al.* 2009), a feature also evidenced by the dynamical analysis presented in Section 1.2.1, so that, since bifurcation is shown to occur in our structures both in tension and compression, these can be used as two-way actuators for mechanical waves, where the axial force controls the speed of the waves traversing the structure. Therefore, the mechanical systems invented here can immediately be generalized and employed to design complex mechanical systems exhibiting bifurcations in tension and compression, to be used, for instance, as systems with specially designed vibrational properties (a movie providing a simple illustration of the concepts exposed in this work, together with a view of experimental results, available at http://ssmg.unitn.it).

1.1 A simple one d.o.f. structure which buckles for tensile dead loading

The best way to understand how a structure can bifurcate under tensile dead loading is to consider the elementary single-degree-of-freedom structure shown in Fig. 1.2, where two rigid rods are connected through a 'slider' (a device which imposes the same rotation angle and axial displacement to the two connected pieces, but null shear transmission, leaving only the possibility of relative sliding). Bifurcation load and equilibrium
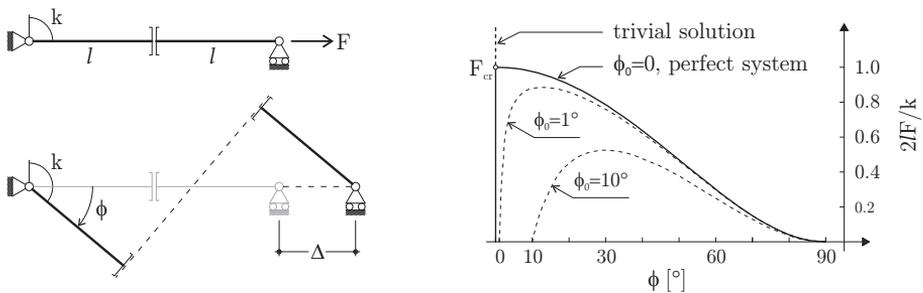
Fig. 1.2: Bifurcation of a single-degree-of-freedom elastic system under *tensile dead loading* (the rods of length l are rigid and jointed through a slider, a device allowing only for relative sliding between the two connected pieces). A rotational elastic spring of stiffness k, attached at the hinge on the left, provides the elastic stiffness. Note that the bifurcation is 'purely geometrical' and is related to the presence of the constraint at the middle of the beam which transmits rotation, but not shear (left). The bifurcation diagram, showing bifurcation and softening in tension is reported on the right. The rotation angle $\phi_0 = \{1°, 10°\}$ denotes an initial imperfection, in terms of an initial inclination of the two rods with respect to the horizontal direction.

paths of this single-degree-of-freedom structure can be calculated by considering the bifurcation mode illustrated in Fig. 1.2 and defined by the rotation angle ϕ. The elongation of the system and the potential energy are respectively

$$\Delta = 2l \left(\frac{1}{\cos \phi} - 1 \right) \tag{1.1}$$

and

$$W(\phi) = \frac{1}{2}k\phi^2 - 2Fl \left(\frac{1}{\cos \phi} - 1 \right), \tag{1.2}$$

10

so that solutions of the equilibrium problem are

$$F = \frac{k\,\phi\,\cos^2\phi}{2l\sin\phi},$$
(1.3)

for $\phi \neq 0$, plus the trivial solution ($\phi = 0$, $\forall F$). Analysis of the second-order derivative of the strain energy reveals that the trivial solution is stable up to the critical load

$$F_{cr} = \frac{k}{2l},$$
(1.4)

while the nontrivial path, *evidencing softening*, is unstable.
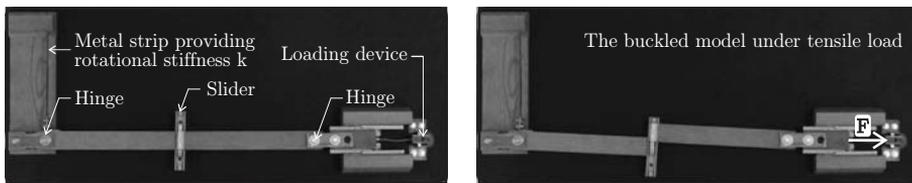
Fig. 1.3: A model of the single-degree-of-freedom elastic structure shown in Fig. 1.2 on the left (in which a metal strip reproduces the rotational spring and the load is given through hanging a load) displaying bifurcation for tensile dead loading (left: undeformed configuration; right: buckled configuration).

For an imperfect system, characterized by an initial inclination of the rods ϕ_0, we obtain

$$W(\phi, \phi_0) = \frac{1}{2}k\,(\phi - \phi_0)^2 - 2Fl\left(\frac{1}{\cos\phi} - \frac{1}{\cos\phi_0}\right)$$
(1.5)

and

$$F = \frac{k\,(\phi - \phi_0)\,\cos^2\phi}{2l\sin\phi},$$
(1.6)

so that the force–rotation relation is obtained, which is reported dashed in Fig. 1.2 for $\phi_0 = 1°$ and $\phi_0 = 10°$.

The simple structure presented in Fig. 1.2, showing possibility of a bifurcation under dead load in tension and displaying an overall softening behaviour, can be realized in practice, as shown by the wooden model

reported in Fig. 1.3.

A further example of a structure buckling in tension is the single-single-degree-of-freedom system shown in Fig. 1.4, where two rigid rods are connected through a roller constrained to slide orthogonally to the left rod.
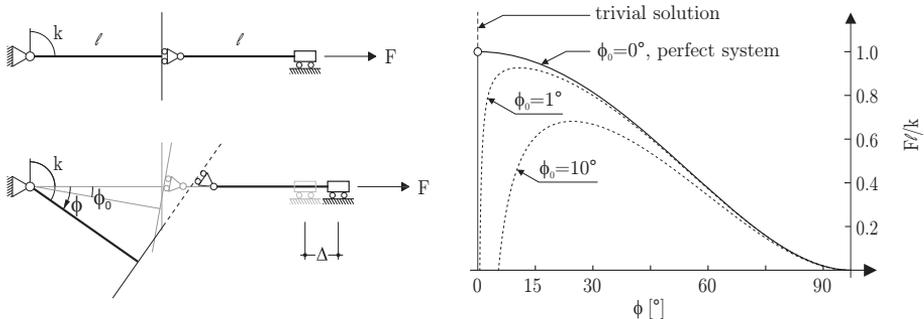

Figure 1.4: Bifurcation of a single-degree-of-freedom elastic system under *tensile dead loading* (the rods of length *l* are rigid and connected through a roller constrained to smoothly slide along the line orthogonal to the rigid rod on the left). A rotational elastic spring of stiffness *k*, attached at the hinge on the left, provides the elastic stiffness. The bifurcation diagram, showing bifurcation and softening in tension is reported on the right, where the angle $\phi_0 = \{1°, 10°\}$ denotes an initial imperfection.

For this structure, bifurcation load and equilibrium paths can be calculated by considering the bifurcation mode illustrated in Fig. 1.4 and defined by the rotation angle ϕ. The elongation of the system and the total potential energy are respectively

$$\Delta = l \left(\frac{1}{\cos \phi} - 1 \right), \quad W(\phi) = \frac{1}{2} k \phi^2 - Fl \left(\frac{1}{\cos \phi} - 1 \right), \qquad (1.7)$$

so that the force at equilibrium satisfies

$$F = \frac{k \phi \cos^2 \phi}{l \sin \phi}. \qquad (1.8)$$

Analysis of the second-order derivative of the strain energy reveals that the trivial solution is stable up to the critical load $F_{cr} = k/l$, while the nontrivial path, *evidencing softening*, is unstable. For an imperfect system,

characterized by an initial inclination of the rods ϕ_0, we obtain

$$W(\phi, \phi_0) = \frac{1}{2} k \, (\phi - \phi_0)^2 - Fl \left(\frac{1}{\cos \phi} - \frac{1}{\cos \phi_0} \right), \quad F = \frac{k \, (\phi - \phi_0) \cos^2 \phi}{l \sin \phi},$$

(1.9)

so that the force–rotation relation reported dashed in Fig. 1.4 for $\phi_0 = 1°$ and $\phi_0 = 10°$ is obtained.

1.2 Vibrations, buckling and the elastica for a structure subject to tensile (and compressive) dead loading

In order to generalize the single-degree-of-freedom system model into an elastic structure, we consider two *inextensible* elastic rods clamped at one end and joined through a slider, identical to that used to join the two rigid bars employed for the single-degree-of-freedom system (see the inset of Fig. 1.5). The two bars have bending stiffness B, length l^- (on the left) and l^+ (on the right) and are subject to a load F which may be tensile ($F > 0$) or compressive ($F < 0$).

1.2.1 The vibrations and critical loads

The differential equation governing the dynamics of an elastic rod subject to an axial force F (assumed positive if tensile) is

$$\frac{\partial^4 v(z, t)}{\partial z^4} - \frac{F}{B} \frac{\partial^2 v(z, t)}{\partial z^2} + \frac{\rho}{B} \frac{\partial^2 v(z, t)}{\partial t^2} = 0,$$

(1.10)

where ρ is the unit-length mass density of the rod and v the transversal displacement, so that time-harmonic motion is based on the separate-variable representation

$$v(z, t) = \tilde{v}(z) \, e^{-i\omega t},$$

(1.11)

in which ω is the circular frequency, t is the time and $i = \sqrt{-1}$ is the imaginary unit.

A substitution of Eq. (1.11) into Eq. (1.10) yields the equation govern-

ing time-harmonic oscillations

$$\frac{d^4\tilde{v}(z)}{dz^4} - \alpha^2\,\mathrm{sign}(F)\,\frac{d^2\tilde{v}(z)}{dz^2} - \beta\tilde{v}(z) = 0, \qquad (1.12)$$

where the function 'sign' (defined as $\mathrm{sign}(\alpha) = |\alpha|/\alpha\ \forall\alpha \in \mathrm{Re}$ and $\mathrm{sign}(0) = 0$) has been used and

$$\alpha^2 = \frac{|F|}{B}, \quad \beta = \omega^2\frac{\rho}{B}. \qquad (1.13)$$

The general solution of Eq. (1.12) is

$$\tilde{v}(z) = C_1\cosh(\lambda_1 z) + C_2\sinh(\lambda_1 z) + C_3\cos(\lambda_2 z) + C_4\sin(\lambda_2 z), \quad (1.14)$$

where

$$\lambda_{1,2} = \sqrt{\frac{\sqrt{\alpha^4 + 4\beta} \pm \alpha^2\,\mathrm{sign}(F)}{2}}. \qquad (1.15)$$

Eq. (1.14) holds both for the rod on the left (transversal displacement denoted with '−') and on the right (transversal displacement denoted with '+') shown in the inset of Fig. 1.5, so that the boundary conditions at the clamps impose

$$\tilde{v}^-(0) = \left.\frac{d\tilde{v}^-}{dz}\right|_{z=0} = 0, \quad \tilde{v}^+(l^+) = \left.\frac{d\tilde{v}^+}{dz}\right|_{z=l^+} = 0, \qquad (1.16)$$

while at the slider we have the two conditions

$$\left.\frac{d^3\tilde{v}^-}{dz^3}\right|_{z=l^-} = \left.\frac{d^3\tilde{v}^+}{dz^3}\right|_{z=0} = 0, \qquad (1.17)$$

expressing the vanishing of the shear force. The imposition of the six conditions (1.16)–(1.17) provides the constants $C^{\pm}_{2,3,4}$ as functions of the constants $C^{\pm}_1$, so that the continuity of the rotation at the slider

$$\left.\frac{d\tilde{v}^-}{dz}\right|_{z=l^-} = \left.\frac{d\tilde{v}^+}{dz}\right|_{z=0} \qquad (1.18)$$

and the equilibrium of the slider

$$\frac{d^2\tilde{v}^-}{dz^2}\bigg|_{z=l^-} - \alpha^2 \operatorname{sign}(F)\ \tilde{v}^-(l^-) = \frac{d^2\tilde{v}^+}{dz^2}\bigg|_{z=0} - \alpha^2 \operatorname{sign}(F)\ \tilde{v}^+(0), \quad (1.19)$$

yields finally a linear homogeneous system (with unknowns C_1^- and C_1^+), whose determinant has to be set equal to zero, to obtain the frequency equation, function of α^2, ω and $\operatorname{sign}(F)$. The circular frequency ω (normalized through multiplication by $\sqrt{\rho l^4/B}$) versus the axial force (normalized through multiplication by $4l^2/(B\pi^2)$) is reported in Fig. 1.5, where the first four branches are shown for a system of two rods of equal length. In this figure the gray zones represent situations that cannot be achieved,
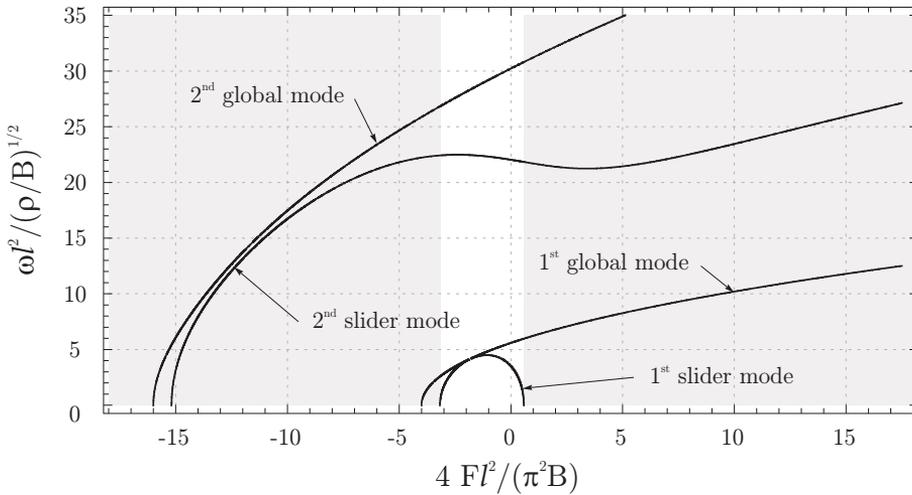
Fig. 1.5: Dimensionless circular frequency ω for the structure shown in the inset (in the particular case of rods of equal length, l) as a function of the dimensionless applied load F. Note that solutions in the gray region cannot be achieved, since the rods cannot remain straight for axial forces external to the bifurcation range of loads (shown as a white zone).

in the sense that the axial force falls outside the interval where the straight configuration of the system is feasible (in other words, for axial loads external to the interval of first bifurcations in tension and compression the straight configuration cannot be maintained).

The branches shown in Fig. 1.5 intersect the horizontal axis in correspondence to the bifurcation loads of the system, namely, $4F_{cr}l^2/(\pi^2 B) = -16, -15.19, -4, -3.17, +0.58$, so that there is one critical load in tension (the corresponding branch is labeled '1st slider mode' in Fig. 1.5), and infinitely many bifurcation loads in compression, the first three are reported in Fig. 1.5 (bifurcations corresponding to the label 'global mode' do not involve relative displacement across the slider).

Beside the possibility of bifurcation in tension, an interesting and novel effect related to the presence of the slider is that a tensile (compressive) axial force yields a decrease (increase) of the frequency of the system, while an opposite effect is achieved when 'global modes' are activated.

Quasi-static solutions of the system and related bifurcations can be obtained in the limit $\omega \to 0$ of the *frequency equation*, which yields

$$
\begin{cases}
\tanh\left(\alpha\, l^-\right)\cosh\left(\alpha\, l^+\right) + \\
+ \sinh\left(\alpha\, l^+\right)\left[1 - (l^+ + l^-)\,\alpha\tanh\left(\alpha\, l^-\right)\right] = 0, \qquad \text{for } F > 0, \\
\tan\left(\alpha\, l^-\right)\cos\left(\alpha\, l^+\right) + \\
+ \sin\left(\alpha\, l^+\right)\left[1 + (l^+ + l^-)\,\alpha\tan\left(\alpha\, l^-\right)\right] = 0, \qquad \text{for } F < 0.
\end{cases}
\tag{1.20}
$$

In the particular case of rods of equal length l, Eqs. (1.20) simplify to

$$
\begin{cases}
\sinh\left(\alpha\, l\right)\left[1 - \alpha\, l\,\tanh\left(\alpha\, l\right)\right] = 0, \qquad \text{for } F > 0, \\
\sin\left(\alpha\, l\right)\left[1 + \alpha\, l\,\tan\left(\alpha\, l\right)\right] = 0, \qquad \text{for } F < 0.
\end{cases}
\tag{1.21}
$$

Eqs. (1.21) show clearly that *there is only one bifurcation load in tension* (branch labeled '1st slider mode' in Fig. 1.5), but there are ∞^2 bifurcation loads in compression (the first three branches are reported in Fig. 1.5). In compression, the bifurcation condition $\sin\left(\alpha\, l\right) = 0$, providing ∞^1 solutions, yields the critical loads of a doubly clamped beam of length $2l$ and defines what we have labeled 'global modes' in Fig. 1.5. Bifurcation loads, normalized through multiplication by $(l^+ + l^-)^2/(\pi^2 B)$, are reported in Fig. 1.6 as functions of the ratio l^+/l^- between the lengths of the two rods.

Note that the graph is plotted in a semi-logarithmic scale, which en-

forces symmetry about the vertical axis. In the graph, the first two buckling loads in compression are reported: the first corresponds to a mode involving sliding, while the second does not involve any sliding (and when $l^+ = l^-$ corresponds to the first mode of a doubly clamped rod of length $2l$). Used as an optimization parameter, $l^+ = l^-$ corresponds to the lower bifurcation load in tension ($+0.58$), near five times smaller (in absolute value) that the buckling load in compression (-3.17).
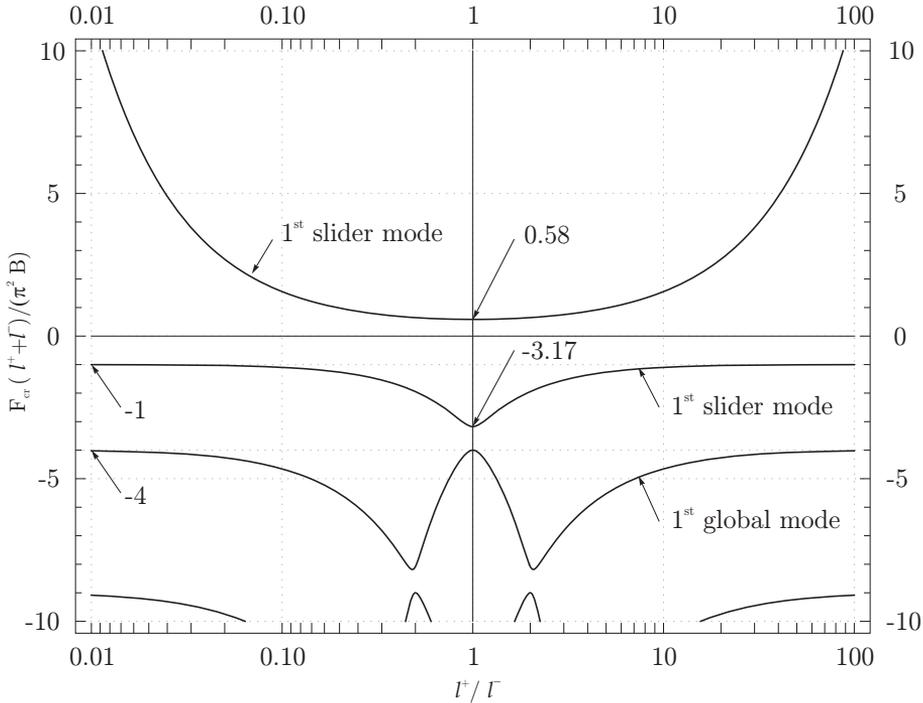
Fig. 1.6: Dimensionless critical loads F_{cr} as a function of the ratio between the lengths of the rods, l^+/l^-. The dimensionless axial forces for bifurcation in tension and those corresponding to the first two modes in compression are reported.

1.2.2 The elastica

The determination of the non-trivial configurations at large deflections of the mechanical system requires a careful use of Euler's elastica. It is

instrumental to employ the reference systems shown in Fig. 1.7 and impose one kinematic compatibility condition and three equilibrium conditions. These are as follows.

- The kinematic compatibility condition can be directly obtained from Fig. 1.7 noting that the jump in displacement across the slider (measured orthogonally to the line of the elastica), Δ_s, can be related to the angle of rotation of the slider Φ_s, a condition that assuming the local reference systems shown in Fig. 1.7 becomes

$$\left[x_1^-(l^-) + x_1^+(l^+) \right] \tan \Phi_s + x_2^-(l^-) + x_2^+(l^+) + \Delta_s = 0, \quad (1.22)$$

where $x_1(s)$ and $x_2(s)$ are the coordinates of the elastica and the index $-$ ($+$) denotes that the quantities are referred to the rod on the left (on the right). Note that Φ_s is assumed positive when anticlockwise and Δ_s is not restricted in sign (negative in the case of Fig. 1.7).

- Since the slider can only transmit a moment and a force R orthogonal to it, equilibrium requires that (see the inset in Fig. 1.7)

$$R = \frac{F}{\cos \Phi_s}, \quad (1.23)$$

where F is the axial force providing the load to the rod, assumed positive (negative) when tensile (compressive), so that since $\Phi_s \in [-\pi/2, \pi/2]$, R is positive (negative) for tensile (compressive) load. Note that with the above definitions we have

$$\theta^+(0) = \theta^-(0) = 0, \quad \theta^+(l^+) = \theta^-(l^-) = -\Phi_s. \quad (1.24)$$

- Equilibrium of the slider requires that

$$\kappa_s^- + \kappa_s^+ = \frac{R}{B} \Delta_s, \quad (1.25)$$

where B is the bending stiffness of the rod and $\kappa_s^\pm$ is the curvature on the left ($-$) or on the right ($+$) of the slider. Note that B is always positive, but R, $\kappa_s^\pm$ and Δ_s can take any sign.
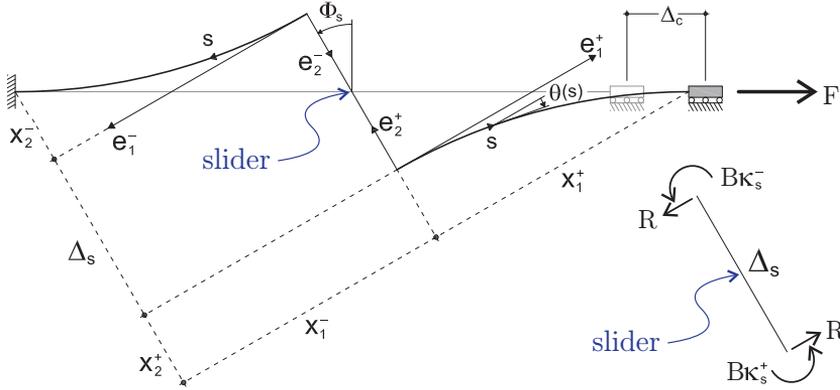
Fig. 1.7: Sketch of the problem of the elastica under tensile axial load F. Note the reference systems employed in the analysis and note that the moments on the slider have been reported positive and the curvature results to be negative.

- For both rods (left and right) rotational equilibrium of the element of rod singled out at curvilinear coordinate s requires

$$\frac{d^2\theta}{ds^2} - \frac{R}{B}\sin\theta = 0, \tag{1.26}$$

where θ is the rotation of the normal at each point of the elastica, assumed positive when anticlockwise, with added the superscript $-$ $(+)$ to denote the rod on the left (on the right).

Eq. (1.26) is usually (see for instance Love, 1927, his Eq. (8) at Sect. 262) written with a sign '+' replacing the sign '−' and R is assumed positive when compressive; the same equation describes the motion of a simple pendulum (see for instance Temme, 1996). The '+' sign originates from the fact that the elastica has been analyzed until now only for deformations originating from compressive loads. However, an equation with the '−' sign and with R/B replaced by the ratio between unit weight density and surface tension of a fluid –thus equal to Eq. (1.26)– determines *the shape of the capillary curve of a liquid* (Lamb, 1928), which therefore results to be identical to the deflection of a rod under tensile load.

In the following we derive equations holding along both rods '+' and '−', so that these indices will be dropped for simplicity. Multiplication of Eq. (1.26) by $d\theta/ds$ and integration from 0 to s yields

$$\left(\frac{d\theta}{ds}\right)^2 = -2\,\tilde{\alpha}^2\,\text{sign}(R)\,\cos\theta + 2\,\tilde{\alpha}^2\left(\frac{2}{k^2} - 1\right), \qquad (1.27)$$

where, using the Heaviside step function H, we have

$$\tilde{\alpha}^2 = \frac{|R|}{B} \quad \text{and} \quad k^2 = \left(\frac{\kappa_s^2}{4\,\tilde{\alpha}^2} + H(R)\right)^{-1}. \qquad (1.28)$$

Eq. (1.27) can be re-written as

$$\left(\frac{d\theta}{ds}\right)^2 = \frac{4\,\tilde{\alpha}^2}{k^2}\left[1 - k^2\sin^2\left(\frac{\theta}{2} + \frac{\pi}{2}H(R)\right)\right], \qquad (1.29)$$

so that the change of variable $u = s\tilde{\alpha}/k$ yields

$$\frac{d\theta}{du} = \pm 2\sqrt{1 - k^2\sin^2\left(\frac{\theta}{2} + \frac{\pi}{2}H(R)\right)}. \qquad (1.30)$$

The analysis will be restricted for simplicity to the case '+' in the following. At $u = 0$ it is $\theta = 0$, so that Eq. (1.30) gives the solution

$$\theta = 2\,\text{am}\,[u + KH(R), k] - \pi\,H(R) \qquad (1.31)$$

and

$$\frac{d\theta}{ds} = \frac{2}{k}\,\tilde{\alpha}\,\text{dn}\,[u + KH(R), k], \qquad (1.32)$$

where am and dn are respectively the Jacobi elliptic functions amplitude and delta-amplitude and K is the complete elliptic integral of the first kind (Byrd and Friedman, 1971). Since in the local reference system we have $dx_1/ds = \cos\theta$ and $dx_2/ds = \sin\theta$, an integration gives the coordinates

x_1 and x_2 of the elastica expressed in terms of u,

$$
\begin{cases}
x_1 = \dfrac{\left(2 - k^2\right) u - 2\,\mathrm{E}\left[\mathrm{am}\left[u, k\right], k\right] + 2k^2 \mathrm{sn}\left[u, k\right] \mathrm{cd}\left[u, k\right]}{k\,\tilde{\alpha}} \\[3mm]
x_2 = \dfrac{2\sqrt{1 - k^2}\left(1 - \mathrm{dn}\left[u, k\right]\right)}{k\,\tilde{\alpha}\,\mathrm{dn}\left[u, k\right]}
\end{cases}
\tag{1.33}
$$

for tensile axial loads $(R > 0)$, while for compressive axial loads $(R < 0)$

$$
\begin{cases}
x_1 = \dfrac{\left(k^2 - 2\right) u + 2\,\mathrm{E}\left[\mathrm{am}\left[u, k\right], k\right]}{k\,\tilde{\alpha}} \\[3mm]
x_2 = \dfrac{2\left(1 - \mathrm{dn}\left[u, k\right]\right)}{k\,\tilde{\alpha}}
\end{cases}
\tag{1.34}
$$

in which the constants of integration are chosen so that x_1 and x_2 vanish at $s = 0$. In Eqs. (1.33)–(1.34) sn and cn are respectively the Jacobi elliptic functions sine-amplitude and cosine-amplitude/delta-amplitude and E is the incomplete elliptic integral of the second kind (Byrd and Friedman, 1971).

Eqs. (1.34) differ from Eqs. (16) reported by Love (1927, his Section 263) only in a translation of the coordinate x_2, while Eqs. (1.33), holding for tensile axial force, are new.

Finally, with reference to Fig. 1.7, we note that the horizontal displacement Δ_c of the right clamp can be written in the form

$$
\Delta_c = \frac{x_1^-\left(l^-\right) + x_1^+\left(l^+\right)}{\cos \Phi_s} - \left(l^+ + l^-\right).
\tag{1.35}
$$

To find the axial load F as a function of the slider rotation Φ_s, or as a function of the end displacement Δ_c, we have now to proceed as follows:

- values for κ_s^- and κ_s^+ are fixed (as a function of the selected mode, for instance, $\kappa_s^- = \kappa_s^+$, to analyze the bifurcation mode in tension);

- k can be expressed using Eq. (1.28)$_2$ as a function of $\tilde{\alpha}$;

- the equations for the coordinates of the elastica, Eq. (1.33) for tensile load, or Eq. (1.34) for compressive load, and Eq. (1.31), evaluated

21
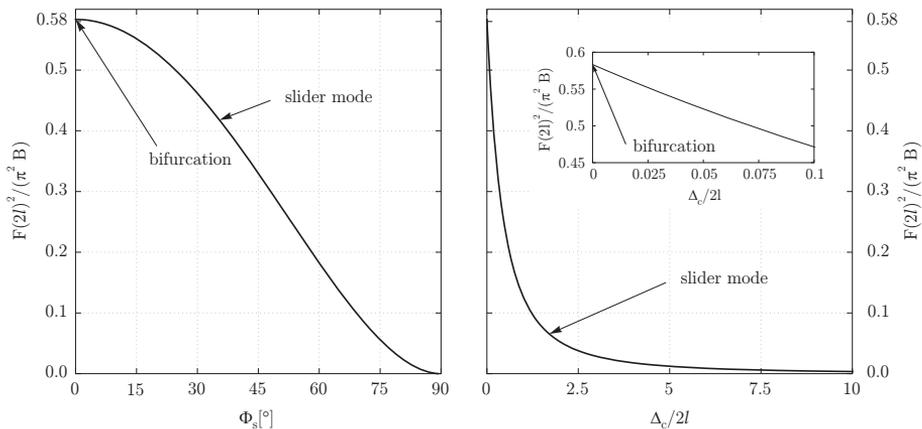
Fig. 1.8: Bifurcation of the structure sketched in Fig. 1.7 under tensile load. Dimensionless axial load F versus slider rotation (versus dimensionless end displacement) is shown on the left (on the right).

at l^- and l^+, become functions of only $\tilde{\alpha}$;

- Eqs. (1.24) and (1.25) provide Φ_s and Δ_s, so that Eq. (1.22) becomes a nonlinear equation in the variable $\tilde{\alpha}$, which can be numerically solved (we have used the function FindRoot of Mathematica® 6.0);

- when $\tilde{\alpha}$ is known, R and F can be obtained from Eqs. $(1.28)_1$ and (1.23);

- finally, Φ_s and Δ_c are calculated using Eqs. $(1.24)_2$ and (1.35).

Results are shown in Fig. 1.8 for tensile loads and in Fig. 1.9 for compressive loads, in terms of dimensionless axial load $4Fl^2/(B\pi^2)$ versus slider rotation Φ_s (on the left) and dimensionless end displacement $\Delta_c/(2l)$ (on the right).

Note that, while there is only one bifurcation in tension, there are infinite bifurcations in compression, so that we have limited results to the initial three modes in compression. Two of these modes involve slider rotation (labeled 'slider mode'), while an intermediate mode (labeled 'global mode') does not.

22
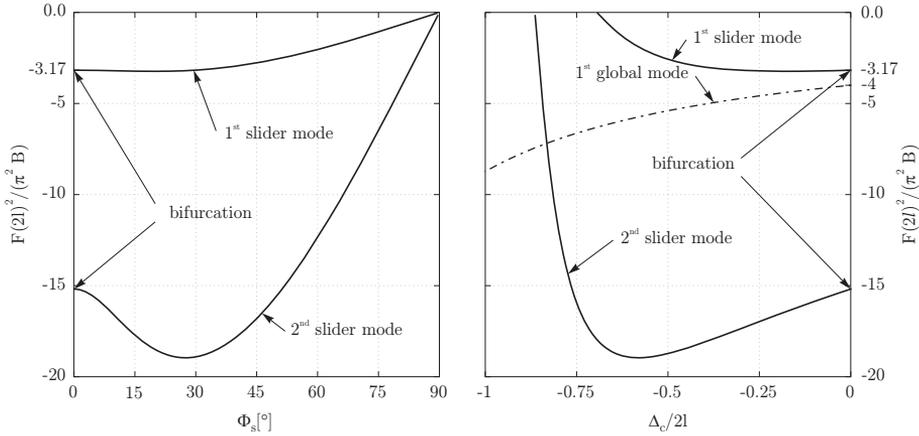
Fig. 1.9: Bifurcation of the structure sketched in Fig. 1.7 under compressive load. Dimensionless axial load F versus slider rotation (versus dimensionless end displacement) is shown on the left (on the right).

The load/displacement curve shown in Fig. 1.8 on the left is plotted until extremely large displacements, namely, $\Delta_c = 20l$ (a detail at moderate displacement is reported in the inset). It displays a *descending, in other words softening and unstable, postcritical behaviour*, which contrasts with the usual postcritical of the elastica under various end conditions, in which the load rises with displacement. In compression, the post-critical behaviour evidences another novel behaviour, so that the first and the second slider modes present an initial part where the load/displacement rises, followed by a softening behaviour. Finally, it is important to note that the curves load versus Φ_s in Figs. 1.8 and 1.9, both *for tension and compression intersect each other at null loading* at the extreme rotation $\Phi_s = 90°$, which means that two unloaded configurations (in addition to the initial configuration) exist. These peculiarities, never observed before in simple elastic structures, are all related to the presence of the slider.

Deformed elastic lines are reported in Fig. 1.10, both for tension and compression, the latter corresponding to the first three slider modes (the global mode is not reported since it corresponds to the first mode of a doubly-clamped rod).
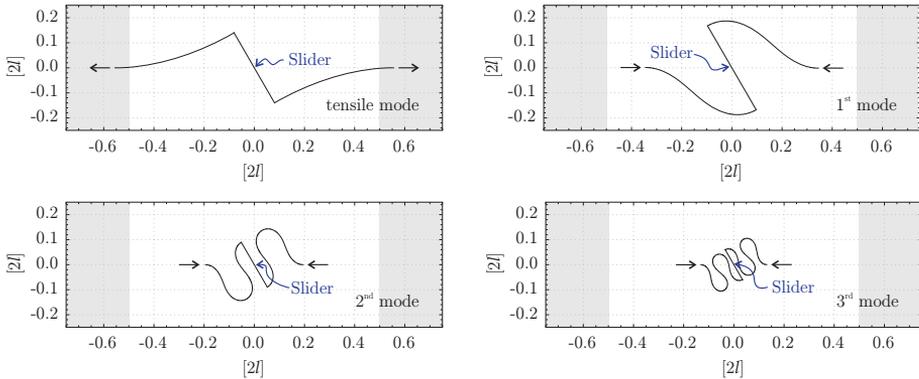
Fig. 1.10: Deflections (the scale of the axes is $2l$) of the structure shown in Fig. 1.7 (with rods of equal length) at a slider rotation of $30°$ in tension (upper part, on the left) and compression (first 3 slider modes are reported, whereas the global mode has not been reported).

1.3 Experiments on the Elastica

The structure sketched in Fig. 1.7 has been realized with two carbon steel AISI 1095 strips ($250\,\mathrm{mm} \times 25\,\mathrm{mm} \times 1\,\mathrm{mm}$; Young modulus $200\,\mathrm{GPa}$) and the slider with two linear bearings (type Easy Rail SN22-80-500-610, purchased from Rollon®), commonly used in machine design applications, see Fig. 1.11. The slider is certified by the producer to have a low friction coefficient, equal to 0.01. Tensile force on the structure has been provided by imposing displacement with a load frame ELE Tritest 50 (ELE International Ltd), the load measured with a load cell Gefran OC-K2D-C3 (Gefran Spa), and the displacement with a potentiometric transducer Gefran PY-2-F-100 (Gefran Spa). Data have been acquired with system NI CompactDAQ, interfaced with Labview 8.5.1 (National Instruments). Photos have been taken with a Nikon D200 digital camera, equipped with a AF-S micro Nikkor lens ($105\,\mathrm{mm}$ 1:2.8G ED) and movies with a Sony Handycam HDR-XR550. Tensile and compressive tests have been run at a velocity of $2.5\,\mathrm{mm/s}$.

Photos taken at different slider rotations (and thus load levels) are shown in Fig. 1.12 for tension ($\Phi_s = 0°$, $10°$, $20°$, $30°$) and in Fig. 1.13 for compression ($\Phi_s = 0°$, $5°$, $10°$, $20°$). A comparison between theo-

24
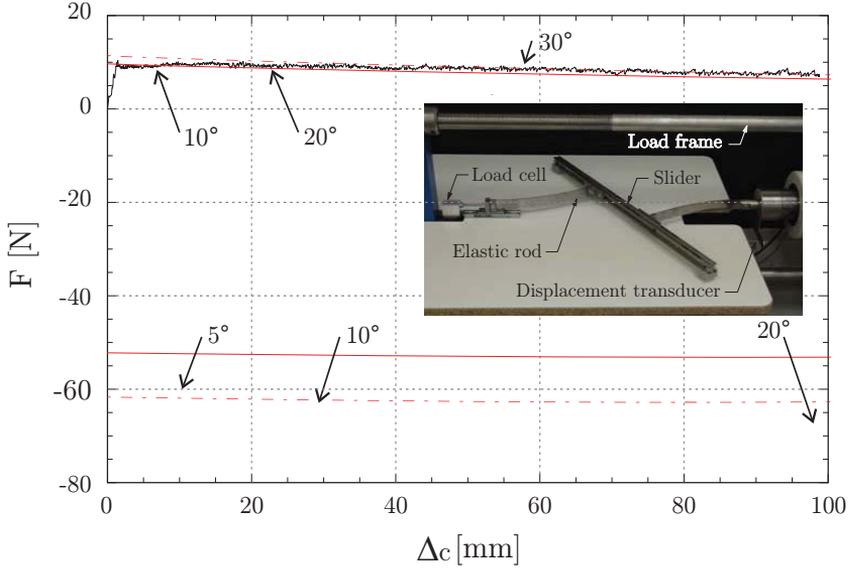
Fig. 1.11: Load versus end displacement for the model representing the structure sketched in Fig. 1.7 recorded during tensile (positive F) and compressive (negative F) tests. The red curves are the theoretical predictions (the dashed line is obtained keeping into account the effective values of the lengths of the rods, 10% smaller than the values measured from the clamps to the middle of the slider). The values '5°', '10°', '20°' and '30°' denote the inclination of the slider in degrees reached during the test. A photo of the experimental setup during the postcritical behaviour in tension is reported on the right.

retical predictions and experiments is reported in the lower parts of the figures where photos are superimposed to the line of the elastica, shown in red and plotted using Eq. (1.33) for tensile load and Eq. (1.34) for compression. These experiments show clearly the existence of the bifurcation in tension and provide an excellent comparison with theoretical results obtained through integration of the elastica both in tension and in compression. A further quantitative comparison between theoretical results and experiments is provided in Fig. 1.11, where the axial load in the structure (positive for tension and negative for compression) is plotted versus the end displacement Δ_c. The experimental result is compared to theoretical results (marked red) expressed by Eq. (1.35), used in the way
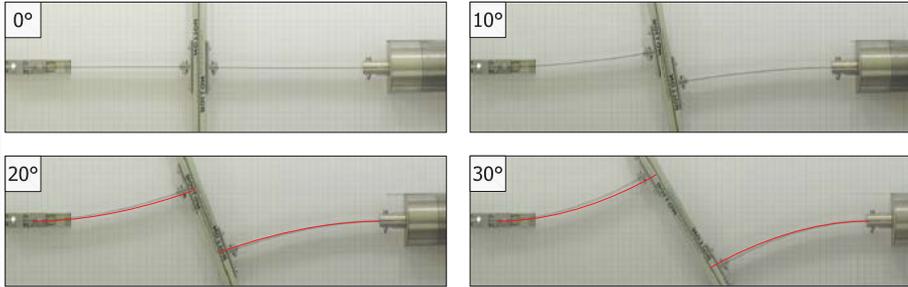
Fig. 1.12: Photos of the model representing the structure sketched in Fig. 1.7 and loaded in tension at different values of slider rotation $\Phi_s = 0°$, $10°$, (upper part) $20°$, $30°$ (center). The elastica calculated with Eq. (1.33) is superimposed on the photos at $20°$, $30°$ in the lower part. The side of the grid marked on the paper is $10\,\text{mm}$.
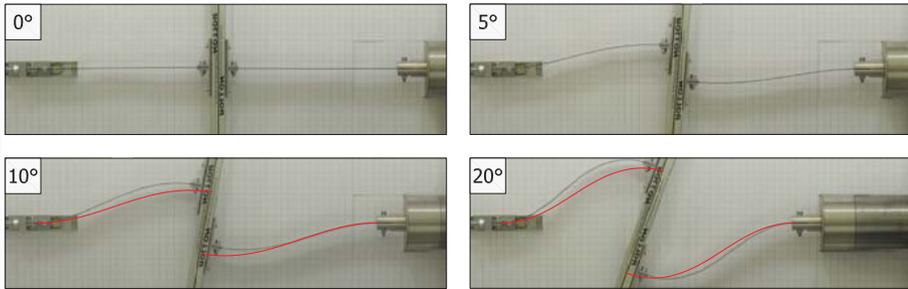
Fig. 1.13: Photos of the model representing the structure sketched in Fig. 1.7 and loaded in compression at different values of slider rotation $\Phi_s = 0°$, $5°$, (upper part) $10°$, $20°$ (center). The elastica calculated with Eq. (1.33) is superimposed on the photos at $10°$, $20°$ in the lower part. The side of the grid marked on the paper is $10\,\text{mm}$.

detailed at the end of Section 1.2.2.

The theoretical result marked in red with continuous curve has been calculated assuming an initial length of the rods (25 cm) measured from the end of the clamps to the middle of the slider. However, the slider and the junctions to the metal strips are $58\,\text{mm}$ thick, so that the system is stiffer in reality. Therefore, we have plotted dashed the theoretical results obtained employing an 'effective' initial length of the rods reduced of 10% (so that the effective length of the system has been taken equal to 45 cm).

The experimental curve evidences oscillations of ± 1 N for tensile loads and ± 5 N for compressive loads. These oscillations are due to friction within the slider, so that it is obvious that the oscillations are higher in compression than in tension, since in the former case the load is higher. Except for these oscillations, the friction (which is very low) has been found not to influence the tests.

The fact that experimentally the bifurcations initiate before the theoretical values are attained represents the well-known effect of imperfections, so that we may conclude that the agreement between theory and experiments is excellent.

To provide experimental evidence to the fact that the elastica in tension corresponds to the shape of the free surface of a liquid in a capillary channel, we note that a meniscus in a capillary channel satisfies (by symmetry) a null-rotation condition at the centre of the channel, so that it corresponds to a clamped edge of a rod. If the tangent to the meniscus at the contact with the channel wall is taken to correspond to the rotation of the non-clamped edge of the rod and the width of the channel is calculated employing the elastica, the elastic deflection of the rod scales with the free surface of the liquid. Therefore, we have performed an experiment in which we have taken a photo (with a Nikon SMZ800 stereo-zoom microscope equipped with Nikon Plan Apo 0.5x objective and a Nikon DD-FI1 high definition color camera head) of a water meniscus in a polycarbonate channel. We have proceeded as follows. First, we have observed that the contact angle between a water surface in air and polycarbonate (at a temperature of 20°C) is 70°. Second, we have taken a photo of the meniscus formed in a polycarbonate 'V-shaped' channel with walls inclined at 10° with the vertical, so that the angle between the horizontal direction and the free surface results to be 30° and the distance between the walls results 6 mm. This photo has been compared with a photo taken (with a Nikon D200 digital camera, and shown in Fig. 1.12 on the right) during buckling in tension when the elastic rods form the same angle of 30°. The result is shown in Fig. 1.1, together with the theoretical solution shown red.

2

Effects of the constraint's curvature on structural instability: tensile buckling and multiple bifurcations

Bifurcation of an elastic structure crucially depends on the curvature of the constraints against which the ends of the structure are prescribed to move, an effect which deserves more attention than it has received so far. In fact, it is shown theoretically and experimentally verified that an appropriate curvature of the constraint over which the end of a structure has to slide strongly affects buckling loads and can induce: (i.) tensile buckling; (ii.) decreasing- (softening), increasing- (hardening), or constant-load (null stiffness) postcritical behaviour; (iii.) multiple bifurcations, determining for instance two bifurcation loads (one tensile and one compressive) in a single-degree-of-freedom elastic system. It is shown how to design a constraint profile to obtain a desired postcritical behaviour and we provide the solution for the elastica constrained to slide along a circle on one end, representing the first example of an inflexional elastica developed from a buckling in tension is provided. These results have important practical implications in the design of compliant mechanisms and may find applications in devices operating in quasi-static or dynamic conditions, even at the nanoscale.

We begin with a simple example, by considering a one-degree-of-freedom elastic structure made up of a rigid rod connected with a rotational linear elastic spring on its left end and with a roller constrained to move on a circle (of radius R_c, centred on the rod's axis) on the right (Fig. 2.1). The structure is subject to a horizontal force, so that when this load is compressive and the circle degenerates to a line (null curvature), the
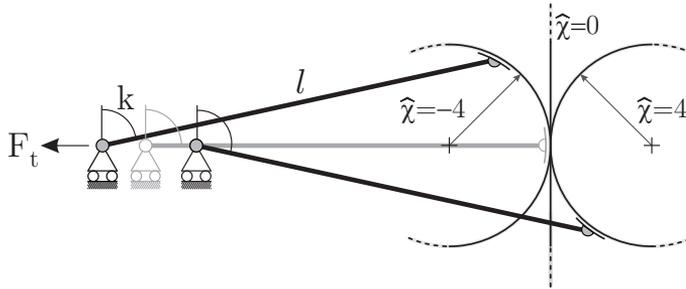
Fig. 2.1: A one-degree-of-freedom structure (with a rotational elastic spring at its left end) evidencing compressive or tensile buckling as a function of the curvature of the constraint (a circular profile with constant curvature, $\widehat{\chi} = \pm 4$) on which the hinge on the right of the structure has to slide.

structure buckles at the compressive force $F = -k/l$. Our interest is to analyze the case when the curvature of the constraint is not null, revealing that this curvature strongly affects the critical load, which results to be a *tensile* force[1] in the negative curvature case ($F_t = k/(3l)$, for $\widehat{\chi} = l/R_c = -4$) and a compressive load for positive curvature ($F_c = -k/(5l)$, for $\widehat{\chi} = l/R_c = 4$).

The example shows that the curvature of the constraint at the end of a structure deeply affects its critical load[2], but also the shape of the curve defining the constraint influences the postcritical behaviour, which displays a rising-load (hardening) behaviour in the case of null curvature and a decreasing-load (softening) behaviour for circular profiles (for instance, when $\widehat{\chi} = \pm 4$, as in the structure shown in Fig. 2.1). Moreover, the postcritical behaviour connected to the tensile (compressive) bifurcation evidences force reversal, since the tensile (compressive) force needed to buckle the structure decreases until it vanishes and becomes compressive

---

[1]Tensile buckling of an elastic structure governed by the elastica, in which all elements are strictly subject to tension, is reported in Chapter 1.

[2]The fact that the curvature influences the critical load was observed in different terms already by Timoshenko and Gere (1936), who analyzed the case of the so-called 'load through a fixed point'. However, they did not generalize the problem enough to discover that: tensile buckling, multiple bifurcations and inflexional tensile elastica during the postcritical behaviour can be obtained, which is the topic attacked in the present chapter.

(tensile), during continued displacement of the structure end.

Once the lesson on the curvature and the shape of the constraint is
clear, it becomes easy to play with these structural elements and discover
several new effects. Some of these are listed in the following.

- A constraint profile can be designed to provide a 'hardening', 'soften-
  ing' or even a '*neutral*' (in which the displacement grows at constant
  load) postcritical behaviour. More in general, a formula will be given
  to determine the shape of the profile to obtain a desired postcriti-
  cal behaviour, including situations in which the stability of the path
  changes during postcritical deformation.

- A negative and a positive curvature can be combined in an 'S-shaped
  constraint' (see the inset of Fig. 2.2) to yield *a one-degree-of-freedom
  structure with two buckling loads: one tensile and one compressive.*
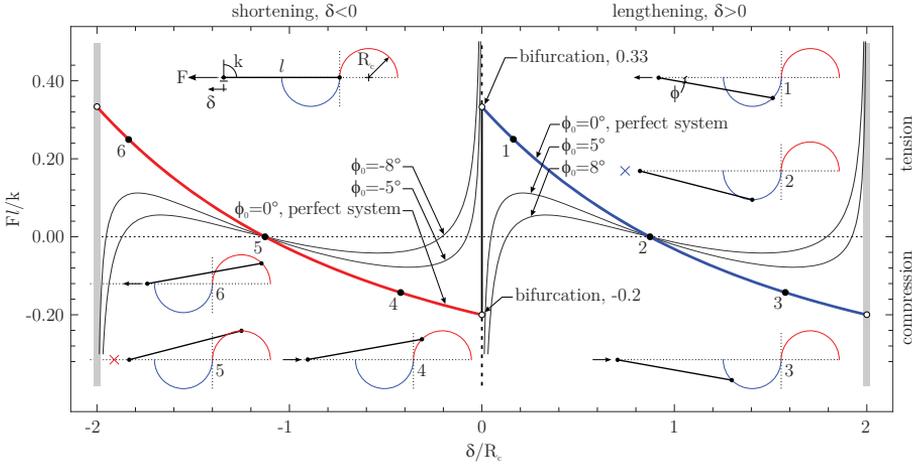
Fig. 2.2: The behaviour of a one-degree-of-freedom structure evidencing two buckling
loads, one compressive and one tensile. These are the effect of the discontinuity in
the curvature of the (piecewise circular) constraint. Note that: (i.) the two unstable
postcritical branches are identical modulo a horizontal shift and that (ii.) during the
postcritical behaviour there is a force reversal, with a transition from tensile (compres-
sive) to compressive (tensile) load.

In the case of the 'S-shaped constraint', imperfections suppress bifurcations and the stability of the equilibrium path strongly depends on the *sign* of the imperfection. For tensile forces, if the imperfection has a positive sign ($\phi_0 > 0$), the equilibrium path of the system becomes unstable after a peak in the load is reached, while if the sign is negative ($\phi_0 < 0$), the structure remains in a metastable equilibrium configuration which asymptotically approaches an unstable configuration (Fig. 2.2).

Finally, we can appreciate the role played by the curvature of a constraint in the more interesting case of a structural element governed by the elastica, a research aspect passed unnoticed until now, but interesting for the applications in compliant mechanisms. We show that consideration of this curvature provides a generalization of the findings reported in Chapter 1, so that their 'slider' can be seen as a special case of the curved constraint introduced here and the elastica developing after a tensile buckling is of inflexional type, while that investigated in Chapter 1 is non-inflexional. We fully develop the theory of the elastica constrained to slide with a rotational spring along a circle on one of its ends and we experimentally confirm the theoretical findings with experiments designed and realized by us.

This chapter is organized as follows. We begin presenting a generalization of the one-degree-of-freedom structure shown in Fig. 2.1, to highlight: (i.) the effects of the curvature of the constraint, (ii.) the multiplicity of bifurcation loads, (iii.) the behaviour of the imperfect system, and (iv.) the possibility of designing a constraint profile to obtain a given postcritical behaviour. Later we analyze a continuous system, made up of an inextensible beam governed by the Euler elastica and we solve the critical loads and the nonlinear postcritical large-deformation behaviour, through explicit integration of the elastica. We systematically complement theoretical results with experiments confirming all our findings for discrete and continuous elastic systems. A movie providing a simple illustration of the concepts exposed here, together with a view of experimental results, is available in the electronic supplementary material, see also http://ssmg.unitn.it/.

2.1 Effect of the constraint's curvature on a one-degree-of-freedom elastic structure

Bifurcation load and equilibrium paths of the one-degree-of-freedom structure illustrated in Fig. 2.3 (where the constraint is assumed smooth and described in the x_1–x_2 reference system as $x_2 = l\,f(\psi)$, with $\psi = x_1/l \in [0,1]$ and $f'(0) = 0$) can be calculated by considering a deformed mode defined by the rotation angle ϕ. Assuming a possible imperfection in terms of an initial inclination ϕ_0, the elongation of the system and the potential energy are respectively

$$\delta = l\left[\cos\phi - \cos\phi_0 - f(\sin\phi) + f(\sin\phi_0)\right] \tag{2.1}$$

and

$$W(\phi) = \frac{1}{2}k(\phi - \phi_0)^2 - Fl\left[\cos\phi - \cos\phi_0 - f(\sin\phi) + f(\sin\phi_0)\right], \tag{2.2}$$

so that solutions of the equilibrium problem are governed by

$$F = -\frac{k\,(\phi - \phi_0)}{l[\sin\phi + \cos\phi\, f'(\sin\phi)]}, \tag{2.3}$$

where $f' = \partial f/\partial \psi$, so that the critical load for the perfect system, $\phi_0 = 0$,
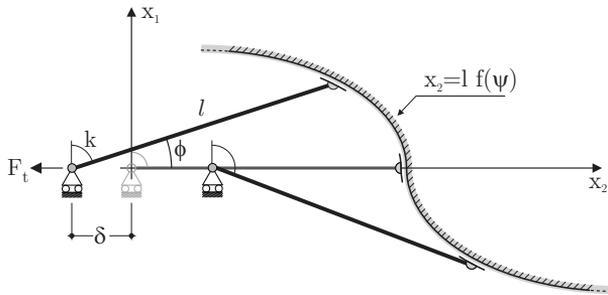
Fig. 2.3: A one-degree-of-freedom structure with an hinge constrained to slide along a generic smooth profile at the right end and a rotational linear-elastic spring at the left end.

is

$$F_{cr} = -\frac{k}{l[1 + f''(0)]}, \tag{2.4}$$

where, since $f'(0) = 0$, $f''(0) = \widehat{\chi}(0)$ is the signed curvature at $\phi = 0$. Stability can be judged on the basis of the sign of the second derivative of the potential energy

$$\frac{\partial^2 W(\phi)}{\partial \phi^2} = k + Fl\left(\cos\phi - f'\sin\phi + f''\cos^2\phi\right), \tag{2.5}$$

showing that the trivial configuration of the perfect system is always unstable beyond the critical load.

In the case when the profile of the constraint is a circle[3] of dimensionless radius $1/|\widehat{\chi}| = 1/l|\chi|$ as in Fig. 2.1, the non-trivial equilibrium configurations are given by

$$F = -\frac{k\,(\phi - \phi_0)\sqrt{1 - \widehat{\chi}^2\sin^2\phi}}{l\,\sin\phi(\widehat{\chi}\cos\phi + \sqrt{1 - \widehat{\chi}^2\sin^2\phi})}, \tag{2.6}$$

and result to be stable when

$$1 - \widehat{\chi}^2\sin^2\phi - (\phi - \phi_0)(\cot\phi - \widehat{\chi}\sin\phi\sqrt{1 - \widehat{\chi}^2\sin^2\phi}) > 0. \tag{2.7}$$

Eqs. (2.6) and (2.7) have been used to solve the special case of Fig. 2.1 ($\widehat{\chi} = \pm4$), with an 'S-shaped' constraint (so that $\widehat{\chi}$ is discontinuous at $\phi = 0$), to obtain the results plotted in Fig. 2.2.

The considered structure (see Fig. 2.3) can be easily generalized by including an additional elastic spring on the hinge sliding along the profile, as shown in Fig. 2.4.

In this structure, the constraint is assumed smooth and described in the x_1–x_2 reference system as $x_2 = l\,f(\psi)$, with $\psi = x_1/l \in [0,1]$ and $f'(0) = 0$.

Bifurcation loads can be calculated by considering a deformed mode defined by the rotation angle ϕ, assumed positive when clockwise. The

---

[3]Note that in the case of a circle the dimensionless signed curvature is $\widehat{\chi} = \pm l/R_c$, with l being the length of the rigid bar and R_c the radius of the circle.
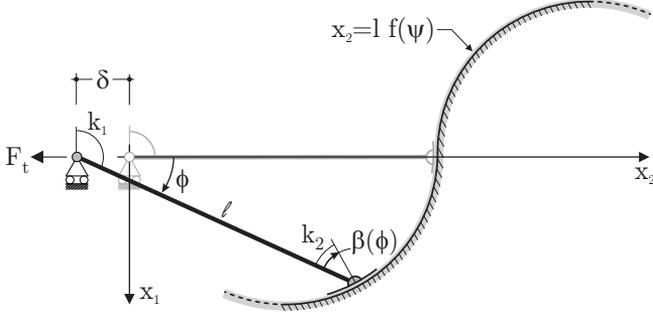
Figure 2.4: A one-degree-of-freedom structure with a linear-elastic hinge constrained to slide along a generic profile at the right end and a rotational linear-elastic spring at the left end.

potential energy of the system is

$$W(\phi) = \frac{1}{2} k_1 \phi^2 + \frac{1}{2} k_2 \beta(\phi)^2 - F \, l \left[\cos \phi - f(\sin \phi)\right], \qquad (2.8)$$

so that the axial force at equilibrium reads

$$F = -\frac{k_1 \phi + k_2 \, \beta(\phi) \, \beta'(\phi)}{l[\sin \phi + \cos \phi \, f'(\sin \phi)]}. \qquad (2.9)$$

When the profile of the constraint is circular, with radius R_c and dimensionless signed curvature $\widehat{\chi} = f''/[1 + (f')^2]^{3/2} = \pm l/R_c$ as shown in the inset of Figs. 2.5 and 2.6, the axial load at equilibrium satisfies

$$\begin{aligned}
F = -\; & \frac{k_1 \phi \sqrt{1 - \widehat{\chi}^2 \sin^2 \phi}}{l \sin \phi (\widehat{\chi} \cos \phi + \sqrt{1 - \widehat{\chi}^2 \sin^2 \phi})} + \\
& - \frac{k_2 \left[\phi + \sin^{-1}(\widehat{\chi} \sin \phi) - \pi \, \mathrm{H}(\widehat{\chi} \phi)\right]}{l \sin \phi},
\end{aligned} \qquad (2.10)$$

where H denotes the Heaviside step function.

Since $\beta(\phi) = -\tan^{-1}[f'(\sin\phi)] - \phi$, the critical load of the system is

$$F_{cr} = -\frac{k_1 + k_2\left[1 + f''(0)\right]^2}{l[1 + f''(0)]} \tag{2.11}$$

where $f''(0) = \widehat{\chi}(0)$ is the signed curvature at $\phi = 0$.

For an imperfect system, characterized by an initial inclination of the rod ϕ_0, the potential energy becomes

$$W(\phi) = \frac{1}{2}k_1(\phi - \phi_0)^2 + \frac{1}{2}k_2\left[\beta(\phi) - \beta(\phi_0)\right]^2 + \\ - Fl\left[\cos\phi - f(\sin\phi) - \cos\phi_0 + f(\sin\phi_0)\right] , \tag{2.12}$$

so that the axial force at equilibrium is

$$F = -\frac{k_1(\phi - \phi_0) + k_2\left[\beta(\phi) - \beta(\phi_0)\right]\beta'(\phi)}{l[\sin\phi + \cos\phi\, f'(\sin\phi)]}, \tag{2.13}$$

which for a circular profile becomes

$$F = -\frac{k_1(\phi - \phi_0)\sqrt{1 - \widehat{\chi}^2\sin^2\phi}}{l\sin\phi(\widehat{\chi}\cos\phi + \sqrt{1 - \widehat{\chi}^2\sin^2\phi})} + \\ - \frac{k_2\left[\phi - \phi_0 + \sin^{-1}(\widehat{\chi}\sin\phi) + \mathrm{sign}(\widehat{\chi}\phi)\sin^{-1}(\widehat{\chi}\sin\phi_0) - \pi\,\mathrm{H}(\widehat{\chi}\phi)\right]}{l\sin\phi} . \tag{2.14}$$

Eq. (2.14) has been used for $\widehat{\chi} = \pm 4$, with an 'S-shaped' constraint (so that $\widehat{\chi}$ is discontinuous at $\phi = 0$), to obtain the results plotted in Figs. 2.5 and 2.6.

2.1.1 The design of the postcritical behaviour

It is important to emphasize that *the shape of the profile on which one end of the structure has to slide can be designed to obtain 'desired postcritical behaviours'*. Let us assume that we want to obtain a certain force-displacement F/δ postcritical behaviour for the structure sketched in Fig. 2.3. Since

$$\delta = l\left[\sqrt{1 - \psi^2} - f(\psi)\right], \tag{2.15}$$
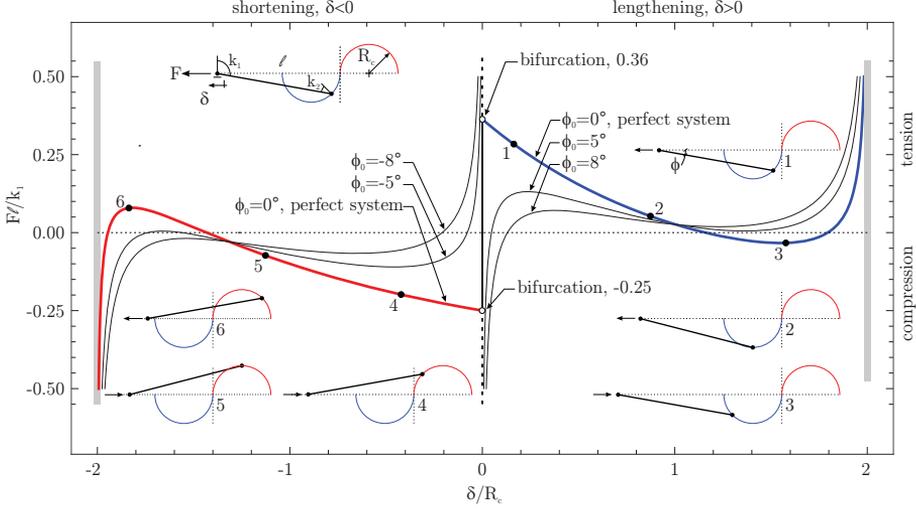
Figure 2.5: The force versus end-displacement behaviour of a single-degree-of-freedom structure, with an 'S-shaped' constraint, $\widehat{\chi} = \pm 4$, and $k_2/k_1 = 0.01$, evidencing two buckling loads, one compressive and one tensile. Note the four points where the force vanishes.

to assume a certain F/δ relation is equivalent to assume a given dependence of F on ψ; therefore we introduce the dimensionless function

$$\beta(\psi) = \frac{l}{k} \, F(\delta(\psi)). \tag{2.16}$$

Employing Eq. (2.3) we obtain the condition

$$f(\psi) = \sqrt{1 - \psi^2} - \int_0^\psi \frac{\arcsin \gamma}{\beta(\gamma) \sqrt{1 - \gamma^2}} \, d\gamma \,, \tag{2.17}$$

satisfying $f(0) = 1$ and $f'(0) = 0$.

Three different profiles designed to obtain particular force F versus rotation ϕ postcritical behaviours (a sinusoidal, a circular and a constant) are sketched in Fig. 2.7. An interesting case is that of the neutral (or constant) postcritical behaviour, in which the rotation ϕ (and therefore
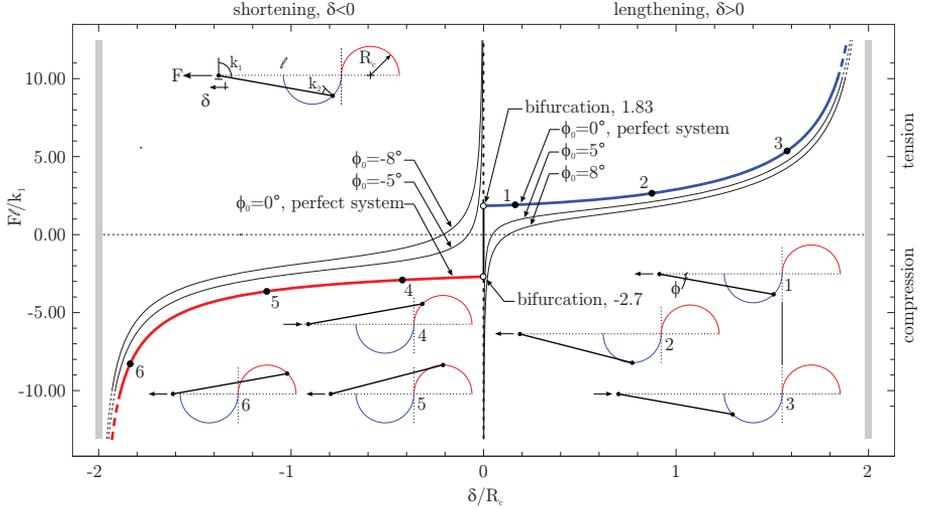
Figure 2.6: The force versus end-displacement behaviour of a single-degree-of-freedom structure, with an 'S-shaped' constraint, $\widehat{\chi} = \pm 4$, and $k_2/k_1 = 0.5$, evidencing two buckling loads, one compressive and one tensile. Note that at points labelled '2' and '5' the external force does not vanish.

also the displacement) can grow at constant load[4], which can be obtained employing the constraint profile expressed as

$$f(\psi) = \sqrt{1 - \psi^2} - \frac{1}{2\beta}\Big(\arcsin\psi\Big)^2 \quad \text{where} \quad \beta = \frac{F_{cr}l}{k}. \tag{2.18}$$

2.1.2 Experiments on one-degree-of-freedom elastic systems: multiple buckling and neutral postcritical response

The behaviours obtained employing the simple one-degree-of-freedom structures are not a mathematical curiosity, but can be realized in prac-

---

[4]A neutral postcritical behaviour has been found also by Gáspár (1984) employing a structural model completely different from that considered by us.
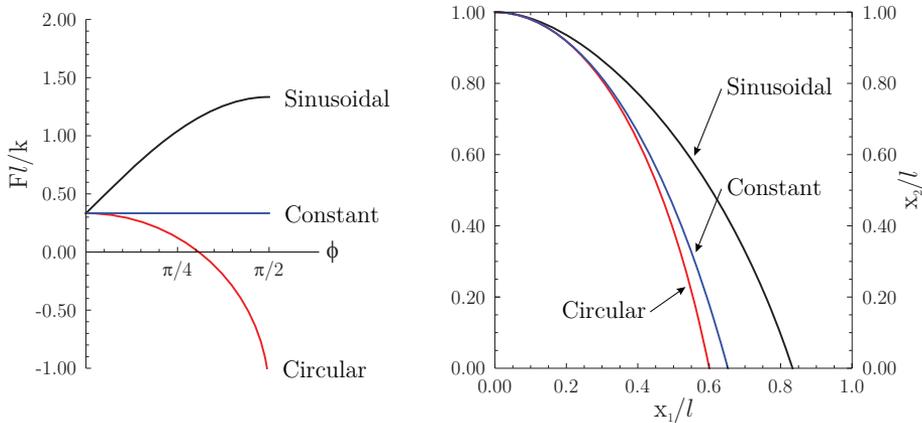
Fig. 2.7: Designed profiles (on the right) to obtain a given force-rotation postcritical response (on the left). The postcritical responses, given in terms of dimensionless force versus rotation of the structure are: sinusoidal, circular and constant (or 'neutral').

tice. In particular, we have realized the 'S-shaped' circular constraint shown in the inset of Fig. 2.2 and the profile illustrated in Fig. 2.7 (on the right, labelled 'constant'), the latter to show a 'neutral' or, in other words, 'constant-force', response. The experimental apparatuses are shown in Fig. 2.8 and in Fig. 2.9 (the former relative to the 'S-shaped' semi-circular profile, the latter to the profile providing the neutral post-critical response), where the grooves have been laser cut (by HTR Laser & Water cut, BZ, Italy) in a 2 mm thick plate of AISI 304 steel and the roller has been realized with a (17 mm diameter) steel cylinder mounted with two roller bearings (SKF-61801-2Z). The rigid bar 600 mm × 50 mm × 20 mm have been machined from an aluminium bar and lightened with longitudinal grooves (see Appendix A), so that its final mass is 820 gr. The hinge with rotational spring has been realized with three identical rotational springs, which have been designed using equations (32) of Brown (1981) and realized in (4 mm diameter) music wire ASTM A228, see Appendix A for further details.

Load/displacement curves are reported in Fig. 2.10 for the 'S-shaped' circular profile and in Fig. 2.11 for the profile giving the neutral response, as obtained from experiments, and directly compared with the theoretical
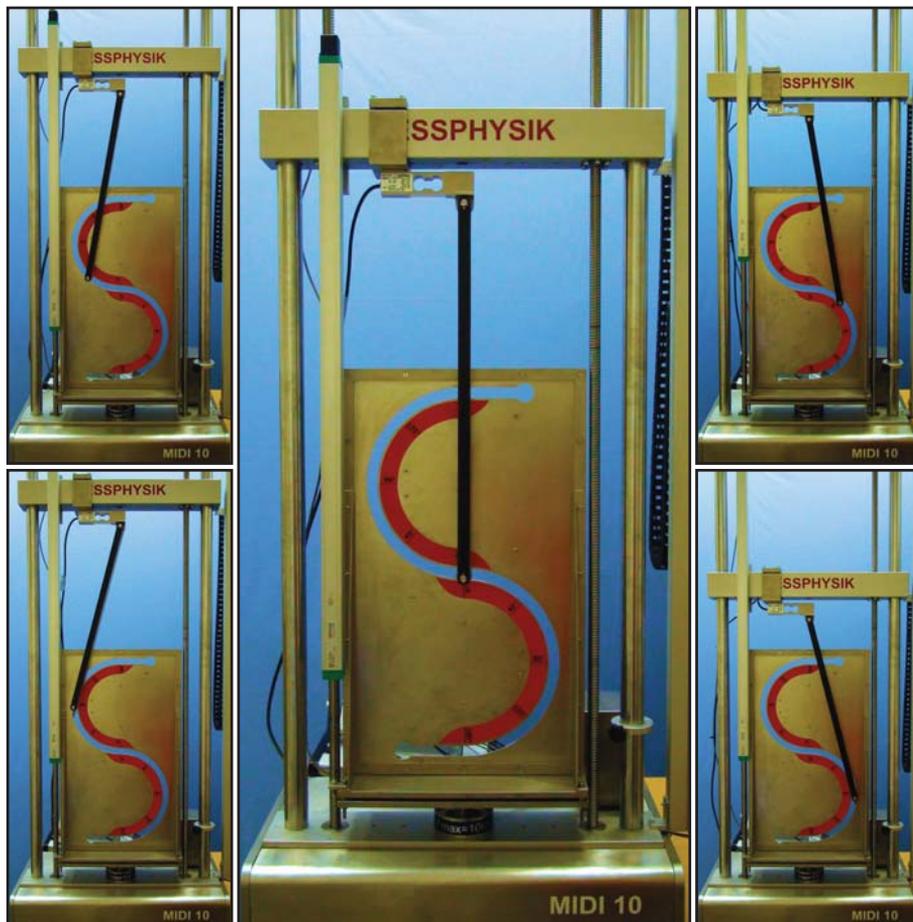
Fig. 2.8: Experimental set-up for the 'S-shaped' structure with a groove corresponding to two circles. Two photos taken during elongation (shortening) are reported on the left (on the right).

predictions. We note a nice agreement, with buckling detected prior to the attainment of the theoretical value, in agreement with the known effect of imperfections. Friction at the roller/profile contact has induced some irrelevant load oscillation, minimized by hand-polishing the edges of the groove and using Areo Lubricant AS 100 (from Rivolta s.p.a, Milano,
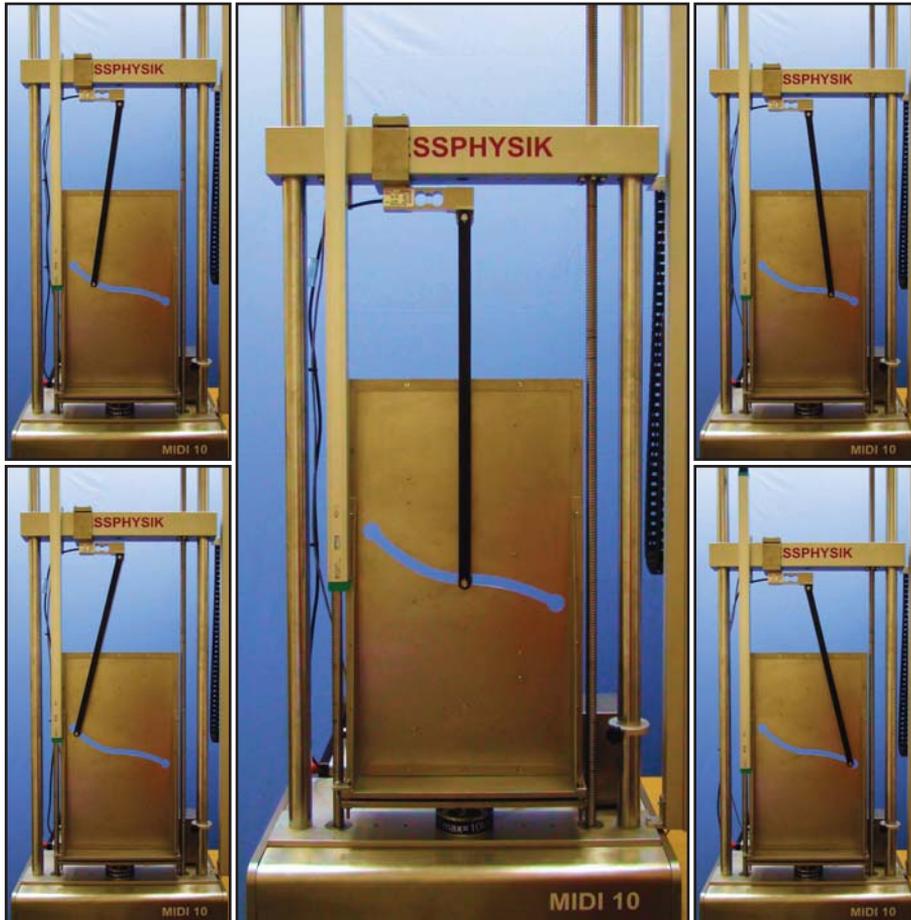
Fig. 2.9: Experimental set-up for the structure providing the neutral postcritical response. Two photos taken during elongation (shortening) are reported on the left (on the right).

Italy). We may finally comment that the experiments confirm the possibility of practically realizing mechanical systems behaving as the theoretical modelling predicts.

Fig. 2.10: Load/displacement experimental results versus theoretical prediction (dashed line) for a one-degree-of-freedom elastic structure having a rotational spring at one end, and a roller constrained to slide on an 'S-shaped', circular profile as shown in Fig. 2.8, together with the experimental set-up.

2.2 The buckling and postcritical behaviour of an elastic rod with a circular constraint on one end

We consider an *inextensible* elastic rod (of bending stiffness B and length l), with a movable clamp at one end, and having a rotational elastic spring (of stiffness k) on the other, which can slide on a circle centred on the axis of the rod, see the inset of Fig. 2.12. The rod is subject to an axial load F which may be tensile ($F > 0$) or compressive ($F < 0$).

42
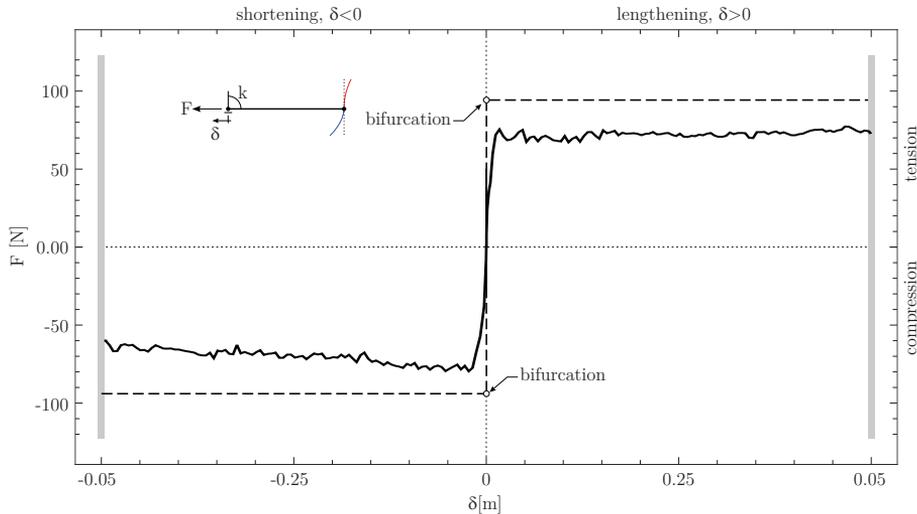
Fig. 2.11: Load/displacement experimental results versus theoretical prediction (dashed line) for a one-degree-of-freedom elastic structure designed to display a neutral postcritical behaviour. The structure has a rotational spring at one end, and a roller constrained to slide on the profile shown in Fig. 2.9, together with the experimental set-up.

2.2.1 The critical loads

The differential equilibrium equation of an elastic rod subject to an axial force F, linearized near the rectilinear configuration, is

$$\frac{d^4v(z)}{dz^4} - \alpha^2 \operatorname{sgn}(F) \frac{d^2v(z)}{dz^2} = 0, \tag{2.19}$$

where v is the transversal displacement, 'sgn' is defined as $\operatorname{sgn}(\alpha) = |\alpha|/\alpha$ $\forall \alpha \in \mathrm{Re} - \{0\}$, $\operatorname{sgn}(0) = 0$, and

$$\alpha^2 = \frac{|F|}{B}. \tag{2.20}$$

The general solution of Eq. (2.19) is

$$v(z) = \frac{C_1}{\alpha^2}\cosh(\sqrt{\mathrm{sgn}(F)}\,\alpha\,z) + \frac{C_2}{\alpha^2}\sqrt{\mathrm{sgn}(F)}\sinh(\sqrt{\mathrm{sgn}(F)}\,\alpha\,z) + C_3\,z + C_4,$$
(2.21)

and the boundary conditions [5] (the third involving the rotational spring stiffness k) are:

$$v(0) = \left.\frac{dv}{dz}\right|_{z=0} = 0,$$

$$-\frac{\mathrm{sgn}(F)}{\alpha^2}\left.\frac{d^3v}{dz^3}\right|_{z=l} = \phi + \left.\frac{dv}{dz}\right|_{z=l}, \tag{2.22}$$

$$-\frac{B}{k}\left.\frac{d^2v}{dz^2}\right|_{z=l} = \phi + \left.\frac{dv}{dz}\right|_{z=l},$$

plus the kinematic compatibility condition defining ϕ

$$\phi = \widehat{\chi}/lv(l), \tag{2.23}$$

involving the signed, dimensionless curvature $\widehat{\chi} = \pm l/R_c$ of the circle.

Imposing conditions (2.22)–(2.23), the solution (2.21) provides the condition for the critical loads

$$\left(\frac{1}{|\widehat{\chi}|} + \mathrm{sgn}(\widehat{\chi})\right)\alpha\,l\,\mathrm{sgn}(F)\cosh(\sqrt{\mathrm{sgn}(F)}\,\alpha\,l) - \mathrm{sgn}(\widehat{\chi})\sqrt{\mathrm{sgn}(F)}\sinh(\sqrt{\mathrm{sgn}(F)}\,\alpha\,l) +$$

$$+\frac{k}{B\alpha}\left[\left(\frac{1}{|\widehat{\chi}|} + \mathrm{sgn}(\widehat{\chi})\right)\alpha\,l\sqrt{\mathrm{sgn}(F)}\sinh(\sqrt{\mathrm{sgn}(F)}\,\alpha\,l) +\right.$$

$$\left.+\,\mathrm{sgn}(\widehat{\chi})\big(1 - \cosh(\sqrt{\mathrm{sgn}(F)}\,\alpha\,l)\big)\right] = 0,$$

(2.24)

corresponding in the two limits $k \to 0$ and $k \to \infty$ to a pinned and clamped constraint on the right end, respectively.

Buckling loads (made dimensionless through multiplication by $l^2/(\pi^2 B)$) are reported in Fig. 2.12 and in Figures 2.13 and 2.14, as functions of the signed radius of curvature $\widehat{\chi}$ of the constraint.

Results reported in the Figs. 2.13 and 2.14 (where the negative signs denote

---

[5] first: null displacement and rotation at the clamped end; second: shear force on the beam at the rotational spring; third: moment on the beam at the rotational spring
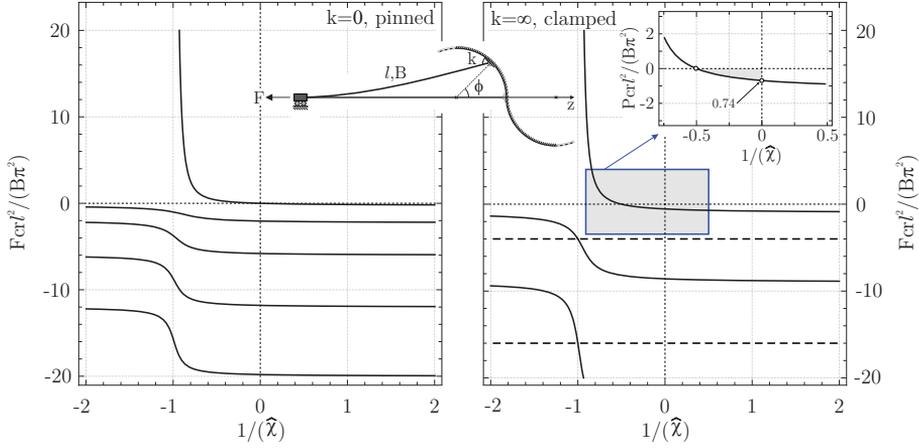
Fig. 2.12: Dimensionless buckling load F_{cr} (a negative sign denotes compression) of the structure sketched in the inset (clamped on the left end and sliding with a hinge, $k=0$, or guided, $k = \infty$, along a circle on the right end) as a function of the signed dimensionless curvature $\widehat{\chi}$ of the circle.

$1/\widehat{\chi}$	$\xi = l_0/l$	$F_{cr}l^2/(\pi^2 B)$		$1/\widehat{\chi}$	$\xi = l_0/l$	$F_{cr}l^2/(\pi^2 B)$
-0.20	3.5373	0.0799		0.20	4.5167	-0.0490
	0.7079	-1.9955		0.40	3.4916	-0.0820
-0.40	2.0773	0.2317		0.60	3.0741	-0.1058
	0.7228	-1.9139		0.80	2.8433	-0.1237
-0.60	1.2750	0.6151		1.00	2.6954	-0.1376
	0.7529	-1.7641		1.25	2.5707	-0.1513
-0.80	0.6284	2.5326		1.50	2.4845	-0.1620
	0.8289	-1.4556		2.00	2.3722	-0.1777
-1.00	-	∞		∞	2	-0.2500
	1	-1.0000				
-1.25	1.2222	-0.6694				
-1.50	1.3726	-0.5308				
-2.00	1.8312	-0.2982				
∞	2	-0.2500				
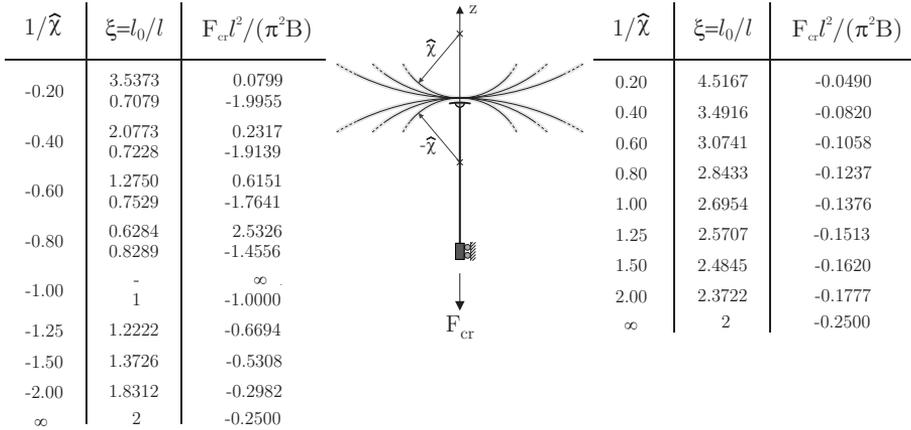
Fig. 2.13: Dimensionless buckling load F_{cr} of the structure sketched in the inset (clamped on one end and with a hinge sliding along a circle on the other) as a function of the signed dimensionless curvature $\widehat{\chi}$ of the circle. A negative sign denotes a compressive load.

45

$1/\widehat{\chi}$	$\xi=l_0/l$	$F_{cr}l^2/(\pi^2 B)$		$1/\widehat{\chi}$	$\xi=l_0/l$	$F_{cr}l^2/(\pi^2 B)$
-0.20	1.5372	-0.4232		0.20	1.2579	-0.6320
-0.40	2.2588	-0.1960		0.40	1.2053	-0.6884
-0.60	1.7689 / 0.5	0.3196 / -4.0000		0.60	1.1704	-0.7300
-0.80	0.6375 / 0.5	2.4608 / -4.0000		0.80	1.1459	-0.7616
-1.00	- / 0.5	∞ / -4.0000		1.00	1.1274	-0.7868
				1.25	1.1102	-0.8114
-1.25	0.6862	-2.1234		1.50	1.0969	-0.8312
-1.50	0.7742	-1.6682		2.00	1.0781	-0.8603
-2.00	0.8554	-1.3666		∞	1	-1.0000
-∞	1	-1.0000				
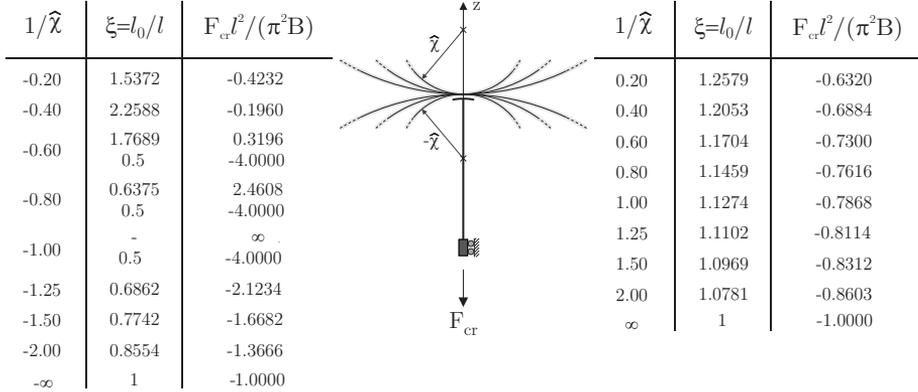
Fig. 2.14: Dimensionless buckling load F_{cr} of the structure sketched in the inset (clamped on one end and guided along a circle on the other end) as a function of the signed dimensionless curvature $\widehat{\chi}$ of the circle. A negative sign denotes a compressive load.

compressive loads) are given in terms of effective length factor ξ defined as

$$F_{cr} = \frac{\pi^2 B}{(\xi l)^2}. \tag{2.25}$$

We note from Figs. 2.12–2.14 that for certain curvatures of the constraint there is one buckling load in tension, while there are always infinite bifurcations in compression (so that we can comment that the bifurcation problem remains a Sturm-Liouville problem). The results reveal the strong effect of the constraint curvature, so that for instance for $\widehat{\chi} = -1/0.2$ (for $\widehat{\chi} = -1/0.8$) there is a buckling load in tension much smaller (much higher) than that in compression, taken in absolute value. Moreover, for $\widehat{\chi} = -1/1.25$, but also for all positive curvatures $\widehat{\chi} > 0$, there is no tensile bifurcation.

2.2.2 The elastica

The shape of the constraint has a strong effect on the postcritical behaviour, as will be shown below with reference to the case of the circular profile. This effect can be exploited for the design of compliant mechanisms, so that the solution of this problem is not only of academic interest. Therefore, we derive the solution for an elastic rod clamped to the left and constrained on the right to slide with a rotational spring (of stiffness k_r) on a 'S–shaped' bi-circular profile, as sketched

in Fig. 2.15, where the local reference system to be used in the analysis is also indicated.
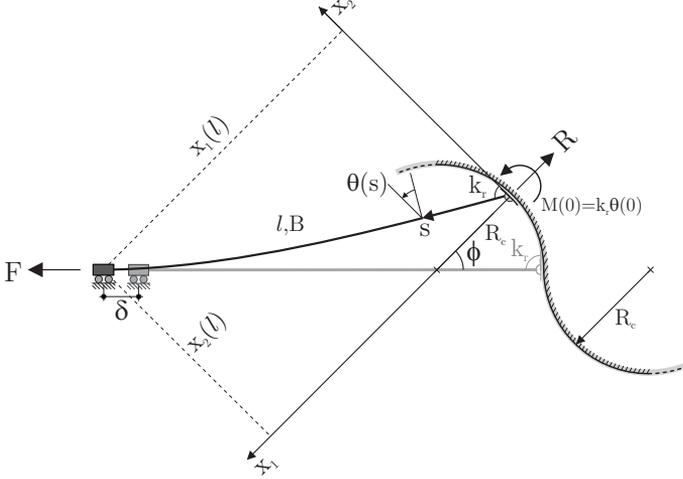
Fig. 2.15: The elastic line problem for a rod clamped at the left end and constrained to slide with a rotational spring (of stiffness k_r) on a circle at the right end. Note the reference system employed in the analysis.

The elastic line problem is governed by the following equations.

i.) A condition of kinematic compatibility can be obtained by observing from Fig. 2.15 that the coordinates of the elastica evaluated at $s = l$, namely, $x_1(l)$ and $x_2(l)$, are related to the angle of rotation of the local reference system ϕ and to the radius R_c of the constraint via

$$[x_1(l) \mp R_c] \tan \phi - x_2(l) = 0, \qquad (2.26)$$

where ϕ is assumed positive if anticlockwise; note that in Eq. (2.26) the sign '$-$' ('$+$') holds for the case of the rotational spring lying on the left (right) half–circle.

ii.) The curved constraint transmits to the rod a moment and a force pointing the centre of the circle, in other words, parallel to x_1 and assumed positive when opposite to the direction of the x_1–axis, so that for $0 \leq \phi < \pi/2$ ($\pi/2 < \phi \leq \pi$) it corresponds to a positive tensile (negative compressive) dead force F applied to the structure defined by

$$F = R \cos \phi. \qquad (2.27)$$

iii.) Through introduction of the curvilinear coordinate s, the fully nonlinear equation of the elastica governing deflections of the rod is

$$\frac{d^2\theta}{ds^2} - \frac{R}{B}\sin\theta = 0, \tag{2.28}$$

where θ is the rotation angle (assumed positive if clockwise) of the normal at each point of the elastica, so that with the symbols introduced in Fig. 2.15 we find the condition

$$\theta(l) = \phi. \tag{2.29}$$

Integration of Eq. (2.28) from 0 to s, after multiplication by $d\theta/ds$, leads to

$$\left(\frac{d\theta}{ds}\right)^2 = 2\,\tilde{\alpha}^2\left[\frac{2}{k^2} - 1 - \mathrm{sgn}(R)\cos\theta\right], \tag{2.30}$$

where

$$\tilde{\alpha}^2 = \frac{|R|}{B}, \qquad k^2 = \frac{4\tilde{\alpha}^2}{[\theta(0)\,k_r/B]^2 + 2\tilde{\alpha}^2\,[\mathrm{sgn}(R)\cos\theta(0) + 1]}, \tag{2.31}$$

in which the term $\theta(0)\,k_r$ corresponds to the moment evaluated at $s = 0$. The introduction of the change of variable

$$\beta = [\theta - \mathrm{H}(R)\,\pi]/2, \tag{2.32}$$

where H denotes the Heaviside step function, allows to re-write Eq. (2.30) as

$$\left(\frac{d\beta}{ds}\right)^2 = \frac{\tilde{\alpha}^2}{k^2}\left(1 - k^2\sin^2\beta\right), \tag{2.33}$$

so that a second change of variable $u = s\tilde{\alpha}/k$ yields

$$\frac{d\beta}{du} = \pm\sqrt{1 - k^2\sin^2\beta}. \tag{2.34}$$

Restricting the treatment to the case '+', which corresponds to $\theta(0) \geq 0$, and since $\beta = \beta(0)$ at $u = 0$, Eq. (2.34) provides the following solution for β

$$\beta = \mathrm{am}\left[u + \mathrm{F}\left[\beta(0), k\right], k\right], \tag{2.35}$$

where am and F are the Jacobi elliptic function amplitude and the incomplete elliptic integral of the first kind of modulus k, respectively (Byrd and Friedman, 1971). Keeping into account that $dx_1/ds = \cos\theta$ and $dx_2/ds = \sin\theta$, an integra-

tion provides the two coordinates x_1 and x_2 of the elastica expressed in terms of u as

$$
\begin{cases}
x_1 = \mathrm{sgn}(R)\,\dfrac{2}{k\tilde{\alpha}}\{(1 - k^2/2)u + \mathrm{E}\left[\beta(0), k\right] - \mathrm{E}\left[\mathrm{am}\left[u + \mathrm{F}\left[\beta(0), k\right], k\right], k\right]\}, \\[4mm]
x_2 = \mathrm{sgn}(R)\,\dfrac{2}{k\tilde{\alpha}}\{\mathrm{dn}\left[u + \mathrm{F}\left[\beta(0), k\right], k\right] - \mathrm{dn}\left[\mathrm{F}\left[\beta(0), k\right], k\right]\},
\end{cases}
\tag{2.36}
$$

in which the constants of integration are chosen so that x_1 and x_2 vanish at $s = 0$. In Eqs. (2.36) dn is the Jacobi elliptic function delta-amplitude of modulus k, while E is the incomplete elliptic integral of the second kind (Byrd and Friedman, 1971). Eqs. (2.36) generalize the expressions derived in Chapter 1 [equations (1.30) and (1.31)], which are recovered when $\theta(0) = 0$.

The horizontal displacement δ of the clamp on the left of the structure (assumed positive for a lengthening of the system) is given in the form

$$
\delta = \frac{x_2}{\sin\phi} - l \mp R_c,
\tag{2.37}
$$

where, as for Eq. (2.26), the sign '$-$' ('$+$') holds for the case of the rotational spring lying on the left (right) half–circle.

The axial load F can be obtained as a function of the rotation ϕ, or as a function of the end displacement δ, through the following steps.

i.) A value for $\theta(0)$ is fixed, so that k can be expressed using Eqs. (2.31) as a function of R;

ii.) the expressions (2.36) for the coordinates of the elastica and Eq. (2.35), evaluated at $s = l$, become functions of R only;

iii.) Eq. (2.29) provides ϕ, so that Eq. (2.26) becomes a nonlinear equation in the variable R, which can be numerically solved (we have used the function FindRoot of Mathematica$^{®}$ 6.0);

iv.) once R is known, F, ϕ and δ can be respectively obtained from Eqs. (2.27), (2.29) and (2.37).

The postcritical behaviour (corresponding to the first modes branching from both tensile and compressive critical loads) of the structure is reported in Fig. 2.16 in terms of dimensionless axial load $4Fl^2/(B\pi^2)$ versus dimensionless displacement δ/R_c, for the particular case of a roller sliding on the profile, $k_r = 0$.

We note that the elastica obtained in this case is *inflexional* and therefore different from that reported in Chapter 1, moreover, the postcritical behaviour
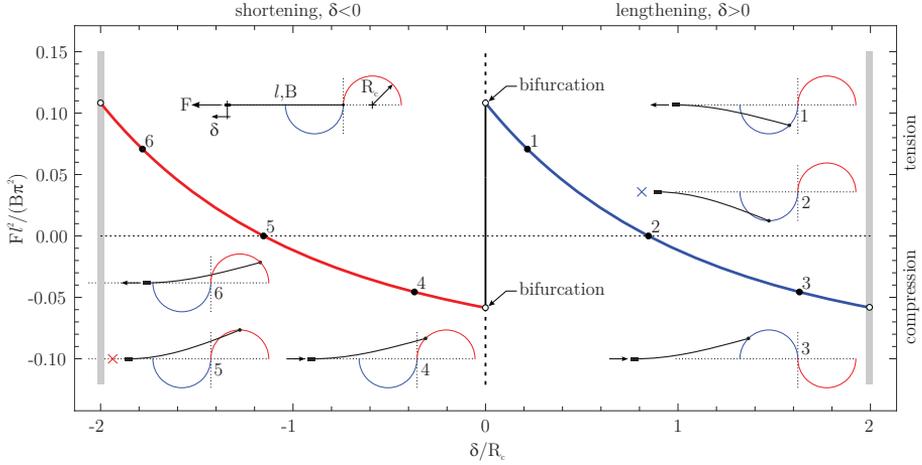
Fig. 2.16: The postcritical behaviour of the structure sketched in the inset (with a roller sliding on the 'S-shaped' profile) corresponding to the first mode under tensile and compressive loads. Dimensionless axial load F versus dimensionless end displacement.

is always unstable, evidencing decrease of the load with increasing edge displacement ('softening'). Special features of the postcritical behaviour (already present in the one-degree-of-freedom system) are (i.) that there is a transition from a tensile (a compressive) to a compressive (to a tensile) elastica when the constraint reaches the points denoted with '2' and '5' in the graph, and that (ii.) the postcritical branches emanating from the critical loads are the same, but horizontally shifted.

2.2.3   Experiments on the elastica

We have tested the behaviour of an elastic rod by employing the same experimental set-up used for testing the one-degree-of-freedom structures in Sect. 2.1.2, but with the rigid system replaced by elastic rods realized with two 250 mm × 25 mm × 4 mm C72 carbon-steel strips (Young modulus 200 GPa, mass 968 gr), see Appendix A for details. The experimental set-up with photos taken during the tests is shown in Fig. 2.17. These experiments represent *the practical realization of a designed compliant mechanism*.

Experimental results are reported in Fig. 2.18 in terms of theoretical (dashed line) versus experimental force/end-displacement data.   Moreover, the photos reported in Fig. 2.19, which are details of the photos shown in Fig. 2.17 on the
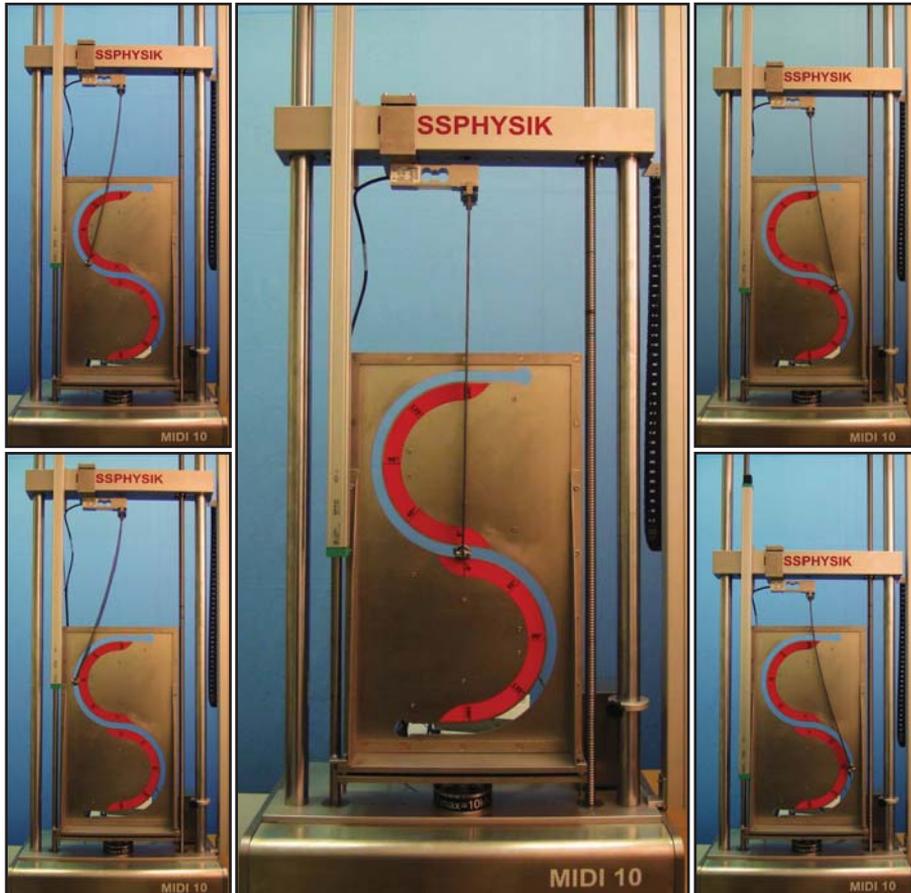
Fig. 2.17: Deformed shapes of the elastica during a test of a beam sliding on an 'S-shaped', circular profile. Two photos taken during elongation (shortening) are reported on the left (on the right). Note that the system represents a compliant mechanism of designed response.

left and on the right, are compared with the theoretical shape of the elastica [shown with a white dashed line and obtained from Eqs. (2.36)] at two different end angles (45° and 90° for tension and compression).

From the figures, we can observe the following facts.

- The experiments definitely substantiate theoretical findings.
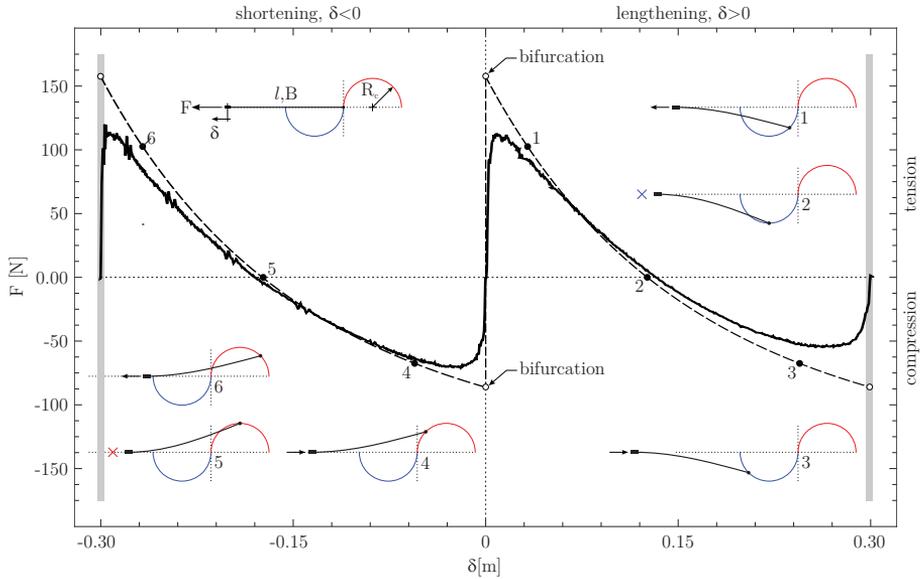
Fig. 2.18: Load/displacement experimental results versus theoretical prediction (dashed line) for a beam sliding on an 'S-shaped', circular profile (see the inset).

• The comparison between the deformed beam during a test and the predictions of the elastica, shown in Fig. 2.19, reveals a very tight agreement between theory and experiments.

As for the one-degree-of-freedom systems, we can again conclude that the experiments confirm the possibility of practically realizing elastic systems behaving in strict agreement with theoretical predictions.
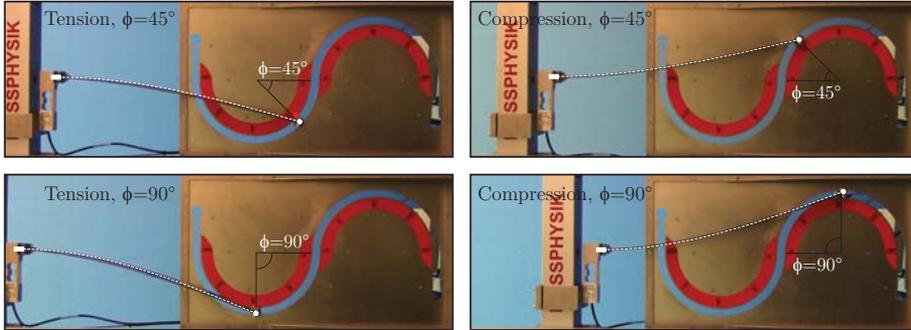
Fig. 2.19: Deformed shapes of the elastica (compared with the theoretical predictions reported with a white dashed line) during the test shown in Fig. 2.17 of a beam with a roller sliding on an 'S-shaped', circular profile.

Details on the experiments

A Midi 10 (10 KN maximum force, from Messphysik Materials Testing) electromechanical testing machine has been employed to impose displacements (velocity 0.2 mm/s) at the ends of the structures. Loads and displacements have been measured with the loading cell and the displacement transducer mounted on the Midi 10 machine, and, independently, with a MT 1041 (0.5 kN maximum load) load cell (from Mettler-Toledo) and a potentiometric displacement transducer Gefran LTM-900-S IP65.

The rotational springs employed for the one-degree-of-freedom systems have been designed to provide a stiffness equal to 211.5 Nm by employing equations (32) of Brown (1981). After machining, the springs have been tested and found to correspond to a stiffness equal to 169.5 Nm, the value which has been used to compare experiments with theoretical results.

An IEPE accelerometer (PCB Piezotronics Inc., model 333B50) has been attached at one end of the structure to precisely detect the instant of buckling. This has been observed in all tests to correspond to an acceleration peak ranging between 0.15 and 0.2 g, while before buckling and during postcritical behaviour the acceleration did not exceed the value 0.003 g.

Data from the load cell MT 1041, the displacement transducer Gefran LTM-900-S IP65, and the accelerometer PCB 333B50 have been acquired with a system NI CompactDAQ, interfaced with Labview 8.5.1 (National Instruments), while acquisition of the data from the Midi 10 has been obtained from a Doli EDC 222 controller.

Temperature near the testing machine has been monitored with a thermocou-

ple connected to a Xplorer GLX Pasco and has been found to lie around 22°C, without sensible oscillations during tests.

Photos have been taken with a Nikon D200 digital camera, equipped with AF Nikkor (18-35mm 1:3.5-4.5 D) lens (Nikon Corporation) and movies have been recorded during the tests with a Sony handycam (model HDR-XR550VE). The testing set-up is shown in Fig. 2.20. Additional material is available at http://ssmg.unitn.it/.
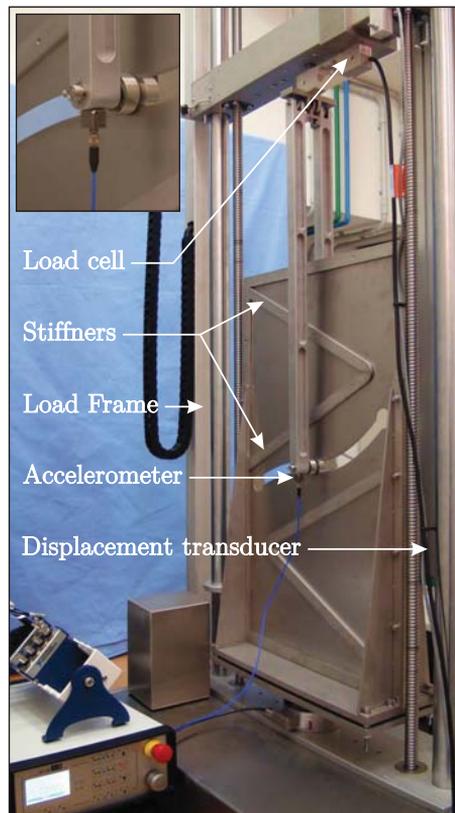
Fig. 2.20: The experimental set-up for the buckling tests, seen from the back.

3

Eshelby-like forces acting on elastic structures: theoretical and experimental proof

The Eshelbian (or configurational) force is the main concept of a celebrated theoretical framework associated with the motion of dislocations and, more in general, defects in solids. In a similar vein, in an elastic structure where a (smooth and bilateral) constraint can move and release energy, a force driving the configuration is generated, which therefore is called by analogy 'Eshelby-like' or 'configurational'. This force (generated by a specific movable constraint) is derived both via variational calculus and, independently, through an asymptotic approach. Its action on the elastic structure is counterintuitive, but is fully substantiated and experimentally measured on a model structure that has been designed, realized and tested. These findings open a totally new perspective in the mechanics of deformable mechanisms, with possible broad applications, even at the nanoscale.

Configurational (or: 'material', 'driving', 'non-Newtonian') forces have been introduced by Eshelby (1951; 1956; 1970; 1975) to describe the fact that massless (for instance: voids, microcracks, vacancies, or dislocations) or heavy (for instance inclusions) defects may move within a solid body as a result of mechanical or thermal loading. The Eshelbian force is defined as the negative gradient of the total potential energy $\mathcal{V}$ of a body with respect to the parameter κ determining the configuration of the defect, namely, $-\partial\mathcal{V}(\kappa)/\partial\kappa$.

Examples are the crack-extension force of fracture mechanics, the Peach–Koehler force of dislocations, or the material force developing on a phase boundary in a solid under loading. Nowadays configurational forces are the cornerstone of a well-developed theory (see for instance the monographs by Gurtin, 2000, Kienzler and Herrmann, 2000, Maugin, 1993, 2011, and the journal special issues by Dascalu et al., 2010, and Bigoni and Deseri, 2011).

Let us consider an elastic structure in equilibrium upon load and assume that a (frictionless and bilateral) constraint can move –a feature which may be

considered as a 'defect'– in a way to allow the system to reconfigure through a release of elastic energy, then a force is generated, similar to an Eshelbian or configurational[1] one.

To reveal this force in an indisputable way, and directly measure it, the simple elastic structure sketched in Fig. 3.1 has been designed, which inflection length can change through sliding along a sleeve and therefore discloses (in two different and independent ways, namely, using variational and asymptotic approaches) the presence of an Eshelby-like force. The structure has been subsequently realized and instrumented (see Fig. 3.2, reporting a series of photos demonstrating the action of the Eshelby-like force), so that the configurational force has been measured at equilibrium and it is shown to perfectly match the theoretical predictions.
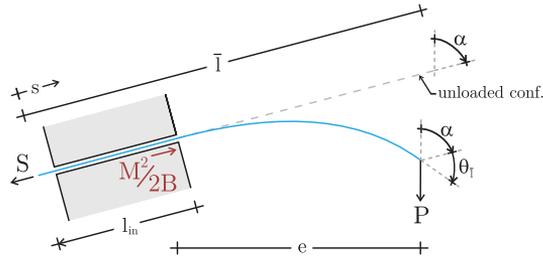
Figure 3.1: Structural scheme of the elastic system employed to disclose a Eshelby-like force. The elastic rod of total length $\bar{l}$ is subject to a dead vertical load P on its right end, is constrained with a sliding sleeve inclined at an angle α (with respect to the vertical) and has a axial dead force S applied at its left end. The presence of the Eshelby-like force $M^2/(2B)$ influences the force S at equilibrium, which results different from $P\cos\alpha$.

In this example configurational forces are non-zero, but small for small deflections[2] and become progressively important when displacements grow. Their effects are counterintuitive and unexpected, so that for instance, the structure shown in Fig. 4.6, which can (wrongly!) be thought to be unable to provide any axial action, is instead subject to an axial Eshelby-like force transmitted by the sliding sleeve. In particular, at the end of the sliding sleeve, the axial force S at

---

[1]'Configurational force' is not to be confused with the follower forces analyzed for instance by Bigoni and Noselli, (2011).

[2]The fact that these forces are small for small displacement does not mean that they are always negligible, since their action is in a particular direction, which may be 'unexpected'. For instance, in the case of null axial dead load, $S = 0$, and sliding sleeve orthogonal to the vertical dead load P, $\alpha = \pi/2$ (Fig. 4.28), the Eshelby-like force is the only axial action, so that equilibrium becomes impossible.
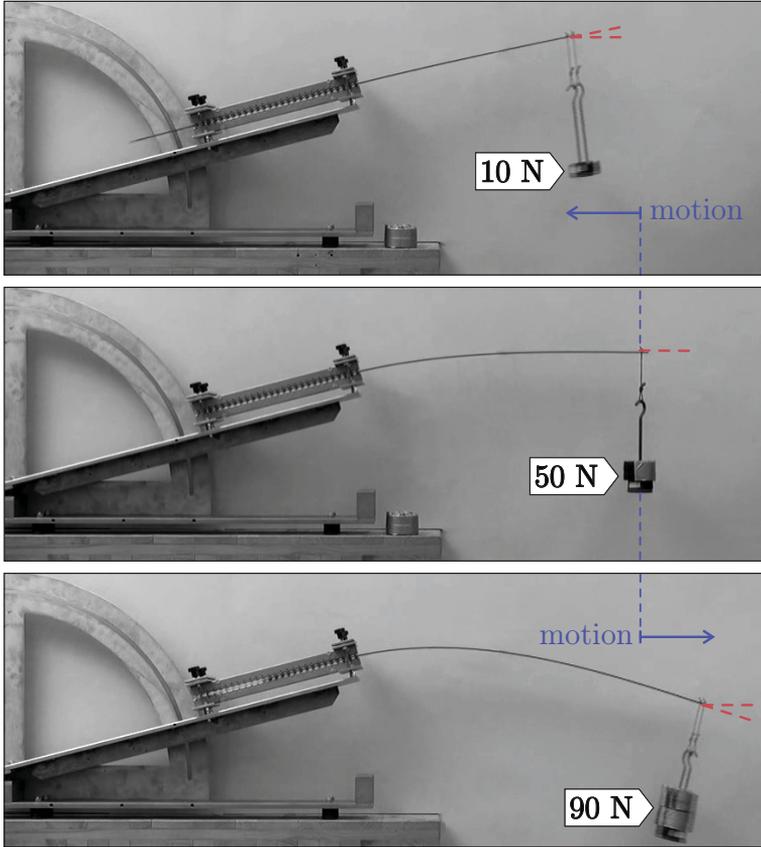
Figure 3.2: The practical realization of the elastic structure shown in Fig. 3.1 reveals an axial Eshelby-like force, so that, while at low vertical force (10 N) the elastic rod tends, as expected, to slip inside the sliding sleeve (upper photo), at 50 N the equilibrium is surprisingly possible (note that the tangent at the loaded end of the elastic rod is horizontal, see the photo in the centre) and at 90 N the elastic rod is expelled from the sliding sleeve (lower photo), even if the system is inclined at 15° with respect to the horizontal ($\alpha = 75°$).

equilibrium with a load P (inclined of α with respect to the rod's axis) is not simply equal to $-P\cos\alpha$, as when the sliding sleeve is replaced by a movable clamp, but will be determined (Section 3.1.3) to be a function of the rotation of

the rod at its end, $\theta_{\bar{l}}$, as

$$S = -P\cos\left(\alpha + \theta_{\bar{l}}\right) = -P\cos\alpha + \underbrace{2P\left(\sin^2\frac{\theta_{\bar{l}} + \alpha}{2} - \sin^2\frac{\alpha}{2}\right)}_{Eshelby-like\,force}, \qquad (3.1)$$

which for for small deflections $(\sin\theta_{\bar{l}} \approx \theta_{\bar{l}})$ becomes

$$S = -P\cos\alpha + \underbrace{P\frac{3\,v_{\bar{l}}}{2(\bar{l} - l_{in})}\sin\alpha}_{Eshelby-like\,force}, \qquad (3.2)$$

where $v_{\bar{l}}$ is the transversal displacement at the loaded end of the rod of length $\bar{l} - l_{in}$ (external to the sliding sleeve). Eqs (3.1) and (3.2) show that there is an 'unexpected' term (null if the elastic rod is constrained by a movable clamp instead of a sliding sleeve), defined as the 'Eshelby-like force'. Although there is a little abuse of notation[3], this definition is motivated by the fact that the Eshelby-like force is null, would the total potential energy of the system be independent of a configurational parameter.

The findings presented in this article demonstrate that movable constraints applied to elastic structures can generate configurational forces and that these become dominant when deformations are sufficiently large. Configurational forces can be employed in the design of new deformable systems with challenging characteristics, which may find applications even at the micro- and nano-scale, for instance, to control growth of a structural element.

3.1 Eshelby-like force produced by a sliding sleeve

An inextensible elastic rod (straight in its unloaded configuration, with bending stiffness B and total length $\bar{l}$) has one end constrained with a sliding sleeve, is subject to an edge axial (dead) force S, and has the other end subject to a dead transversal load P (inclined at an angle α, see Fig. 3.1). Introducing the curvilinear coordinate $s \in [0, \bar{l}]$, the length l_{in} of the segment of the rod internal to a (frictionless, perfectly smooth and bilateral) sliding sleeve, and the rotation $\theta(s)$ of the rod's axis, it follows that $\theta(s) = 0$ for $s \in [0, l_{in}]$. Denoting by a prime the derivative with respect to s, the bending moment along the elastic rod is $M(s) = B\theta'(s)$, so that at the loaded edge of the rod, we have the zero-moment boundary condition $\theta'(\bar{l}) = 0$.

---

[3]The introduction of the nomenclature 'Eshelby-like force' allows to distinguish terms generated by the possibility of configurational changes of the system, while 'Eshelby forces' must always vanish at equilibrium.

The total potential energy of the system is

$$
\begin{aligned}
\mathcal{V}(\theta(s), l_{in}) = \quad & B \int_{l_{in}}^{\bar{l}} \frac{\left[\theta'(s)\right]^2}{2} ds - P\left[\bar{l} - \cos\alpha \int_{l_{in}}^{\bar{l}} \cos\theta(s) ds \right. \\
& \left. + \sin\alpha \int_{l_{in}}^{\bar{l}} \sin\theta(s) ds \right] - S\, l_{in},
\end{aligned}
\tag{3.3}
$$

which at equilibrium becomes

$$
\begin{aligned}
\mathcal{V}(\theta_{eq}(s, l_{eq}), l_{eq}) = \quad & B \int_{l_{eq}}^{\bar{l}} \frac{\left[\theta'_{eq}(s, l_{eq})\right]^2}{2} ds - P\left[\bar{l} - \cos\alpha \int_{l_{eq}}^{\bar{l}} \cos\theta_{eq}(s, l_{eq}) ds \right. \\
& \left. + \sin\alpha \int_{l_{eq}}^{\bar{l}} \sin\theta_{eq}(s, l_{eq}) ds \right] - S\, l_{eq},
\end{aligned}
\tag{3.4}
$$

where l_{eq} is the length of the elastic rod inside the sliding sleeve and θ_{eq} the rotation of the rod's axis at the equilibrium configuration.

The Eshelbian force related to the sliding in the sleeve can be calculated by taking the derivative with respect to l_{eq} of the total potential energy at equilibrium, eqn (3.4). In particular, keeping into account integration by parts

$$
\theta'_{eq} \frac{\partial \theta'_{eq}}{\partial l_{eq}} = \left(\theta'_{eq} \frac{\partial \theta_{eq}}{\partial l_{eq}}\right)' - \theta''_{eq} \frac{\partial \theta_{eq}}{\partial l_{eq}},
\tag{3.5}
$$

the equilibrium of the elastica

$$
B\theta''_{eq}(s) + P\left[\cos\alpha \sin\theta_{eq}(s) + \sin\alpha \cos\theta_{eq}(s)\right] = 0, \qquad s \in [l_{eq}, \bar{l}]
\tag{3.6}
$$

and the boundary condition $\theta'_{eq}(\bar{l}) = 0$, we arrive at the following expression for the Eshelby force

$$
-\frac{\partial \mathcal{V}(l_{eq})}{\partial l_{eq}} = B\frac{[\theta'_{eq}(l_{eq})]^2}{2} + B\theta'_{eq}(l_{eq}) \left.\frac{\partial \theta_{eq}}{\partial l_{eq}}\right|_{s=l_{eq}} + P\cos\alpha + S.
\tag{3.7}
$$

The fact that θ_{eq} is a function of $s - l_{eq}$ and of the angle of rotation of the beam at the loaded end $\theta_{\bar{l}}$ (function itself of l_{eq}), but is always zero at $s = l_{eq}$ for all

$\theta_{\bar{l}}$, yields

$$\left.\frac{\partial \theta_{eq}}{\partial l_{eq}}\right|_{s=l_{eq}} = -\theta'_{eq}(l_{eq}), \tag{3.8}$$

so that the vanishing of the derivative with respect to l_{eq} of the total potential energy, eqn (3.7), represents the axial equilibrium

$$\underbrace{\frac{M^2}{2B}}_{Eshelby-like\,force} = S + P\cos\alpha, \tag{3.9}$$

where $M = B\theta'_{eq}(l_{eq})$ is the reaction moment, equal to Pe, where e is the load eccentricity (to the sliding sleeve).

Although the Eshelby force must vanish at equilibrium, the contribution $M^2/(2B)$ is a 'counterintuitive term' which depends on the configurational parameter l_{eq} (and would be absent if the elastic rod would be constrained with a movable clamp instead than a sliding sleeve) and is for this reason indicated as the 'Eshelby-like force'. This term has wrongly been neglected by a number of authors who have considered sliding sleeve constraints, while a term $M^2/(2B)$ correctly enters in calculations referred in a different context, namely, adhesion mechanics, in which it is equated to an 'adhesion energy' (Majidi, 2007; Majidi et al. 2012).

Since equilibrium is only possible when eqn (3.9) is satisfied, the presence of the Eshelby-like force (parallel to the direction of sliding) explains the reason why the equilibrium is possible for the configuration shown in the central photo in Fig. 3.2 and why the rod is 'expelled' from the sliding sleeve in the lower photo.

In the next sections the existence of the Eshelby-like force (3.9) will be demonstrated via two different and independent approaches (an asymptotic method and a variational technique).

3.1.1 Asymptotic approach

The Eshelbian force (3.9) can be obtained via an asymptotic approach. This has been found in a forgotten article published in Russian by Balabukh et al. (1970). The main idea is to consider an imperfect sliding sleeve (Fig. 3.3) having a small gap Δ (the distance between the two rigid, frictionless and parallel surfaces realizing the sliding device), so that the perfect sliding sleeve case is recovered when the gap is null, $\Delta = 0$. Within this space, the elastic rod is deflected, so that $\vartheta(\Delta)$ denotes the angle at its right contact point, where the forces H, V, M are applied. The length of the rod detached from the two surfaces representing the imperfect sliding sleeve is denoted with $a(\Delta)$. The frictionless contact generates

the reaction forces R and Q, in equilibrium with the axial dead force S at the other end. For small Δ, the equilibrium is given by

$$Q = \frac{M}{a(\Delta)}, \qquad R = V + \frac{M}{a(\Delta)}, \qquad S = \left(V + \frac{M}{a(\Delta)}\right)\vartheta(\Delta) - H. \qquad (3.10)$$

On application of the virtual work for a linear elastic inextensible rod yields the geometric quantities $a(\Delta)$ and $\vartheta(\Delta)$

$$a(\Delta) = \sqrt{\frac{6B\Delta}{M}}, \qquad \vartheta(\Delta) = \frac{1}{2}\sqrt{\frac{6M\Delta}{B}}, \qquad (3.11)$$

so that forces Q, R and S can be written as

$$Q = M\sqrt{\frac{M}{6B\Delta}}, \qquad R = V + M\sqrt{\frac{M}{6B\Delta}}, \qquad S = \frac{M^2}{2B} + \frac{V}{2}\sqrt{\frac{6M\Delta}{B}} - H. \quad (3.12)$$

In the limit of perfect (zero-thickness) sliding sleeve, $\Delta \to 0$, the horizontal component of the reaction R *does not vanish, but* becomes the Eshelbian force (3.9)

$$\lim_{\Delta \to 0} R(\Delta)\vartheta(\Delta) = \frac{M^2}{2B}. \qquad (3.13)$$
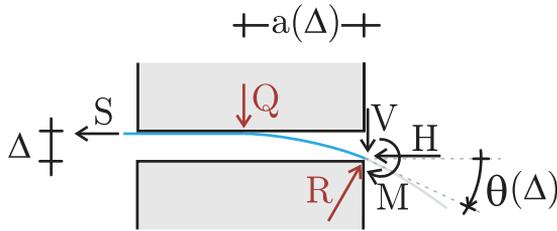
Figure 3.3: Deformed configuration of an elastic rod within an imperfect sliding sleeve made up of two smooth, rigid and frictionless planes placed at a distance Δ. Applied and reaction forces provide in the limit $\Delta \to 0$ the Eshelby-like force.

3.1.2 Variational approach

The total potential energy (3.3) has a movable boundary l_{in}, so that it is expedient (Courant and Hilbert, 1953, see also Majidi et al. 2012) to introduce a small parameter ϵ and take variations (subscript '*var*') of an equilibrium con-

figuration (subscript '*eq*') in the form

$$\theta(s, \epsilon) = \theta_{eq}(s) + \epsilon\theta_{var}(s), \qquad l_{in}(\epsilon) = l_{eq} + \epsilon l_{var} \ , \qquad (3.14)$$

with the boundary conditions

$$\theta_{eq}(l_{eq}) = 0, \quad \theta(l_{eq} + \epsilon l_{var}) = 0, \quad \theta'_{eq}(\bar{l}) = 0. \qquad (3.15)$$

A Taylor series expansion of $\theta(l_{in})$ for small ϵ yields

$$\theta(l_{eq} + \epsilon l_{var}, \epsilon) = \quad \theta_{eq}(l_{eq}) + \epsilon\left(\theta_{var}(l_{eq}) + \theta'_{eq}(l_{eq})l_{var}\right)$$
$$+ \frac{\epsilon^2}{2}l_{var}\left(2\theta'_{var}(l_{eq}) + \theta''_{eq}(l_{eq})l_{var}\right) + \mathcal{O}\left(\epsilon^3\right), \qquad (3.16)$$

so that the boundary conditions (3.15) lead to the following compatibility equations

$$\theta_{var}(l_{eq}) + \theta'_{eq}(l_{eq})l_{var} = 0, \quad 2\theta'_{var}(l_{eq}) + \theta''_{eq}(l_{eq})l_{var} = 0. \qquad (3.17)$$

Taking into account the Leibniz rule of differentiation and the boundary (3.15) and compatibility (3.17) conditions, through integration by parts, the first variation of the functional $\mathcal{V}$ is

$$\delta_\epsilon \mathcal{V} = \quad -\int_{l_{eq}}^{\bar{l}}\left[B\theta''_{eq}(s) + P\left(\cos\alpha\sin\theta_{eq}(s) + \sin\alpha\cos\theta_{eq}(s)\right)\right]\theta_{var}(s)ds$$
$$+\left[B\frac{\theta'_{eq}(l_{eq})^2}{2} - P\cos\alpha - S\right]l_{var},$$
$$(3.18)$$

so that the equilibrium equations (3.6) and (3.9) are obtained, the latter of which, representing the so-called 'transversality condition' of Courant and Hilbert (1953), provides the Eshelby-like force.

3.1.3 The Eshelby-like force expressed as a function of the transversal load

The equilibrium configuration of the elastic rod satisfies the elastica equation (3.6) (see Love, 1927, and Bigoni, 2012) and, through a change of variables, the

rotation field (for the first mode of deformation) can be obtained as

$$\theta_{eq}(s) = 2 \arcsin \left[\eta \operatorname{sn} \left((s - l_{eq}) \sqrt{\frac{P}{B}} + \mathcal{K}(m, \eta), \eta \right) \right] - \alpha, \tag{3.19}$$

where sn is the Jacobi sine amplitude function, $\mathcal{K}(m, \eta)$ the incomplete elliptic integral of the first kind and

$$\eta = \sin \frac{\theta_{\bar{l}} + \alpha}{2}, \qquad m = \arcsin \left[\frac{\sin(\alpha/2)}{\eta} \right], \tag{3.20}$$

with $\theta_{\bar{l}} = \theta_{eq}(\bar{l})$ representing the rotation measured at the free end of the rod, related to the applied vertical load through

$$P = \frac{B}{(\bar{l} - l_{eq})^2} \left[\mathcal{K}(\eta) - \mathcal{K}(m, \eta) \right]^2. \tag{3.21}$$

The Eshelby-like force (3.9) can be expressed as

$$\frac{M^2}{2B} = 2P \left(\eta^2 - \sin^2 \frac{\alpha}{2} \right), \tag{3.22}$$

so that the axial force S at the end of the sliding sleeve, which will be measured through a load cell in the experiments, is given by eqn (3.1). It can be noted from eqn. (3.1) that the measured load S is (in modulus) bounded by P and that S tends to P only in the 'membrane limit', when B tends to zero and $\theta_{\bar{l}} + \alpha$ to π.

The following three different cases may arise, explaining the experiments shown in Fig. 3.2.

- the elastic rod within the sliding sleeve is in compression, or 'pushed in', if $\theta_{\bar{l}} + \alpha < \pi/2$;

- the elastic rod within the sliding sleeve is unloaded if $\theta_{\bar{l}} + \alpha = \pi/2$;

- the elastic rod within the sliding sleeve is in tension, or 'pulled out', if $\theta_{\bar{l}} + \alpha > \pi/2$.

The case of null axial force, $S = 0$, occurs when $M^2/(2B)$ is equal to the axial component of the dead load, $P \cos \alpha$, and corresponds to deformed configurations which have the tangent at the free end orthogonal to the direction of the dead load P, as in Fig. 3.2 (center).

Finally, it can be noted that the Eshelby-like force $M^2/(2B)$ is greater than

the applied load P when

$$\cos\alpha - 2\cos^2\left(\frac{\theta_{\bar{l}}+\alpha}{2}\right) > 0. \tag{3.23}$$

Regions in the $\theta_{\bar{l}}-\alpha$ plane where the axial force S is positive/negative and where $M^2/(2B) > P$ are shown in Fig. (3.4). From the figure it can be concluded that $M^2/(2B) > P$ is possible only for positive axial load, $S > 0$, and high deflections of the rod (at least for rotation at the free end $\theta_{\bar{l}}$ greater than $\pi/3$ and depending on α).
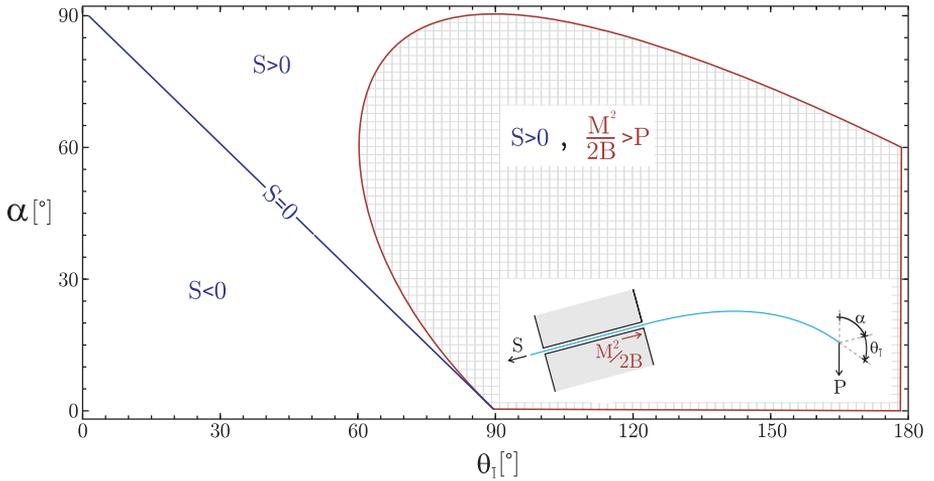
Figure 3.4: Regions in the plane $\theta_{\bar{l}} - \alpha$ where $S > 0$, $S < 0$ and $M^2/(2B) > P$.

3.2 The experimental evidence of configurational force

The structure shown in Fig. 3.1 has been realized using for the elastic rod two C62 carbon-steel strips (25 mm × 2 mm cross section), one 585 mm in length and the other 800 mm. For these rods the bending stiffness B has been determined with flexure experiments to be equal to 2.70 Nm².

The sliding sleeve is 384 mm in length and has been realized with 32 pairs of rollers (made up of 10 mm diameter and 15 mm length teflon cylinders, each containing two roller bearings). The tolerance between the metal strip and the rollers is calibrated with four micrometrical screws.

The axial force S has been measured using a MT1041 load cell (R.C. 300N), while dead loading, measured through a Leane XFTC301 (R.C. 500N) loading cell, has been provided with a simple hydraulic device in which water is poured at constant rate of 10 gr/s into a container. Data have been acquired with a NI CompactDAQ system, interfaced with Labview 8.5.1 (National Instruments). The whole apparatus has been mounted on an optical table (1HT-NM from Standa) to prevent spurious vibrations, which have been checked to remain negligible (accelerations have been found inferior to 2×10^{-3} g) with four IEPE accelerometer (PCB Piezotronics Inc., model 333B50) attached at different positions. The tests have been performed in a controlled temperature (20±0.2 °C) and humidity (48±0.5%) room. The testing set-up is shown in Fig. 3.5. Additional material can be found at http://ssmg.unitn.it/.
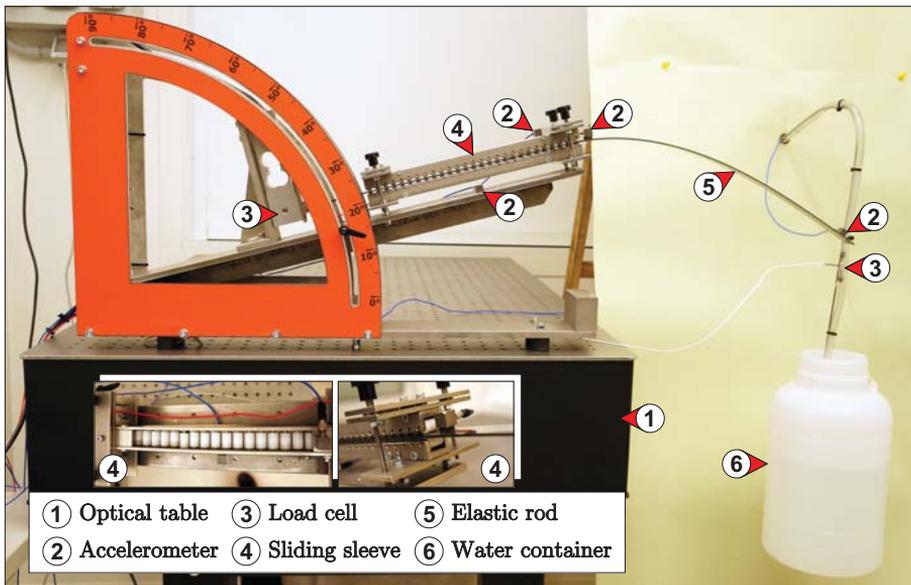
Figure 3.5: The test setup for the measure of the axial Eshelby-like force transmitted by a sliding sleeve, a realization of the scheme reported in Fig. 3.6.

3.2.1 Eshelbian force provided by a roller device

Rollers have been employed in the practical realization of the sliding sleeve, so that the question may arise how this set-up is tight to our idealization and can effectively measure the Eshelby-like force. To quantify the effects introduced

by the rollers, an asymptotic approach similar to that presented in Section 3.1.1 is developed here by considering the statically determined system given by two rollers with finite radius r and which centers are distant $\Delta_H + 2r$ and $\Delta_V + 2r$ in the axial and transversal directions, so that the model of a perfect sliding sleeve is achieved in the limit of null value for these three parameters (r, Δ_H and Δ_V), Fig. 3.6.
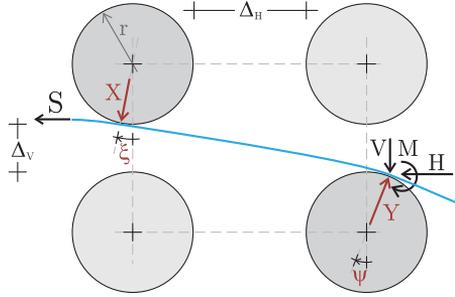
Figure 3.6: The scheme of the sliding sleeve constraint realized through two pairs of rollers.

In the limit $\Delta_V/\Delta_H \to 0$, the roller reactions X and Y are obtained from rotational and translational (in the transversal direction) equilibrium as

$$X = \frac{M}{\cos\xi\left[\Delta_H + r\left(2 + \sin\psi + \sin\xi\right)\right]},$$

$$Y = \frac{1}{\cos\psi}\left[V + \frac{M}{\Delta_H + r\left(2 + \sin\psi + \sin\xi\right)}\right], \tag{3.24}$$

where ξ and ψ are the rotations of the rod at the contact points with the rollers, so that the translational (in the axial direction) equilibrium leads to

$$S = V\tan\psi - \frac{M\left(\tan\xi - \tan\psi\right)}{\Delta_H + r\left(2 + \sin\psi + \sin\xi\right)} - H. \tag{3.25}$$

Restricting attention to small deflections between the rollers, the angles ξ and ψ

can be obtained through integration of the elastica as

$$\xi = -\frac{M(\Delta_H + 2r)^2 (2B + Mr) + 6B(-2B + Mr)\Delta_V}{2B(\Delta_H + 2r)(6B + Mr)},$$

$$\psi = \frac{M(\Delta_H + 2r)^2 (4B + Mr) + 6B(2B + Mr)\Delta_V}{2B(\Delta_H + 2r)(6B + Mr)}. \tag{3.26}$$

In the limit of $\Delta_V/r \to 0$, eqn (3.26) simplifies to

$$\xi = -\frac{M(\Delta_H + 2r)(Mr + 4B)}{2B(Mr + 6B)}, \quad \psi = -\xi, \tag{3.27}$$

and the translational equilibrium, eqn. (3.25), reads

$$\underbrace{\frac{M}{6B + Mr}\left[\frac{6M(3B + Mr)}{6B + Mr} + \frac{V(\Delta_H + 2r)(4B + Mr)}{2B}\right]}_{Eshelby-like force} = S + H, \tag{3.28}$$

an equation which introduces the concept of Eshelby-like force provided by a roller device, and reducing in the limits $r \to 0$ and $\Delta_H \to 0$ to the value of the Eshelby-like force (3.9) arising from a sliding sleeve.

It can be noted that the lowest value of the configurational force realized by the roller device occurs in the limit of the sliding sleeve.

3.2.2 Experiments

Results of experiments are reported in Fig. 3.7 and compared with the theoretical predictions obtained with the 'perfect model' of sliding sleeve, eqn (3.9), and with the 'roller-version' of it, eqn (3.28), the latter used with parameters tailored on the experimental set up ($r = 5$ mm, $\Delta_H = 1$ mm).

First of all, we can note that the theoretical values are close to each other, which is a proof that the rollers have a negligible effect on the determination of the Eshelby-like force. Moreover, we see that there is an excellent agreement between the theoretical predictions and the experimental results, which is an indisputable proof that Eshelby-like forces acting on elastic structures are a reality.
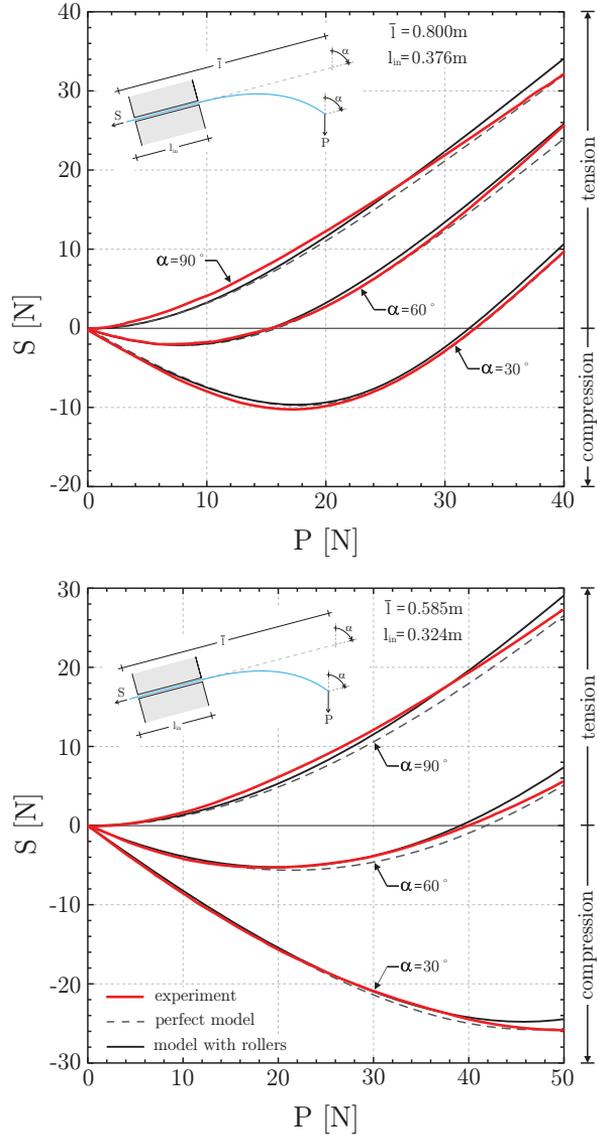
Figure 3.7: Comparison between experimental results (red curve) and the theoretical predictions. These have been reported for a perfect sliding sleeve (dashed curve) and for a sliding sleeve realized with rollers mimicking the experimental conditions (solid curve). Two rods have been used of external lengths 261 mm (left) and 424 mm (right) for different inclinations (90°, 60° and 30°).

4

Instability of a penetrating blade

Application of a dead compressive load at the free end of an elastic rod (the 'blade') induces its penetration into a sliding sleeve ending with a linear elastic spring. Bifurcation and stability analysis of this simple elastic system shows a variety of unexpected behaviours: (i.) an increase of buckling load at decreasing of elastic stiffness; (ii.) a finite number of buckling loads for a system with infinite degrees of freedom (leading to a non-standard Sturm-Liouville problem); (iii.) more than one bifurcation loads associated to each bifurcation mode; (iv.) a restabilization of the straight configuration after the second bifurcation load associated to the first instability mode; (v.) the presence of an Eshelby-like (or configurational) force, deeply influencing stability. Only the first of these behaviours was previously known, the second and third ones disprove common beliefs, the fourth highlights a sort of 'island of instability', and the last one shows surprising phenomena and effects on stability.

Despite the common belief that structural instability is a fully mature field of mechanics, it has recently been shown that it is still possible to discover new and 'unexpected' phenomena in the critical and postcritical behaviour of simple structures, such as tensile buckling (Zaccaria et al., 2011), buckling inducing shrinking of a structure (Shim et al., 2012), multiple bifurcations in single degree of freedom structures (see Chapter 2), frictional flutter instability (Bigoni and Noselli, 2011), and that buckling can be exploited to facilitate adhesion (Chan et al., 2008), or to create flexible electronics (Rogers et al., 2010), or to switch a phononic band gap (Bertoldi and Boyce, 2008), or to induce a pattern transformation (Li et al., 2012).

The aim of the present article is to explore the critical and postcritical behaviour of a simple elastic structure, displaying several unexpected effects, some of which were previously known but received only marginal attention (Feodosyev, 1977; Tarnai, 1980), while others were simply unknown. The importance of the mechanical features highlighted and discovered in the present article lies in the fact that they disprove common believes (for instance, engineers believe that critical loads always increase with the stiffness of a structure, and mathematicians that a bifurcation problem of an elastic rod is always a Sturm-Liouville prob-

lem), correct errors in several published works (where the so-called 'Eshelby-like force' is wrongly omitted in the calculations), provide a new understanding of the adhesion energy between a structure and a substrate (Majidi, 2007; Majidi et al., 2012), and open the way to unconventional mechanical applications, as for instance to continuous self-restabilizing systems (a simple example of this behaviour, restricted to a system with two degrees of freedom, is reported by Potier-Ferry, 1987). The considered mechanical problem is the following.

A blade (an elastic planar rod) is forced to penetrate into an elastic movable clamp (a frictionless sliding sleeve with a final linear spring) through the application of a dead compressive load at the other edge, Fig. 4.1.
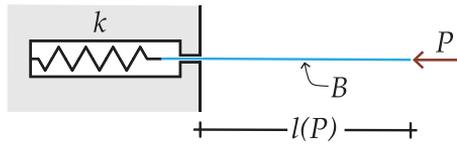
Figure 4.1: The penetrating blade is an elastic planar rod whose free length l is a function of the amount of the applied axial load P. The blade with constant bending stiffness B has a free end subject to the dead load P, while at the other edge the blade slides into a frictionless sleeve and is restrained by an axial linear spring of stiffness k.
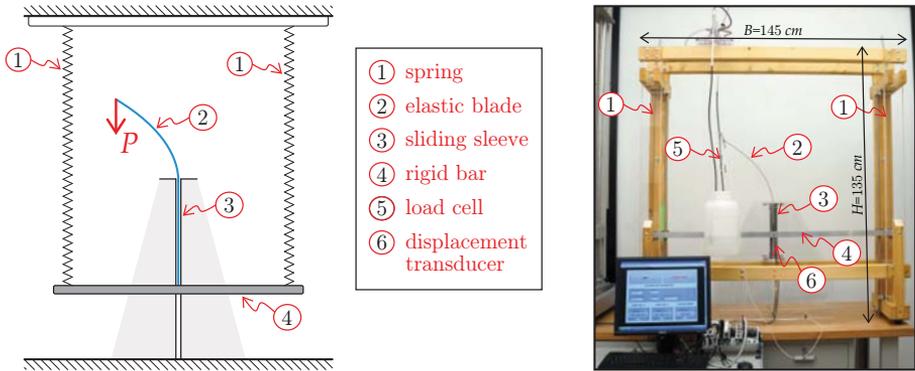
Figure 4.2: Left: the design scheme employed to realize the structure shown in Fig. 4.1 and right: its practical realization (prototype 1). Note that the sliding sleeve is borne by a transparent plexiglass support (represented grey on the left). Details of the experimental setup are given in Sect. 4.4.

This system is shown to exhibit several surprising and counterintuitive me-

chanical behaviours, theoretically predicted by elastic analysis and experimentally confirmed through a physical model (Fig. 4.2, for details of the experimental setup see Sect. 4.4). These are as follows.

- (i.) The buckling load of the system is governed by the relative spring/bending stiffness, so that *an increase of elastic stiffness of the spring yields a decrease in the buckling load.* Moreover, if the stiffness of the spring is low enough compared to the rod's bending stiffness ('highly compliant' system), there will be no buckling, but only a straight penetration into the sliding sleeve. In these conditions an *increase in the elastic stiffness of the spring* may induce buckling, see Fig. 4.3 showing that for infinite stiffness (lower part) of the spring the blade buckles, while for highly compliant spring (lower part) the blade does not.

  Previously, this effect was theoretically noticed by Feodosyev (1977) and on a simpler structure by Tarnai (1980).

- (ii.) Buckling of an elastic rod (with ordinary boundary conditions, e.g. doubly pinned) is governed by a Sturm-Liouville problem (Broman, 1970), admitting an infinite number of bifurcation loads. This is commonly associated to the fact that the system 'has infinite degrees of freedom'. Although the system shown in Fig. 1 is continuous, the moving boundary introduced by the sliding sleeve leads to a non-standard Sturm-Liouville problem, so that a *finite* number of buckling loads is found.

- (iii.) Usually, a compressed elastic rod (with ordinary boundary conditions, e.g. doubly pinned) evidences one bifurcation load of the fundamental equilibrium path associated to each bifurcation mode (secondary bifurcations emanating from the postcritical path, as for instance in the case of the doubly-pinned rod, see Bigoni, 2012, Section 1.13.1, are not considered now). The structure shown in Fig. 4.1 displays *two* (actually three, but one of these will be shown to be physically not accessible) *bifurcation loads for the straight configuration associated to each bifurcation mode*, a situation occurring also in the simpler system analyzed by Bigoni (2012, Section 1.13.4).

- (iv.) In usual structural systems, stability of the fundamental path is lost after buckling and is never 'later' recovered. Differently, the straight configuration of the structure, stable at small load (Fig. 4.4, upper part on the right), returns to be stable (Fig. 4.4, lower part on the right) at load sufficiently higher than that corresponding to buckling (more precisely, higher than the load corresponding to a second bifurcation of the fundamental path). This situation occurs also in the simpler systems analyzed
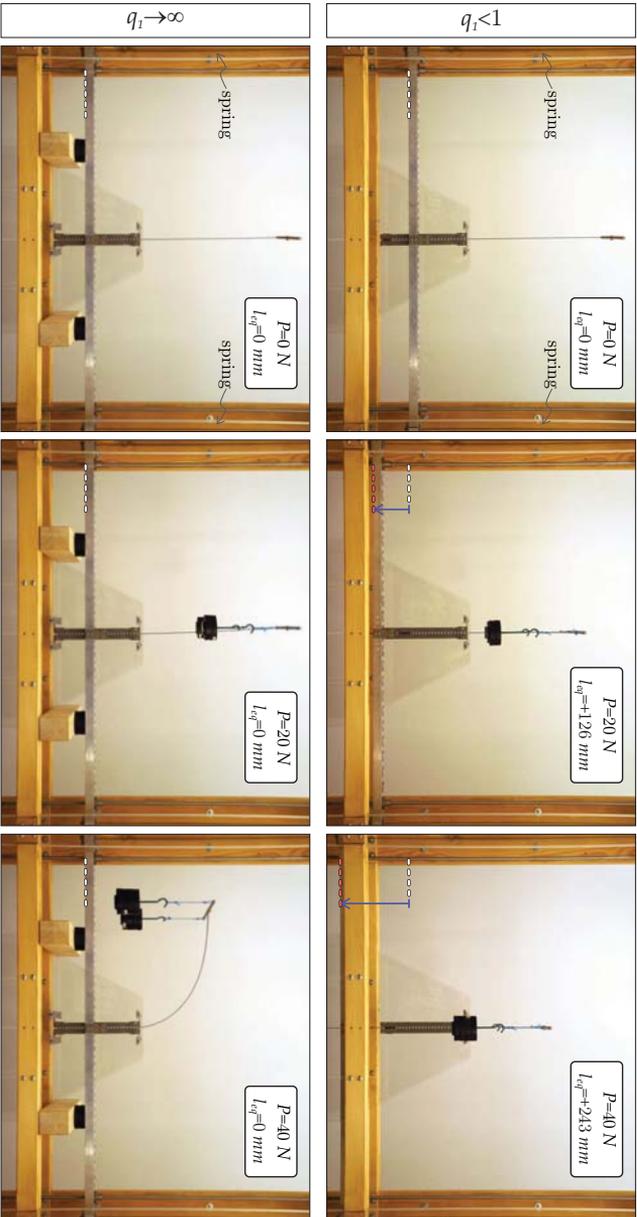
Figure 4.3: A blade (an elastic planar rod) subject to a dead compressive load P on an edge does not evidence buckling when can penetrate into a sliding sleeve restrained by springs (upper part, so-called 'highly compliant system', $q_1 < 1$). The same blade buckles when it is clamped at the lower edge (lower part, $q_1 \rightarrow \infty$). This model (which can be better understood by analyzing the scheme reported in Fig. 4.2) shows that an increase of stiffness (the lower clamp is infinitely stiff when compared with the springs restraining the penetration into the sliding sleeve) may lower the buckling load. The length of the blade inside the sliding sleeve at equilibrium is l_{eq}, while q_1 is the dimensionless relative stiffness defined by eq. (4.7).

by Bigoni (2012, Section 1.13.4) and Potier-Ferry (1987).[1]
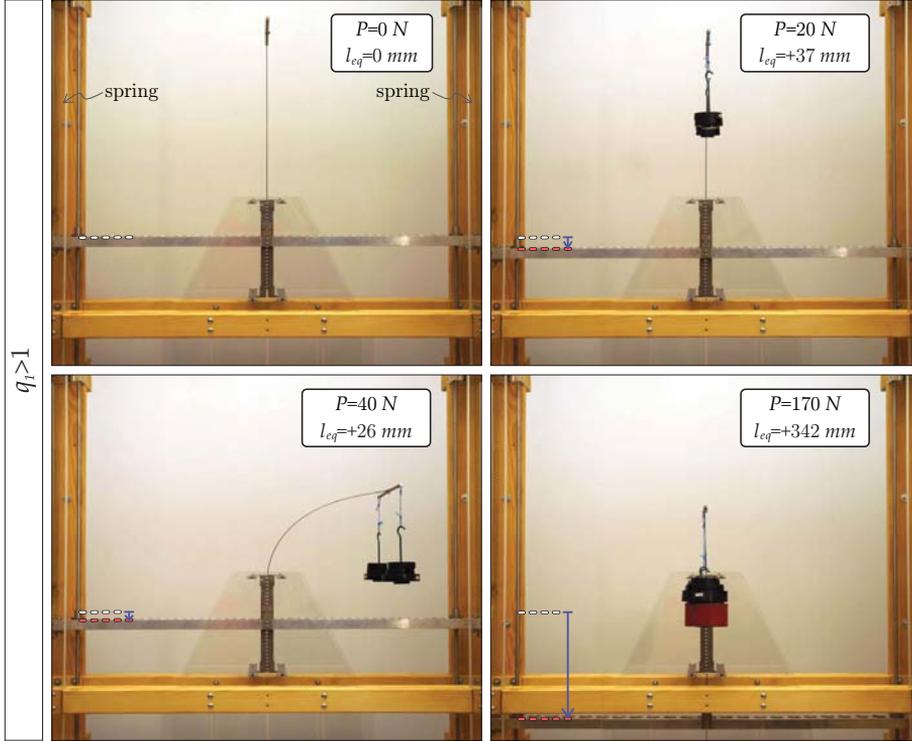
Figure 4.4: The straight configuration for the blade (elastic planar rod) is stable at small load (upper part, right), becomes unstable at higher load (lower part, left) and, for further increase, it eventually returns stable (lower part, right). The structural model has been realized following the scheme reported in Fig. 4.2. The length of the blade inside the sliding sleeve at equilibrium is l_{eq}, while q_1 is the dimensionless relative stiffness defined by eq. (4.7).

- (v.) In Chapter 3 we have shown that a sliding sleeve constraining the edge of an elastic rod may induce Eshelby-like (or 'configurational'[2]) forces in

---

[1]For monotonically increasing loading the structure buckles and does not 'spontaneously' return in the straight configuration. Therefore, the system has to be set in this configuration to observe its stability beyond the second buckling load.

A system that spontaneously self-restabilizes has been shown by Potier-Ferry, 1987.

[2]These forces have been named by Bigoni et al. (2013) from Eshelby since they can

structures, generated by the fact that the rod, freely sliding at one edge, can change its length and therefore release elastic energy. The presence of an Eshelby-like (or configurational) force produced by the sliding sleeve in the structure shown in Fig. 4.1 strongly affects the post-critical behaviour and its stability. The effects of this force can be counterintuitive, so that the springs in the structure shown in Fig. 4.5 at low load (upper part on the right, $P = 20N$) are subject to an *higher* elongation than that occurring when a higher load P is applied (lower parts on the left, $P = 30N$, and on the right, $P = 40N$).

The existence of this Eshelby-like force (erroneously ignored by a number of authors in previous articles) becomes even more evident in the photo shown in Fig. 4.6, because in the absence of this *vertical* force the equilibrium would be impossible (note that this configuration for the structure is unstable, as will be proven in Sect. 4).

All the above five features are demonstrated in this article, both theoretically and experimentally. In particular, points (i.)–(iii.) are analyzed through a standard bifurcation analysis and integration of the planar elastica. Points (iv.) and (v.) are investigated by using a variational formulation, which allows to confirm the existence of an Eshelby-like force (through consideration of the first variation) and to address stability (through consideration of the second variation).

4.1 More than one critical load for each instability mode and finite number of critical loads for continuous elastic systems

Let us consider an inextensible elastic beam with constitutive behaviour defined by the Euler-Bernoulli equation

$$M(s) = B\frac{d\theta(s)}{ds},$$ (4.1)

where B is the constant bending stiffness, $\theta(s)$ is the angle of inclination of the tangent to the elastica at the curvilinear coordinate s. The Euler formula provides the n-th critical load (associated to the n-th instability mode) for an elastic clamped-free planar rod of length l as

$$P_{cr,n} = \frac{(2n-1)^2\pi^2 B}{4l^2}, \qquad n \in \mathbb{N}^+.$$ (4.2)

be understood as the derivative of the total potential energy of the system with respect to the configurational parameter characterizing the system, in strict analogy with the concept of Eshelbian force (Eshelby, 1956). 'Configurational force' has here a different meaning than the 'follower' force considered by Bigoni and Noselli (2011).
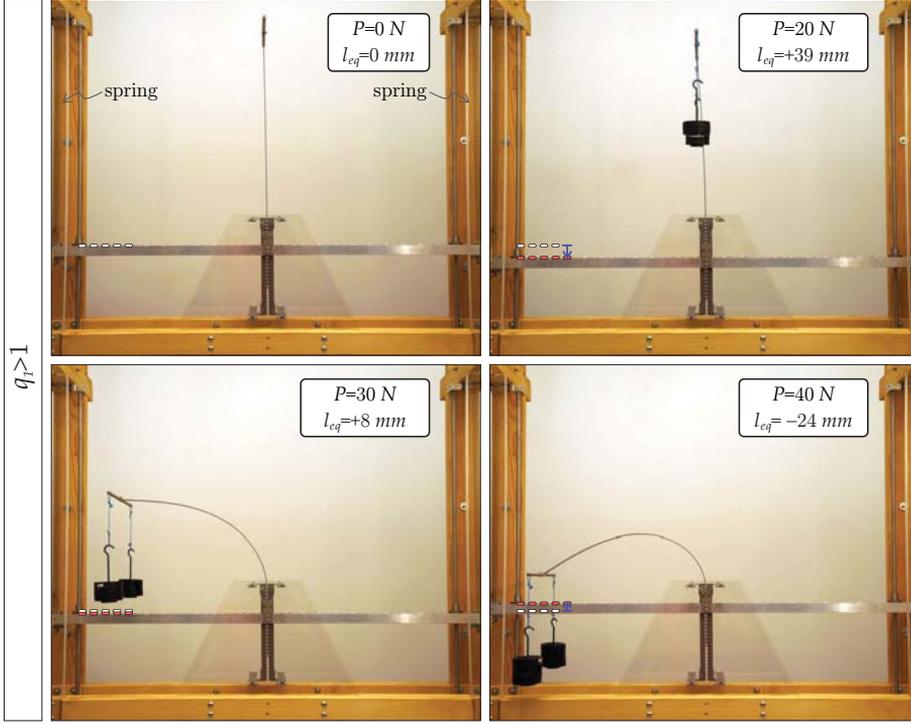
Figure 4.5: An Eshelby-like force is generated when the blade (elastic planar rod) buckles, so that the length of the rod inserted into the sliding sleeve (l_{eq}) decreases when the applied compressive load P is increased. As a consequence, the length of the rod inside the sliding sleeve can become even smaller than in the unloaded configuration (i.e. $l_{eq} < 0$, lower part, right) with the increasing of the compressive load. This counterintuitive effect is due to the presence of an vertical upward Eshelie-like force generated by the sliding sleeve which is greater than the vertical downward load P. The structural model has been realized following the scheme reported in Fig. 4.2. The length of the blade inside the sliding sleeve at equilibrium is l_{eq}, while q_1 is the dimensionless relative stiffness defined by eq. (4.7).

Eq. (4.2) shows that the n-th critical load P_{cr} is unique whenever the beam length l is fixed, but this uniqueness may be lost when the length becomes a function of the applied axial load, $l = l(P)$.

If, as shown in Fig. 4.1, a sliding sleeve with an axial spring replaces the clamp, so that the elastic planar rod (or 'blade') can penetrate into the constraint of an amount l_{eq} (the index 'eq' indicates a value at equilibrium), $l(P)$ is given

Figure 4.6: The vertical and upward Eshelby-like force (equal and opposite to the
applied downward load) generated by the sliding sleeve makes the equilibrium config-
uration possible, even if unstable. Note that the tangent to the end of the blade is
horizontal, as will be theoretically rationalized in Sect. 4.2.

by

$$l(P) = \bar{l} - l_{eq}(P), \tag{4.3}$$

where $\bar{l}$ is the outer length of the blade at null axial load P, $l(P = 0) = \bar{l}$. In the
particular case of a linear spring with stiffness k and considering the blade in the
straight configuration the equilibrium equation in the axial direction is given by

$$P = k l_{eq}, \tag{4.4}$$

(an equation that does not hold when the curvature at the point $s = l_{eq}$ is
different from zero, $\theta'_{eq}(l_{eq}) \neq 0$, Sect. 4.2) so that the length of the outer part
of the blade is $l(P) = \bar{l} - P/k$ and the Euler formula (4.2) becomes

$$P_{cr,n} = \frac{(2n-1)^2 \pi^2 B}{4 \left(\bar{l} - \dfrac{P_{cr,n}}{k} \right)^2}, \qquad n \in \mathbb{N}^+. \tag{4.5}$$

The solution for the critical load $P_{cr,n}$ from eq. (4.5) leads to the following cubic

equation

$$p_{cr,n}^3 - 2p_{cr,n}^2 + p_{cr,n} - \frac{4}{27q_n} = 0, \qquad n \in \mathbb{N}^+, \tag{4.6}$$

where $p_{cr,n}$ and q_n are respectively the dimensionless n-th critical load and dimensionless relative stiffness (spring stiffness multiplied by the bar length and divided by a critical load) of the elastic system, the latter given as

$$q_n = \frac{16k\bar{l}^3}{27(2n-1)^2\pi^2 B}, \qquad n \in \mathbb{N}^+, \tag{4.7}$$

and the former is the 'n-th' and critical 'cr' value of the dimensionless load

$$p = \frac{P}{k\bar{l}}. \tag{4.8}$$

Note that the dimensionless relative stiffness is positive, $q_n > 0$, defined in a way that for $n = 1$ there is no buckling for $q_1 < 1$, and that the dimensionless n-th critical load $p_{cr,n}$ has to satisfy the following inequality[3]

$$p_{cr,n} \le 1, \qquad n \in \mathbb{N}^+, \tag{4.9}$$

corresponding to $l(P) \ge 0$, in other words, to the constraint that the blade cannot buckle after complete penetration into the sliding sleeve.

The solution of the cubic equation (4.6) yields the following conclusions:

i) since all the coefficients of the cubic equation (4.6) are real, the following infinite sequence always exists of real roots

$$p_{cr,n}^{\mathcal{C}} = \frac{1}{3}\left[2 + \sqrt[3]{\frac{q_n}{2 - q_n + 2\sqrt{1 - q_n}}} + \sqrt[3]{\frac{2 - q_n + 2\sqrt{1 - q_n}}{q_n}}\right] > 1,$$
$$n \in \mathbb{N}^+, \tag{4.10}$$

all violating the constraint (4.9) and thus representing meaningless solutions from mechanical point of view;

ii) in the case when for a given $m \in \mathbb{N}^+$ the inequality

$$q_{m+1} < 1 < q_m, \qquad \text{or equivalently} \qquad (2m-1)^2 < q_1 < (2m+1)^2, \tag{4.11}$$

---

[3]This restriction holds only for the calculation of the critical loads. Indeed, as it will be shown in Sect. 4.2, equilibrium configurations with $p \ge 1$ are possible for non-trivial deformation paths.

is satisfied, in addition to the sequence of real roots (4.10) other $2m$ real roots exist for the cubic equation (4.6),

$$
\left.\begin{array}{c} p_{cr,n}^{\mathcal{A}} \\[2mm] p_{cr,n}^{\mathcal{B}} \end{array}\right\} = \frac{1}{3}\left[2 - \frac{1 \pm i\sqrt{3}}{2}\sqrt[3]{\frac{q_n}{2 - q_n + 2\sqrt{1 - q_n}}} - \frac{1 \mp i\sqrt{3}}{2}\sqrt[3]{\frac{2 - q_n + 2\sqrt{1 - q_n}}{q_n}}\right], n \le m \qquad n, m \in \mathbb{N}^{+},
$$

(4.12)

satisfying the following property

$$
0 < p_{cr,n}^{\mathcal{A}} \le p_{cr,m}^{\mathcal{A}} \le p_{cr,m}^{\mathcal{B}} \le p_{cr,n}^{\mathcal{B}} < 1, \qquad n \le m \qquad n, m \in \mathbb{N}^{+} \quad (4.13)
$$

so that $2m$ critical loads are obtained, which correspond to 2 critical loads for the same n-th instability mode;

iii) in the particular case when, for a given $m \in \mathbb{N}^{+}$, $q_m = 1$ (or, equivalently, $q_1 = [2m - 1]^2$), the two real roots associated to the m-th mode (4.12) are coincident,

$$
p_{cr,m}^{\mathcal{A}} = p_{cr,m}^{\mathcal{B}} = \frac{1}{3}, \qquad m \in \mathbb{N}^{+}, \quad (4.14)
$$

so that $2m - 1$ critical loads are obtained, though $2m$ postcritical paths still exist.

Dimensionless critical loads, calculated with eq. (4.12), are reported as functions of the dimensionless relative stiffness parameter q_1 in Fig. 4.7 for the first three modes ($n = 1, 2, 3$), together with the experimental data observed on Prototype 1. As it will be shown in the following, the dimensionless load $p_{cr,1}^{\mathcal{A}}$ corresponds to the lower buckling load and to the loss of stability of the straight configuration, while the dimensionless load $p_{cr,1}^{\mathcal{B}}$ corresponds to the upper bifurcation load and to the restabilization of the straight configuration. Note that there is no bifurcation for $q_1 < 1$ (Fig. 4.3, upper part), but for $q_1 > 1$ there are always two bifurcation loads (the lower called 'buckling' and the higher 'restabilization') associated to the first mode (n=1). A second bifurcation mode emerges at $q_1 = 9$, so that four critical loads exists for $9 < q_1 < 25$, two associated with the first mode and two with the second. A third bifurcation mode emerges at $q_1 = 25$. Moreover, while $p_{cr,1}^{\mathcal{A}}$ corresponds to a critical *buckling* load for which there is a spontaneous departure from the straight configuration of the blade, $p_{cr,1}^{\mathcal{B}}$ denotes a load from which the straight configuration returns to be stable, but cannot be spontaneously reached by the blade from its buckled configuration. Finally, we may observe the following.

i) Considering constant geometrical and material properties of the rod, the
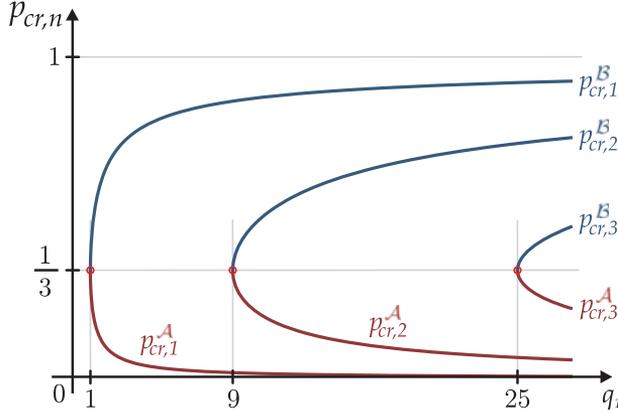
Figure 4.7: Dimensionless bifurcation loads $p_{cr,n}$ (*buckling* load $p_{cr,n}^{\mathcal{A}}$ and *restabilization* load $p_{cr,n}^{\mathcal{B}}$) as a function of the dimensionless relative stiffness q_1 of the elastic system. Note that if the stiffness ratio q_1 decreases, then the n-th buckling load increases while the n-th restabilization load decreases, and the number of bifurcation modes can even reduce to zero in the case of 'highly compliant systems' ($q_1 < 1$), where bifurcation does not occur. Experimental data (white dots) observed on Prototype 1 are also reported.

reduction of spring stiffness k leads to an increase of the *buckling* load $p_{cr,1}^{\mathcal{A}}$ (according to Tarnai, 1980) and a reduction of the *restabilization* load $p_{cr,1}^{\mathcal{B}}$;

ii) differently from the usual behaviour of continuous elastic systems, the structure sketched in Fig. 4.1 has a countable (finite) number (which depends on the elastic properties of the system) of pairs (two for each mode) of critical loads.

4.2 From the total potential energy to the equilibrium equations

An inextensible elastic planar rod (straight in its unloaded configuration, with bending stiffness B and total length $\bar{l}$) has one end constrained with a sliding sleeve and a coaxial spring of stiffness k, while at the other edge is subject to an axial (dead compressive) force P, see Fig. 4.1. Introducing the curvilinear coordinate $s \in [0, \bar{l}]$ and the rotation field $\theta(s)$ of the planar rod's axis, the axial

and transversal displacement fields can be written as

$$u_1(s) = \int \cos\theta(s)ds, \qquad u_2(s) = \int \sin\theta(s)ds. \tag{4.15}$$

With reference to the structural system reported in Fig. 4.1, the sliding sleeve introduces the condition of null rotation for a portion of the rod,

$$\theta(s) = 0, \qquad s \in [0, l_{in}], \tag{4.16}$$

where l_{in} is the length of the rod inside the (frictionless, perfectly smooth and bilateral) sliding sleeve, while on the other end of the rod $(s = \bar{l})$ the boundary condition is

$$\theta'\left(\bar{l}\right) = 0. \tag{4.17}$$

The total potential energy is

$$\mathcal{V}(\theta, l_{in}) = \int_{l_{in}}^{\bar{l}} B \frac{\left[\theta'(s)\right]^2}{2} ds + \frac{1}{2} k \left(l_{in}\right)^2 - P \left[\bar{l} - \int_{l_{in}}^{\bar{l}} \cos\theta(s)ds\right]. \tag{4.18}$$

Since the total potential energy (4.18) is written for a system with a moving boundary l_{in}, it is expedient (Courant and Hilbert, 1953, see also Majidi et al. 2012) to introduce a small parameter ϵ and to take variations (subscript '*var*') of an equilibrium configuration (subscript '*eq*') in the form

$$\theta(s, \epsilon) = \theta_{eq}(s) + \epsilon\theta_{var}(s), \qquad l_{in}(\epsilon) = l_{eq} + \epsilon l_{var}, \tag{4.19}$$

with the boundary conditions at the sliding sleeve $(s = l_{in})$

$$\theta_{eq}(l_{eq}) = 0, \qquad \theta(l_{eq} + \epsilon l_{var}) = 0, \tag{4.20}$$

and the boundary conditions at the other end $(s = \bar{l})$

$$\theta'_{eq}\left(\bar{l}\right) = 0, \qquad \theta'_{var}\left(\bar{l}\right) = 0. \tag{4.21}$$

A Taylor series expansion of $\theta(l_{in})$ for small ϵ yields

$$\theta(l_{eq} + \epsilon l_{var}, \epsilon) = \theta_{eq}(l_{eq}) + \epsilon\left[\theta_{var}(l_{eq}) + \theta'_{eq}(l_{eq})l_{var}\right]$$
$$+ \frac{\epsilon^2}{2}l_{var}\left[2\theta'_{var}(l_{eq}) + \theta''_{eq}(l_{eq})l_{var}\right] + \mathcal{O}\left(\epsilon^3\right), \tag{4.22}$$

so that the boundary conditions (4.20) lead to the following compatibility equa-

tions

$$\theta_{var}(l_{eq}) + \theta'_{eq}(l_{eq})l_{var} = 0, \quad 2\theta'_{var}(l_{eq}) + \theta''_{eq}(l_{eq})l_{var} = 0. \tag{4.23}$$

Taking into account the Leibniz rule of differentiation and the boundary conditions (4.20) and (4.21), together with compatibility equations (4.23), through integration by parts, the first variation of the functional $\mathcal{V}$ is obtained as

$$\delta_\epsilon \mathcal{V} = -\int\limits_{l_{eq}}^{\bar{l}} \left[B\theta''_{eq} + P\sin\theta_{eq}(s)\right]\theta_{var}(s)ds + \left[kl_{eq} - P + \frac{B}{2}\theta'_{eq}(l_{eq})^2\right]l_{var},$$

$$\tag{4.24}$$

from which, by imposing vanishing for any admissible variation $\theta_{var}(s)$ and l_{var}, the elastica is obtained

$$B\theta''_{eq}(s) + P\sin\theta_{eq}(s) = 0, \tag{4.25}$$

as well as the axial equilibrium condition

$$P = kl_{eq} + \underbrace{\frac{B}{2}\left[\theta'_{eq}(l_{eq})\right]^2}_{Eshelby-likeForce}, \tag{4.26}$$

revealing the presence of an Eshelby-like force (Bigoni et al., 2013) generated by the sliding sleeve (see also the asymptotic derivation by Balabukh et al., 1970) and representing the so-called 'transversality condition' of Courant and Hilbert (1953). Note that, eq. (4.26) reduces to the 'trivial' axial equilibrium equation, eq (4.4), only in the case of null curvature at the sliding sleeve, $\theta'_{eq}(l_{eq}) = 0$.

It can be noted from the axial equilibrium equation (4.26) that, the surprising (and never noticed before) equilibrium configuration shown in Fig. 4.6 is possible in the absence of the spring ($k = 0$), when the elastica is such that the curvature at the sliding sleeve satisfies

$$P = \frac{B}{2}\left[\theta'_{eq}(l_{eq})\right]^2, \tag{4.27}$$

corresponding to the fact the dead load P and the Eshelby-like force $(B\left[\theta'_{eq}(l_{eq})\right]^2/2)$ are equal and opposite.

4.2.1 The elastica

The rotation field at equilibrium $\theta_{eq}(s)$ is the solution of the following non-linear second–order differential equation with moving boundary condition

$$\begin{cases} \dfrac{d^2\theta_{eq}(s)}{ds^2} + \lambda^2 \sin\theta_{eq}(s) = 0, & s \in \left(l_{eq}, \bar{l}\right) \\[2mm] \theta_{eq}\left(l_{eq}\right) = 0, \\[2mm] \left.\dfrac{d\theta_{eq}(s)}{ds}\right|_{s=\bar{l}} = 0, \\[2mm] \lambda^2 = \dfrac{k}{B}l_{eq} + \dfrac{1}{2}\left[\theta'_{eq}(l_{eq})\right]^2, \end{cases} \tag{4.28}$$

where the normalized axial load $\lambda^2 = P/B$ has been introduced.

The problem has the trivial solution (denoted with $^{(0)}$)

$$\theta_{eq}^{(0)}(s) = 0, \qquad l_{eq}^{(0)} = \frac{P}{k}, \tag{4.29}$$

while non-trivial solutions can be obtained through the following procedure. Multiplication of equation $(4.28)_1$ by $d\theta_{eq}/ds$ and integration in the variable s yields

$$\left[\frac{d\theta_{eq}(s)}{ds}\right]^2 - 2\lambda^2 \cos\theta_{eq}(s) = \text{constant}, \tag{4.30}$$

so that, setting $\theta_{eq}(\bar{l}) = \theta_{\bar{l}}$ and using the boundary condition $(4.28)_3$, it follows (only the solution with the '+' sign has been considered)

$$\frac{d\theta_{eq}(s)}{ds} = \lambda\sqrt{2(\cos\theta_{eq}(s) - \cos\theta_{\bar{l}})}. \tag{4.31}$$

It is now a standard expedient to operate the following change of variables

$$\eta = \sin\frac{\theta_{\bar{l}}}{2}, \qquad \eta\sin\phi(s) = \sin\frac{\theta_{eq}(s)}{2}, \tag{4.32}$$

leading to the following differential problem equivalent to the system (4.28)

$$
\begin{cases}
\dfrac{d\phi(s)}{ds} = \lambda\sqrt{1 - \eta^2 \sin^2 \phi(s)}, \\[3mm]
\phi\left(l_{eq}\right) = h\pi, \\[3mm]
\phi(\bar{l}) = \dfrac{2j+1}{2}\pi, \\[3mm]
l_{eq} = \lambda^2 \dfrac{B}{k}(1 - 2\eta^2).
\end{cases}
\qquad h, j \in \mathbb{Z} \qquad (4.33)
$$

Integration of the differential problem (4.33) leads to non-trivial η, related to the rotation of the loaded end $\theta_{\bar{l}}$ through eq. (4.32), as a function of the load parameter λ,

$$
(2n-1)\mathcal{K}(\eta) = \lambda\left[\bar{l} - \lambda^2\frac{B}{k}(1 - 2\eta^2)\right], \qquad n \in \mathbb{N}^+, \qquad (4.34)
$$

where n corresponds to the number of the instability mode and $\mathcal{K}(\eta)$ is the complete elliptic integral of the first kind,

$$
\mathcal{K}(\eta) = \int\limits_0^{\frac{\pi}{2}} \frac{d\phi}{\sqrt{1 - \eta^2 \sin^2 \phi}}. \qquad (4.35)
$$

Using the dimensionless parameters p_n and q_n, eqs. (4.7) and (4.8), the solution (4.34) can be rewritten in the following form

$$
(1 - 2\eta^2)^2 p_n^3 - 2(1 - 2\eta^2)p_n^2 + p_n - \frac{4}{27q_n}\left[\frac{2\mathcal{K}(\eta)}{\pi}\right]^2 = 0, \qquad n \in \mathbb{N}^+, \quad (4.36)
$$

which is a cubic equation providing in general three 'deformation paths' $(\mathcal{A}_n; \mathcal{B}_n; \mathcal{C}_n)$ corresponding to the n-th mode, namely, three dimensionless loads $(p_n^{\mathcal{A}}; p_n^{\mathcal{B}}; p_n^{\mathcal{C}})$ for each mode as functions of the rotation at the loaded end $\theta_{\bar{l}}$, through inversion of relation (4.32)$_1$, and the relative dimensionless stiffness q_n

$$
p_n^{\mathcal{A}} = p_n^{\mathcal{A}}(\theta_{\bar{l}}, q_n), \qquad p_n^{\mathcal{B}} = p_n^{\mathcal{B}}(\theta_{\bar{l}}, q_n), \qquad p_n^{\mathcal{C}} = p_n^{\mathcal{C}}(\theta_{\bar{l}}, q_n), \qquad n \in \mathbb{N}^+. \quad (4.37)
$$

Note that in the limit of undeformed configuration (implying a null angle at the loaded end $\theta_{\bar{l}} \to 0$, so that $\eta \to 0$, $\mathcal{K}(\eta \to 0) \to \pi/2$), the cubic equation (4.36)

corresponds to that obtained within the small displacement theory, eq. (4.6), and again yields the critical dimensionless loads $(p_{cr,n}^{\mathcal{A}}; p_{cr,n}^{\mathcal{B}}; p_{cr,n}^{\mathcal{C}})$, given by eqs. (4.10) and (4.12).

For a given value of the applied load, the rotation at the loaded end (related to the three 'deformation paths') can be computed from eq. (4.36) and then, through inversion of relation $(4.32)_1$, the corresponding rotation field can be obtained

$$\theta_{eq}(s) = 2 \arcsin \left[\eta \operatorname{sn} \left(\lambda \left(s - l_{eq} \right), \eta \right) \right], \tag{4.38}$$

from which the axial and transversal displacements are obtained by integration, eq. (4.15), as

$$
\begin{aligned}
u_1(s) &= -s + \frac{2}{\lambda} E \left[\operatorname{am} \left(\lambda \left(s - l_{eq} \right), \eta \right), \eta \right] - l_{eq}, \\
u_2(s) &= \frac{2\eta}{\lambda} \left[1 - \operatorname{cn} \left(\lambda \left(s - l_{eq} \right), \eta \right) \right],
\end{aligned}
\tag{4.39}
$$

which can be evaluated at the loaded end, thus yielding

$$u_1 \left(\bar{l} \right) = \frac{2}{\lambda} \left[E \left(\eta \right) - \mathcal{K} \left(\eta \right) \right] - l_{eq}, \qquad u_2(\bar{l}) = \frac{2\eta}{\lambda}. \tag{4.40}$$

In eq. (6.1) the functions am, cn and sn denote the Jacobi amplitude, Jacobi cosine amplitude and Jacobi sine amplitude functions,

$$\operatorname{cn}(x, \eta) = \cos \left[\operatorname{am}(x, \eta) \right], \qquad \operatorname{sn}(x, \eta) = \sin \left[\operatorname{am}(x, \eta) \right], \tag{4.41}$$

while $E(x, \eta)$ is the incomplete elliptic integral of the second kind of modulus η, defined as

$$E(x, \eta) = \int_o^x \sqrt{1 - \eta^2 \sin^2 t} \, dt. \tag{4.42}$$

Finally, in the case when the stiffness of the axial spring vanishes ($k = 0$, Fig. 4.6), eq. (4.27) represents the only possible equilibrium configuration of the system. This equation can be rewritten, by introducing a change of variables in eq. (4.32), as

$$1 - 2 \sin^2 \left(\frac{\theta_{\bar{l}}}{2} \right) = 0. \tag{4.43}$$

Eq. (4.43) reveals that the only equilibrium configuration for the system without spring occurs when the end tangent to the rod is orthogonal to the sliding sleeve, $\theta_{\bar{l}} = \pi/2$, representing *a purely geometrical condition*, visibly satisfied in Fig. 4.6.

4.3 Stability of configurations

In order to evaluate the stability of the equilibrium configurations for the penetrating blade, the second variation of the functional $\mathcal{V}$, eq. (4.18), has to be calculated. Considering the boundary conditions (4.20) and the perturbations in the rotation field $\theta_{var}(s)$ and in the length l_{var} satisfying the compatibility equations (4.23), the second variation evaluated at an inflexed equilibrium configuration can be written as

$$\delta_\epsilon^2 \mathcal{V} = \frac{1}{2}\left\{ kl_{var}^2 + B \int_{l_{eq}}^{\bar{l}} \left[\theta_{var}'(s)\right]^2 ds - P \int_{l_{eq}}^{\bar{l}} [\theta_{var}(s)]^2 \cos\theta_{eq}(s) ds \right\}. \quad (4.44)$$

The stability or instability of an equilibrium configuration is then related to the sign of the second variation $\delta_\epsilon^2 \mathcal{V}$, evaluated for that equilibrium configuration, namely,

$$\delta_\epsilon^2 \mathcal{V} = \begin{cases} > 0 & \text{stable equilibrium configuration,} \\[2mm] < 0 & \text{unstable equilibrium configuration,} \end{cases} \quad (4.45)$$

for any admissible perturbations $\theta_{var}(s)$ and l_{var} satisfying the compatibility eqs. (4.23).

Considering the auxiliary function $\Gamma(s)$, solution of the following boundary value problem (the Riccati equation plus a boundary condition, see van Brunt, 2005)

$$\begin{cases} \dfrac{\partial \Gamma(s)}{\partial s} - P\cos\theta_{eq}(s) - \dfrac{\Gamma(s)^2}{B} = 0, \\[4mm] \Gamma(\bar{l}) = 0, \end{cases} \quad (4.46)$$

the compatibility eqs. (4.23) and the following identity

$$\int_{l_{eq}}^{\bar{l}} \frac{d}{ds}\left[\theta_{var}^2(s)\Gamma(s)\right] ds - \left[\theta_{var}^2(s)\Gamma(s)\right]_{l_{eq}}^{\bar{l}} = 0, \quad (4.47)$$

the second variation, eq. (4.44), can be rewritten as

$$\delta_\epsilon^2 \mathcal{V} = \frac{1}{2}\left\{ B \int_{l_{eq}}^{\bar{l}} \left[\theta_{var}'(s) + \frac{\Gamma(s)}{B}\theta_{var}(s)\right]^2 ds + l_{var}^2 \left[\left[\theta_{eq}'(l_{eq})\right]^2 \Gamma(l_{eq}) + k\right] \right\}. \quad (4.48)$$

To judge the stability of the equilibrium configurations, the two conditions obtained by Majidi et al. (2012) are exploited here. In particular (note that the existence of a bounded $\Gamma(s)$ on the interval $\left[l_{eq}, \bar{l}\right]$ implies that the integral in (4.48) is non-negative)

- *Necessary condition* (N) for the equilibrium configuration defined by $\{\theta_{eq}(s), l_{eq}\}$ to be stable (so that it minimizes the functional $\mathcal{V}$) is that the auxiliary function $\Gamma(s)$, solution of to the boundary-value problem (4.46), cannot become unbounded in the interval $\left[l_{eq}, \bar{l}\,\right]$ and satisfies the following inequality

$$\Delta = \left[\theta_{eq}^{'}(l_{eq})\right]^{2} \Gamma(l_{eq}) + k \geq 0. \tag{4.49}$$

- *Sufficient condition* (S) for the trivial equilibrium configuration $\{\theta_{eq}(s) = 0, l_{eq} = P/k\}$, to be stable is that the auxiliary function $\Gamma(s)$, solution of the boundary-value problem (4.46), is bounded.

In order to obtain the auxiliary function $\Gamma(s)$, it is instrumental to consider the Jacobi transformation

$$\Gamma(s) = -B\frac{\Lambda^{'}(s)}{\Lambda(s)}, \tag{4.50}$$

leading to the following Jacobi boundary value problem

$$\begin{cases} \Lambda^{''}(s) + \lambda^{2}\cos\theta_{eq}(s)\,\Lambda(s) = 0, \\ \Lambda(\bar{l}) = 1, \\ \Lambda^{'}(\bar{l}) = 0. \end{cases} \tag{4.51}$$

Once the function $\Gamma(s)$ and the auxiliary function $\Lambda(s)$ are obtained for a specific equilibrium configuration by solving the differential eqs. (4.46) and (4.51), the stability of that equilibrium configuration can be judged through the necessary (N) and sufficient (S) conditions.

4.3.1 Stability of trivial configurations

In the case when the equilibrium configuration is straight, identifying the trivial solution $\{\theta_{eq}(s) = 0; \;\; l_{eq} = P/k\}$, the Jacobi boundary value problem (4.51) simplifies to

$$\begin{cases} \Lambda^{''}(s) + \lambda^{2}\,\Lambda(s) = 0, \\ \Lambda(\bar{l}) = 1, \\ \Lambda^{'}(\bar{l}) = 0, \end{cases} \tag{4.52}$$

which, through the Jacobi transformation (4.50), leads to the following solution for the auxiliary function $\Gamma(s)$

$$\Gamma(s) = \sqrt{PB} \tan\left(\sqrt{\frac{P}{B}}\,(\bar{l} - s)\right).\tag{4.53}$$

The auxiliary function $\Gamma(s)$, eq. (4.53), is bounded for $s \in \left[l_{eq} = P/k, \bar{l}\,\right]$ if and only if

$$\frac{P}{B}\left(\bar{l} - \frac{P}{k}\right)^2 < \frac{\pi^2}{4},\tag{4.54}$$

which can be rewritten in the dimensionless form

$$p\,(1-p)^2 < \frac{4}{27q_1},\tag{4.55}$$

an equation reducing to eq. (4.6) when '<' is replaced by '='. Considering now the necessary (N) and sufficient (S) conditions, the *trivial straight configuration is*:

- for $q_1 < 1$: *stable* ('highly compliant' systems, see eq. (4.7));

- for $q_1 > 1$:

    - *stable*   if $P < P_{cr,1}^{\mathcal{A}}$,
    - *unstable* if $P_{cr,1}^{\mathcal{A}} < P < P_{cr,1}^{\mathcal{B}}$,
    - *stable*   if $P_{cr,1}^{\mathcal{B}} < P < k\bar{l}$.

4.3.2   Stability of non-trivial configurations

In the case of non-trivial equilibrium configurations, $\theta_{eq}(s) \neq 0$, the function $\Lambda(s)$, solution of the Jacobi problem (4.52), can be obtained only through numerical integration. Numerical investigations performed varying the dimensionless relative stiffness q_1 and the applied load P show which non-trivial configuration is unstable, through application of the necessary condition (N). In particular, a configuration is unstable either (N$_1$) when the function $\Lambda(\hat{s}) = 0$ with $\hat{s} \in \left[l_{eq}, \bar{l}\,\right)$, namely, the auxiliary function $\Gamma(s)$, is bounded, or (N$_2$) when $\Delta < 0$, see eq. (4.49).

It is concluded that *unstable equilibrium configurations* are:

- all the investigated non-trivial equilibrium configurations of the paths $\mathcal{A}_n$, $\mathcal{B}_n$, and $\mathcal{C}_n$ with $n \geq 2$, due to condition (N$_1$);

- all the non-trivial equilibrium configurations of the path $\mathcal{B}_1$, due to condition (N$_2$);

- all the non-trivial equilibrium configurations of the path $\mathcal{A}_1$, due to condition (N$_2$), when $q_1 < 1$;

- the non-trivial equilibrium configurations associated to a negative slope in the $\theta_{\bar{l}} - P$ plane (snap-through instability) of the path $\mathcal{A}_1$, due to condition (N$_2$), and occurring only when $1 < q_1 < q^{ST} \approx 1.6875$.

All other non-trivial equilibrium configurations not listed above satisfy the necessary condition (N) and therefore *could* be stable, although this cannot be proven and remains an open problem. However, although stability for these cases cannot –for the moment– be rigorously decided, the stability of the non-trivial equilibrium configurations $\mathcal{A}_1$ has been experimentally confirmed (see the experimental results presented in the next Section).

Finally, it is straightforward to judge the stability of the system in the case when the axial spring is absent ($k = 0$, Fig. 4.6) and conclude that, although the auxiliary function $\Gamma(s)$ is always bounded, all the possible equilibrium configurations are unstable due to condition (N$_2$).

4.4 Theory vs. experiments

The buckling loads of the structure sketched in Fig. 4.1 are given by Eq. (4.12). Moreover, for a given value of the applied load P, λ is known from its definition ($\lambda^2 = P/B$), so that Eq. (4.34) allows the calculation of the corresponding η and thus l_{eq} is known from Eq. (4.33)$_4$. Finally, Eqs. (6.1) give the components of the elastica and, in particular, Eqs. (4.40) permit the evaluation of the displacement components of the blade's end point. Instability (stability) of the configurations has been determined using condition N (condition S) obtained in Sect. 4.3. As we have already mentioned in that Section, the stability of the ascending branches of the first-mode of postcritical behaviour (where the necessary condition for stability is verified) has been *only conjectured* on the basis of our experimental results, while stability and instability of all the rest of the trivial and bifurcated paths has been rigorously proven.

Restricting the attention for the moment only to the first bifurcation mode of the structure shown in Fig. 4.1, the dimensionless load $p = P/(k\bar{l})$ is plotted as a function of the dimensionless displacement components $\{u_1(\bar{l})/\bar{l}, u_2(\bar{l})/\bar{l}, \theta_{\bar{l}}\}$ in Fig. 4.8, for different values of the dimensionless stiffness q_1, taken equal to 0.7, 1.1, and 2. Note that solid (dashed) lines represent stable (unstable) configurations.

The following observations can be drawn.

- The upper part of Fig. 4.8 is relative to $q_1 = 0.7$. In this case, no bifurcation occurs and the blade rigidly penetrates into the sliding sleeve. Note that alternative (and unstable) equilibrium configurations exist in addition
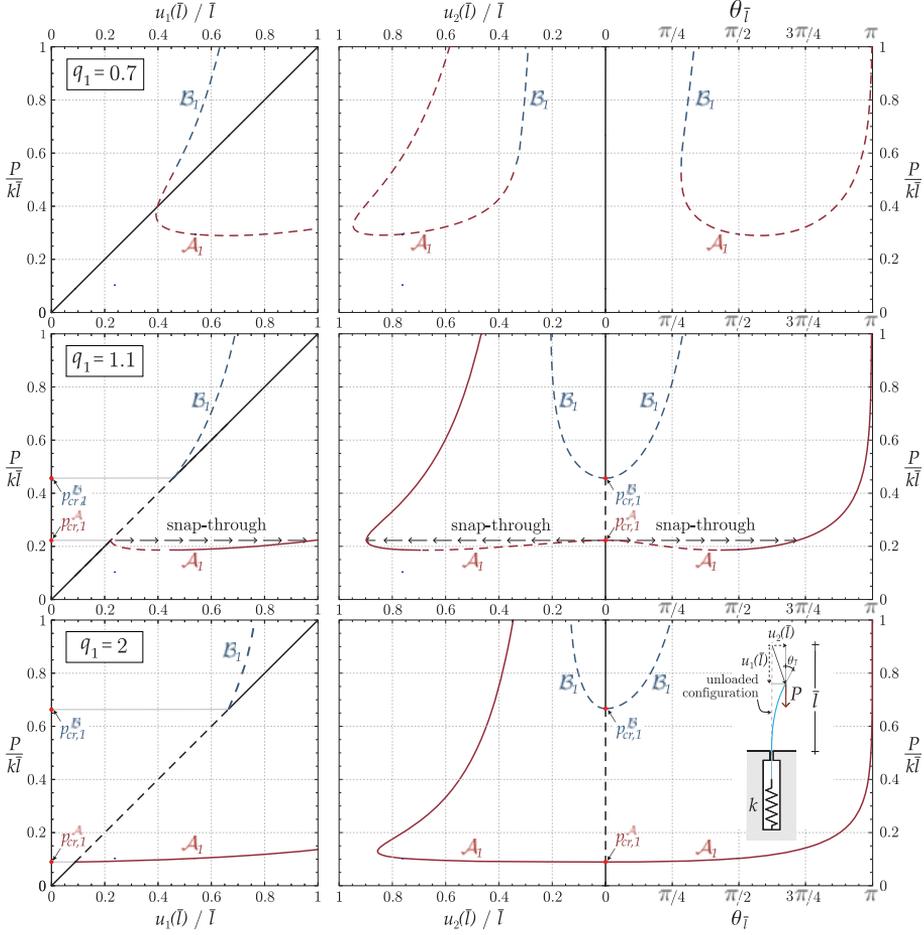
Figure 4.8: First-mode of bifurcation: deformation paths of the structure sketched in the inset, expressed as the (dimensionless) applied load versus (dimensionless) displacement components and rotation of the blade loaded edge.

to the trivial straight configuration, but (with the exception of the figure on the left, which can give a false impression of bifurcation) they do not cross (and even 'touch') the trivial path, so that these non-trivial unstable configurations cannot spontaneously be reached by the system.

- Both the central and the lower parts of Fig. 4.8 show *two bifurcation loads*

associated to the first bifurcation mode and show the *restabilization of the straight configuration* after the second buckling load.

- The central part of Fig. 4.8, referred to $q_1 = 1.1$, shows an example of a descending path of the lower equilibrium branch, associated to a snap-through of the system. On the other hand, the lower part of Fig. 4.8, referred to $q_1 = 2$, shows that the lower equilibrium branch has always a positive slope (so that snap-through does not occur).

- Comparing the central and the lower parts of Fig. 4.8 we may observe that *an increase in the stiffness of the system decreases the buckling load and increases the restabilization load.*

- The fact that a vertical *Eshelby-like force is generated and 'expels' the blade from the sliding sleeve after buckling* is not directly visible in Fig. 4.8. The visualization of this effect requires plotting P as a function of l_{eq}, which is done in Fig. 4.10 where comparison with experiments is presented.

An example of bifurcation paths involving the first, the second and the third mode is reported in Fig. 4.9, where the load P (made dimensionless through division by $k\bar{l}$) is plotted as a function of the rotation of the loaded end of the blade, $\theta_{\bar{l}}$. In the three parts of Fig. 4.9, referring (from left to right) to q_1
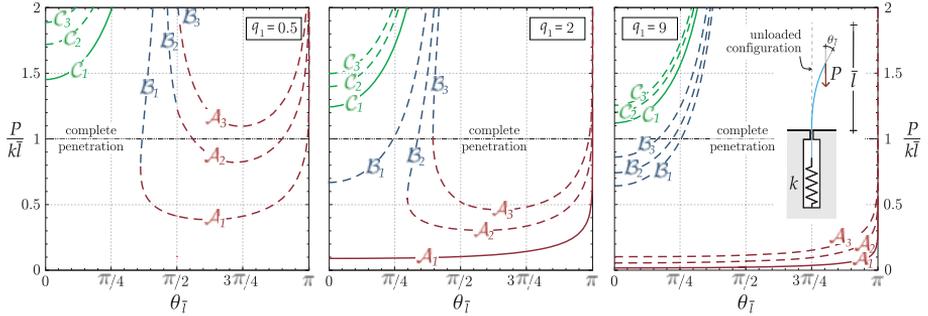
Figure 4.9: Force vs. blade's edge rotation of the structure sketched in the inset, evidencing the first, second and third mode of bifurcation. The threshold marked as 'complete penetration' corresponds to the complete penetration of the blade into the sliding sleeve. In the example on the left there is no bifurcation, while in the central part of the figure only the first mode is involved. In the right part of the figure, the first, second and third mode of bifurcation may occur before the 'complete penetration' is attained.

equal to 0.5, 2, and 9, a line denoted as 'complete penetration' is reported at the value of parameter $p = P/(k\bar{l}) = 1$, corresponding to the complete penetration

of the blade into the sliding sleeve. Therefore, curves reported beyond that limit are mathematically corrected, but meaningless from mechanical point of view. A situation where the postcritical paths do not intersect the vertical axis (corresponding to stable equilibrium only for the trivial straight configuration), and thus bifurcation does not occur, is reported in the left part of the figure, $q_1 = 0.5$. Here, first- and second-mode non-trivial unstable configurations exist below the 'complete penetration' limit but these cannot be reached during loading of the system. Bifurcation is possible in the central, $q_1 = 2$, and right, $q_1 = 9$, parts of the figure. While only first mode bifurcations occur in the former case, in the latter case first, second and third modes bifurcations are possible. In general, all modes superior to the first have been always found unstable in all cases analyzed (not only in those reported in this article).

An essential part in the present study is to show that all the found mechanical behaviours can be realized in practice. To this purpose, we have designed, realized and tested model structures to verify the theoretical findings. We have already anticipated with Figs. 4.3–4.6 that the theory has been fully confirmed, so that our intention is now to provide quantitative support.

Two prototypes (called 'Prototype 0', see Appendix A and Fig. 4.11, and 'Prototype 1', Fig. 4.2, right) of the structure sketched in Fig. 4.1 have been realized, according to the design scheme shown in Fig. 4.2 (left). Both prototypes have fully confirmed the theory, although Prototype 0 only in a qualitative way, so that Prototype 1 has been later manufactured to obtain quantitative results.

The linear elastic spring represented in Fig. 4.1 has been realized by hanging a highly-stiff horizontal bar (to which the elastic blade is clamped) with two metal springs. The horizontal bar can only rigidly translate as constrained by two linear bushings (LHFRD12, Misumi Europe).

Five blades have been employed (lengths: 600 mm, 530 mm, 510 mm, 430 mm, and 360 mm) with the 'stiff' springs and four blades (lengths: 600 mm, 530 mm, 510 mm and 430 mm) with the 'compliant' one, all realized with C62 carbon-steel strips (25 mm × 2 mm cross section) in the experiments. For these blades the bending stiffness B has been determined with flexure experiments to be equal to 2.70 Nm^2. The same sliding sleeve employed by Bigoni et al. (2013) has been used, which is 296 mm in length and has been realized with 27 pairs of rollers (made up of 10 mm diameter and 15 mm length teflon cylinders, each containing two roller bearings). The tolerance between the metal strip and the rollers has been set to be 0.2 mm. Two pairs of carbon steel (EN 10270-1 SH) springs (the so-called 'stiff': D19130, 1.6 mm wire diameter and 12.5 mm mean coil diameter, k=600 N/m; and the so-called 'compliant': D19100 1.25 mm wire diameter and 8 mm mean coil diameter, k=540 N/m, purchased from D.I.M.) have been used. The dead load at the end of the blade has been imposed by filling (at a constant rate of 10 g/s) two containers with water and has been

measured with two miniaturized Leane XFTC301 (R.C. 500N) load cells. The penetration length l_{eq} has been obtained by measuring the displacement of the lower edge of the blade through a magnetic noncontact displacement transducer GC-MK5 (from Gemac).

Experimental results (solid lines) are reported in Fig. 4.10 and compared with theoretical predictions (dashed lines). Results are expressed in terms of applied load P (measured in N) as a function of the amount of blade internal to the sliding sleeve, l_{eq} (measured in cm). Results reported on the left refer to
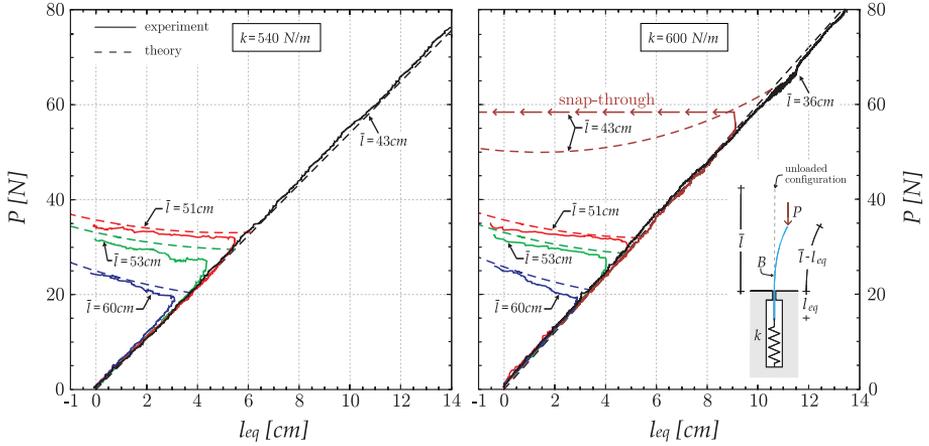
Figure 4.10: Comparison of theoretical and experimental results obtained with the set-up shown in Fig. 4.2.

'compliant' spring, $k = 540 N/m$, while results reported on the right to the 'stiff' one, $k = 600 N/m$. Four blades of different length have been used in the former case, five in the latter. For both spring stiffnesses, the blades with shortest length show a pure translation without buckling, while buckling has been observed for all the other lengths. A snap-through behaviour was theoretically predicted for $\bar{l} = 51$ cm of the 'compliant' spring case and for $\bar{l} = 43$ cm of the 'stiff' spring case. In the former case ($\bar{l} = 51$ cm), the descending postcritical path is so short and weakly inclined that it becomes hardly visible in the graph and therefore the snap-through has not been experimentally observed. On the other hand, in the latter case ($\bar{l} = 43$ cm) the snap-through has been so violent that the experiment has been immediately interrupted and subsequent data have not been measured.

A very nice agreement between theory and experiments (fully confirming the presence of the Eshelby-like force) can be noted from Fig. 4.10, with departures from the straight configuration observed to occur slightly before the theoretical

loads for buckling, which is nothing but the usual effect of the imperfections (see for instance Bigoni et al. 2012). Experiments clearly show that the blade is ejected from the sliding sleeve (which corresponds to a decrease in l_{eq}) during the postcritical behaviour of the structure and that the measured values of the force perfectly agree with those found by Bigoni et al. (2013).

Finally, the theoretical and experimental shapes of the elastica are so tightly close to each other that result superimposed in the the photos shown in Figs. 4.4, 4.5 and 4.6. Therefore, the calculated elastica curves have been omitted from the figures to preserve the view of the experiment.

Movies of the experiments can be found in the additional material at http://ssmg.unitn.it/.

Prototype 0 and further details on the experimental setup

The Prototype 0 (Fig. 4.11) has been realized to provide a qualitative experimental validation of the features displayed by the mechanical system shown in Fig. 4.1.
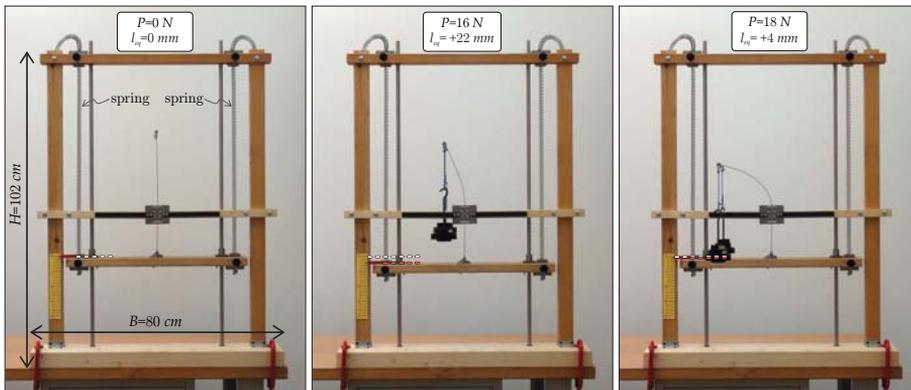
Figure 4.11: The unloaded configuration (left) and two deformed configurations (center and right) of Prototype 0. At high load (right) the base of the structure has an upward rigid translation when compared with the configuration at low load (left), a clear indication of the presence of the Eshelby-like force.

Two blades have been employed (with lengths 250 mm and 200 mm), both realized with a C62 carbon-steel strip (25 mm × 1 mm cross section). The sliding sleeve, 31 mm in length, has been realized with three pairs of rollers (15 mm diameter teflon cylinders, each containing two roller bearings). Three pairs

of carbon steel (EN 10270-1 SH) springs (D19060, 0.8 mm wire diameter and 5 mm mean coil diameter; D19130, 1.6 mm wire diameter and 12.5 mm mean coil diameter; D19100, 1.25 mm wire diameter and 8 mm mean coil diameter all purchased from D.I.M.) have been used. The two linear bushings (LHFRD12) used to maintain horizontal the bar to which the blade is clamped have been purchased from Misumi Europe. Load has been controlled by manually imposing given weights.

For both Prototypes 0 and 1, all the experimental tests have been performed in a controlled temperature (20±0.2°C) and humidity (48±0.5%) room and data have been acquired with a NI CompactDAQ system, interfaced with Labview 8.5.1 (National Instruments). Furthermore, photos have been taken with a Sony NEX 5N digital camera, equipped with 3.5-5.6/18-55 lens (optical steady shot from Sony Corporation) and movies have been recorded during the tests with a Sony handycam (model HDR-XR550VE).

Additional material can be found at http://ssmg.unitn.it/.

5

A teaching model for truss structures

A classroom demonstration model has been designed, machined and successfully tested in different learning environments to facilitate understanding of the mechanics of truss structures, in which struts are subject to purely axial load and deformation. Gaining confidence with these structures is crucial for the development of lattice models, recurring in many fields of physics and engineering.

The way in which a *truss structure* can be conceived to have all elements subject to pure axial force is complex and the way it deforms under loading is definitely not intuitive, even for undergraduate students of mathematics, physics, and engineering. Truss structures are *optimal*, ubiquitous and so important from many perspectives that deserve a special attention. Indeed truss structures are used in many traditional (e.g. bridges, electricity pylons, cranes, airplanes, cars, motorcycles) and innovative (e.g. nanotrusses [60]) technologies and are crucial for the understanding of several biological structures (e.g. vertebrate skeletons [20] and protein materials [12]) and conceptual models in physics (e.g. crystal lattices). Our aim is to develop a teaching model to enhance the student's ability of visualizing the deformation of such lattice structures, which is the primary key to 'catch the concept'[1].

Models of elastic truss structures have been previously developed for both stimulate student's interest and form an experimental outlook during undergraduate teaching [14, 37, 39, 57]. However, the models developed by Pippard [57]

---

[1]Cross and Morgan [16] wrote: 'The ability of a designer of continuous structures is measured chiefly by his ability to visualize the deformation of the structure under load. If he cannot form a rough picture of these deformations when he begins the analysis he will probably analyse the structure in some very awkward and difficult way; if he cannot picture these deformations after he has made the analysis, he doesn't know what he is talking about. The more or less gentle reader may find the constant repetition of this theme monotonous, but it is the deliberate conclusion of the authors that the most important aspect of the subject is the simple picture of structural deformation.' We completely agree with this statement, which becomes even more evident nowadays that numerical simulations often obscure physical intuition.

are simple three-element planar systems, while Hilson [39] provides only qualitative experiments, and Godden [37] focusses on buckling of compressed elements. Moreover, in the models proposed by Charlton [14] the struts are 'Z-shaped' members deforming under flexure (see his figure 17), not directly evidencing elongation or shortening, so that the mechanical behaviour results complex enough that cannot be followed by an untrained audience. Therefore, we have developed spring-strut elements, capable of sustaining large deformation (Fig. 5.1), and connected these elements in various structural forms (Warren truss –an ensemble of bars disposed in an alternately inverted equilateral triangle geometry– is only reported here for brevity) through bolt junctions (Fig. 5.2).

The first prototype (not reported here for brevity) that we have developed was planar and, though light, simple and very accurate in reproducing deformation, was hiding the problem of the necessity of braces to avoid out-of-plane instability. Therefore, we have developed the fully spatial model shown in Fig. 5.2, which can effectively demonstrate the importance of cross bracing, see also the electronic supporting material at http://ssmg.unitn.it/video/truss.mp4. This model is addressed to the simplest geometry, namely a Warren structure often employed in bridges (so that it can be used to explain the mechanics of a truss structure), though it is fully representative of the behaviour of elastic lattice models.

The two teaching models have been regularly employed during ten years of undergraduate classes of strength of materials (at the University of Trento) and have been used for: (i.) two university orientation courses organized by the 'Scuola Normale Superiore' of Pisa, (ii.) public demonstrations (for instance, at the so-called 'researchers' night' 2010 and 2011) and even (iii.) presentations given at elementary school. These models have been proved to exemplify the way a truss structure is designed and deforms and have been used during undergraduate class to experimentally assess the validity of structural modelling via linear elasticity.

5.1 The design and performance of the truss model

We have started designing and realizing a simple pin-jointed[2] Warren planar truss structure (namely, one wall of the structure considered in the following –Fig. 5.2– and not reported here for brevity), in which the straight members have been realized with spring-strut elements. The model has been used: (i.) *qualitatively* to show the 'global' behaviour of the structure and to explain the way in which all elements are primarily subject to axial tension or compression and (ii.) *quantitatively* (during undergraduate class), by calculating the ratio between two or more rod's elongation (or node displacements) and measuring

---

[2]The term 'pin-jointed' means that the connection between elements leaves the relative rotation unconstrained.

this ratio on the model.

Classroom presentations of the model have revealed that, though excellent for the above-listed purposes, it was somehow hidden to the student the out-of-plane instability of the structure and the consequent need of a cross bracing. Therefore, we have designed the spring snubber shown in Fig. 5.1 (where a movable pointer allows the measure of the elongation/shortening of the element) and combined in a sort of 'Warren truss bridge', externally constrained with a hinge and a roller, as shown in Fig. 5.2. The snubbers have been machined from aluminum 2117
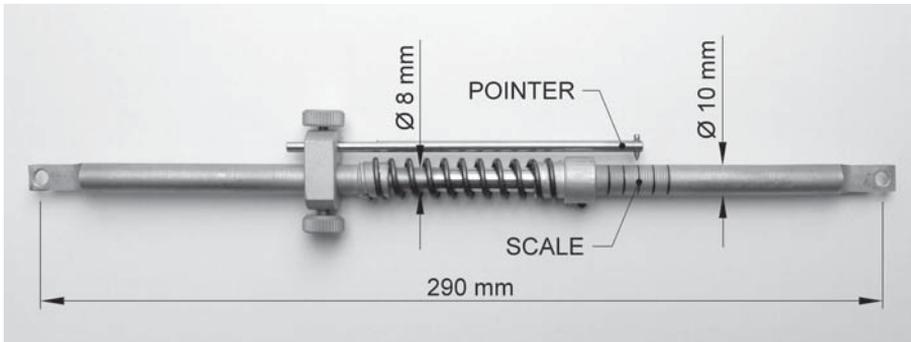
Figure 5.1: The spring snubber element used for the truss structure shown in Fig. 5.2. Note the movable pointer to measure elongation/shortening.

tubes and the springs have been designed using the well-known formula for helical springs of round wire [see eqn (5.3) of [71]] and produced with (2 mm diameter) music wire ASTM A228. The external hinge and roller have been realized with eight roller bearings (SKF-618/5) and the whole structure has been mounted on an AISI 304 stainless steel frame.

During an undergraduate class, the developed models can be used to provide confirmatory experiments. In particular, they can be loaded with dead loads and the elongation or shortening of the bars can be measured on the structure by visual inspection employing the pointers. Two load systems (one symmetric and the other unsymmetric) are shown in Figs. 5.3 and 5.4. In addition to the elongation of the bars, displacement of the nodes can be measured with a mechanical comparator. The measurements of the bar elongations can be normalized through division by one reference elongation and therefore compared with the predicted ratios between the forces inside the bars, which can be calculated on the blackboard and do not require any stiffness measurement. The model allows a nice comparison between theoretical predictions and experimental values, which is crucial to stimulate interest of the students and facilitate understanding
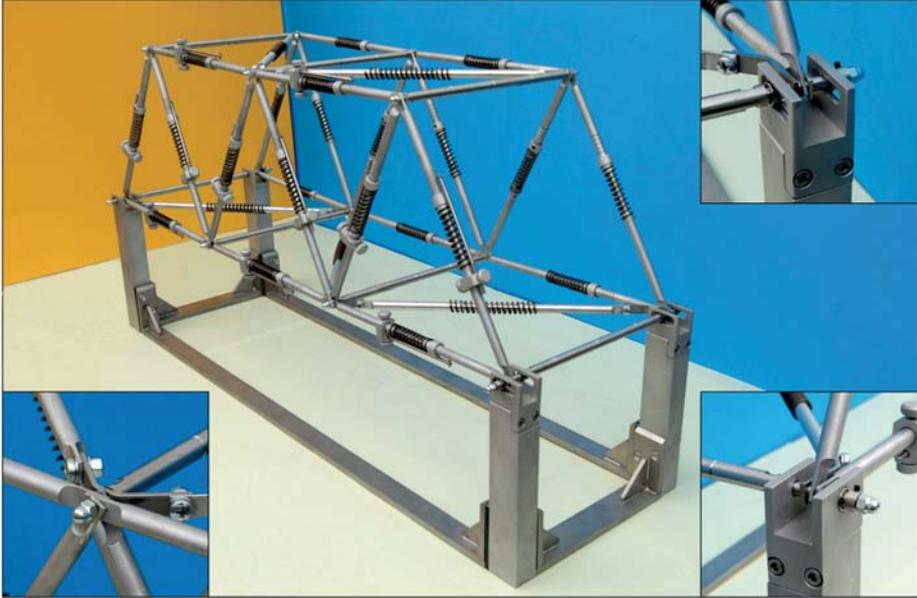
Figure 5.2: View of the (unloaded) spatial Warren truss model, with details (an internal node on the left, two external nodes on the right: a roller and a hinge).

of the capabilities and limits of the mechanical modelling, as highlighted, among others, by Pippard [57].

Measurements of vertical displacements at the central node of the upper chord, labelled 4, and the two central nodes of the lower chord, labelled 3 (left) and 5 (right) for different loadings are reported in Tabs. 5.1 (symmetric loading as in Fig. 5.3) and 5.1 (unsymmetric loading as in Fig. 5.4), as taken by five different students (labelled 'St' in the tables).

Ratios of mean value of the measured (by five students) vertical displacements (presented with the standard deviation as error bar) are compared to the corresponding theoretical values in Fig. 5.5 for symmetric (upper part) and unsymmetric (lower part) loadings. Mean values of the ratios of bars' elongation are reported in Fig. 5.6 for unsymmetric loading.

The experimental values reported in Tabs. 5.1–5.1 and in Figs. 5.5–5.6 show a good agreement with the predictions from linear elastic theory and this agreement becomes tighter at higher loads, where friction at the nodal hinges plays a minor role. Therefore, the developed teaching model does not only provide a qualitative explanation of the mechanics of truss structures, but also a quantita-
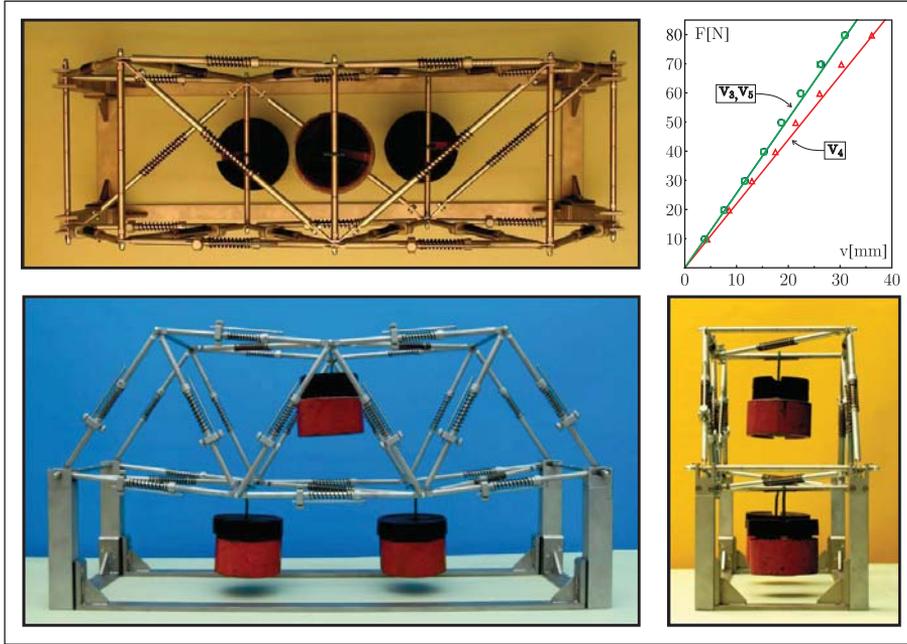
Figure 5.3: Frontal (lower part, on the left), lateral (lower part, on the right) and top (upper part, on the left) view for the symmetric load combination. A comparison between theoretical predictions and experimental data is also included in terms of applied load F versus mean value of measured nodal vertical displacements v (upper part on the right).

tive experimental in-class proof of the validity of the theoretical predictions.

Finally, the truss model can also be effectively employed to explain the importance of cross bracing. Indeed these braces can be easily removed, so that loading of the unbraced model reveals an unstable out-of-plane movement, as illustrated in Fig. 5.7.
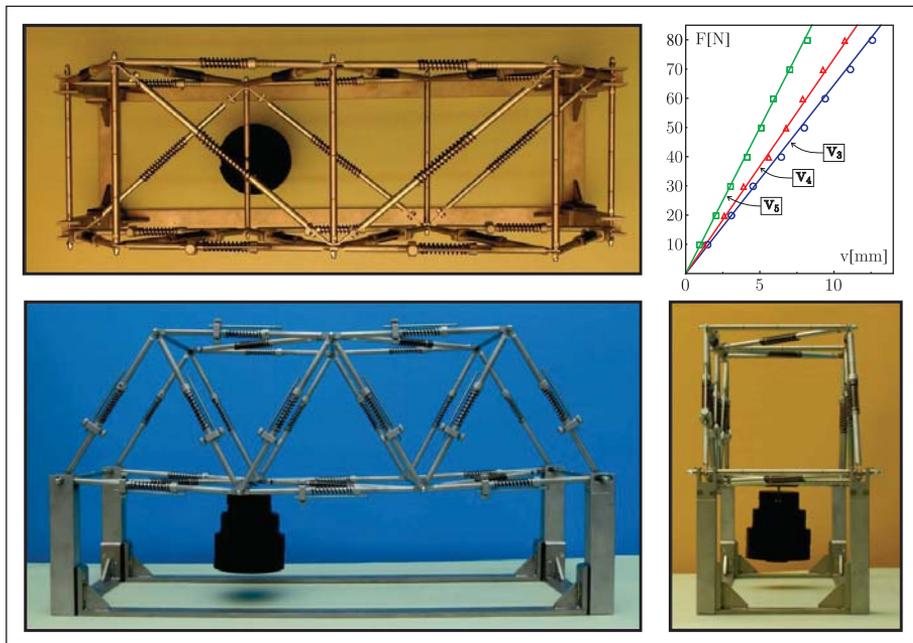
Figure 5.4: As for Fig. 5.3, except that the load is unsymmetric.

Load F[N]	Node	Measured vertical displacement v_i [mm]					Mean value $\bar{v}_i$ [mm]	Standard deviation σ [mm]	Theoretical value v_i [mm]
		St1	St2	St3	St4	St5			
10	3	3.80	4.25	4.35	3.25	3.30	3.79	0.46	3.91
	4	4.30	4.50	4.85	4.25	3.80	4.34	0.34	4.55
	5	3.85	3.90	4.20	3.50	3.75	3.84	0.23	3.91
20	3	8.00	7.85	7.60	7.45	7.35	7.65	0.24	7.82
	4	8.25	8.85	8.25	8.70	8.65	8.54	0.25	9.10
	5	8.00	7.60	7.25	7.65	7.05	7.51	0.33	7.82
30	3	13.10	11.10	11.80	11.45	10.85	11.66	0.79	11.74
	4	14.10	12.75	11.70	13.40	12.85	12.96	0.79	13.65
	5	12.00	11.25	11.30	11.70	11.30	11.51	0.29	11.74
40	3	15.50	14.45	15.95	14.80	15.90	15.32	0.60	15.65
	4	18.10	16.60	16.25	18.35	18.20	17.50	0.89	18.20
	5	15.70	14.40	15.15	15.20	15.80	15.25	0.50	15.65
50	3	19.70	18.00	18.85	17.70	18.80	18.61	0.70	19.56
	4	22.15	20.60	20.15	21.95	22.20	21.41	0.86	22.75
	5	19.45	17.80	18.70	18.20	19.15	18.66	0.60	19.56
60	3	23.30	21.90	23.00	21.90	21.70	22.36	0.66	23.47
	4	26.45	25.20	24.80	26.80	26.90	26.03	0.86	27.30
	5	22.65	21.95	22.80	22.50	22.25	22.43	0.30	23.47
70	3	27.45	25.90	27.25	25.60	25.55	26.35	0.83	27.38
	4	30.80	29.90	29.55	30.10	30.85	30.24	0.51	31.85
	5	26.85	26.00	26.10	25.65	25.90	26.10	0.40	27.38
80	3	30.35	30.60	31.40	31.90	30.45	30.94	0.61	31.29
	4	37.00	35.10	34.85	36.75	36.85	36.11	0.93	36.40
	5	30.75	30.05	31.05	31.60	30.95	30.88	0.50	31.29

Table 5.1: Measures on the teaching model loaded symmetrically (Fig. 5.3) taken by different students

Load F[N]	Node	Measured vertical displacement v_i [mm]					Mean value $\bar{v}_i$ [mm]	Standard deviation σ [mm]	Theoretical value v_i [mm]
		St1	St2	St3	St4	St5			
10	3	1.85	1.50	1.40	1.35	1.30	1.48	0.20	1.55
	4	1.50	1.25	1.05	1.30	1.15	1.25	0.15	1.36
	5	1.20	0.90	0.85	1.05	0.70	0.94	0.17	1.00
20	3	2.95	3.30	2.75	3.65	2.75	3.08	0.35	3.10
	4	2.75	2.35	2.45	2.80	2.65	2.6	0.17	2.72
	5	1.95	1.90	2.15	2.50	1.75	2.05	0.26	2.00
30	3	4.65	4.65	4.60	4.50	4.35	4.55	0.11	4.65
	4	3.85	4.15	3.45	4.30	3.75	3.90	0.30	4.08
	5	3.30	2.75	2.60	3.60	2.85	3.02	0.37	3.01
40	3	6.10	6.40	6.15	7.40	6.20	6.45	0.49	6.20
	4	5.25	5.80	5.55	6.05	5.35	5.60	0.29	5.44
	5	4.25	3.70	3.75	4.95	4.05	4.14	0.45	4.01
50	3	9.15	7.40	7.40	8.60	7.45	8.00	0.74	7.75
	4	6.20	7.60	6.70	7.10	6.25	6.77	0.53	6.80
	5	5.20	4.70	4.90	5.95	4.70	5.09	0.47	5.01
60	3	9.95	9.20	9.60	10.05	8.25	9.41	0.65	9.30
	4	7.45	8.50	7.85	8.30	7.35	7.89	0.45	8.16
	5	6.15	5.40	5.70	6.70	5.60	5.91	0.47	6.01
70	3	12.40	10.55	11.25	11.55	10.05	11.11	0.88	10.85
	4	9.10	9.20	9.30	9.75	8.95	9.26	0.27	9.52
	5	7.50	6.15	6.85	7.85	6.75	7.02	0.60	7.01
80	3	12.90	11.65	12.50	13.65	12.25	12.59	0.67	12.40
	4	10.00	10.60	10.60	11.55	10.90	10.73	0.50	10.88
	5	7.90	7.20	8.00	9.35	8.60	8.21	0.72	8.01

Table 5.2: Measures on the teaching model loaded unsymmetrically (Fig. 5.4) taken by different students
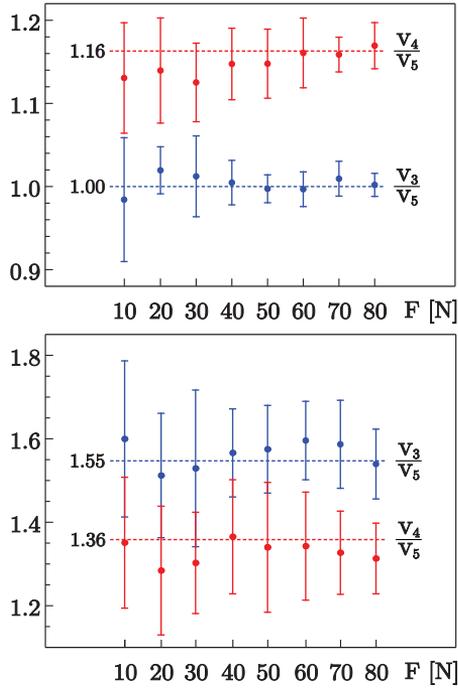
Figure 5.5: Ratios of mean values of the measured vertical displacement (dots) together with relative standard deviation (error bar) and theoretical value (dashed line) for different values of loading for symmetric (upper part) and unsymmetric (lower part) conditions.
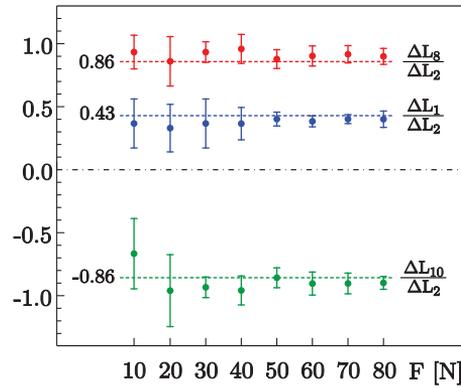
Figure 5.6: Ratios of mean values of elongation bars (dots) together with relative standard deviation (error bar) and theoretical value (dashed line) for different values of loading for unsymmetric condition.
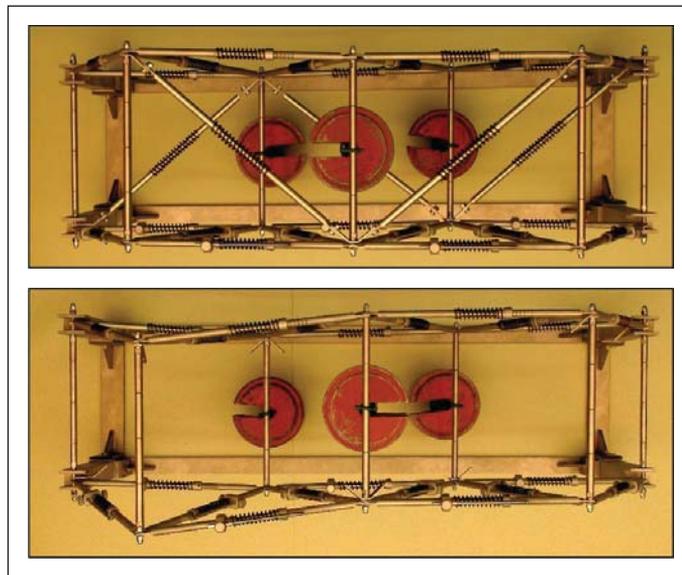
Figure 5.7: The effect of cross bracing: top view of the structure with (upper part) and without (lower part) bracing. A huge out-of-plane movement occurs (and is visible) when bracing is removed.

104

6

Stress concentration near stiff inclusions: validation of rigid inclusion model and boundary layers by means of photoelasticity

Photoelasticity is employed to investigate the stress state near stiff rectangular and rhombohedral inclusions embedded in a 'soft' elastic plate. Results show that the singular stress field predicted by the linear elastic solution for the rigid inclusion model can be generated in reality, with great accuracy, within a material. In particular, experiments: (i.) agree with the fact that the singularity is lower for obtuse than for acute inclusion angles; (ii.) show that the singularity is stronger in Mode II than in Mode I (differently from a notch); (iii.) validate the model of rigid quadrilateral inclusion; (iv.) for thin inclusions, show the presence of boundary layers deeply influencing the stress field, so that the limit case of rigid line inclusion is obtained in strong dependence on the inclusion's shape. The introduced experimental methodology opens the possibility of enhancing the design of thin reinforcement and of analyzing complex situations involving interaction between inclusions and defects.

6.1   Introduction

Experimental stress analysis near a crack or a void has been the subject of an intense research effort (see for instance Lim and Ravi-Chandar, 2007; 2009; Schubnel et al. 2011; Templeton et al. 2009), but the stress field near a rigid inclusion embedded in an elastic matrix, a fundamental problem in the design of composites, has surprisingly been left almost unexplored (Theocaris, 1975; Reedy and Guess, 2001) and has *never* been investigated via photoelasticity[1].

---

[1]Gdoutus (1982) reports plots of the fields that would result from photoelastic investigation of cusp inclusions, but does not report any experiment. Noselli et al. (2011) (see also Bigoni, 2012; Dal Corso et al. 2008) have only treated the case of a thin

Though the analytical determination of elastic fields around inclusions is a problem in principle solvable with existing methodologies (Movchan and Movchan, 1995; Muskhelishvili, 1953; Savin, 1961), detailed treatments are not available and the existing solutions (Chang and Conway, 1968; Evan-Iwanowski, 1956) lack mechanical interpretation, in the sense that it is not known if these predict stress fields observable in reality[2].

Moreover, from experimental point of view, questions arise whether the bonding between inclusion and matrix can be realized and can resist loading without detachment (which would introduce a crack) and if self-stresses can be reduced to negligible values. In this chapter we (i.) re-derive asymptotic and full-field solutions for rectangular and rhombohedral rigid inclusions (Section 6.2) and (ii.) compare these with photoelastic experiments (Section 6.3).

Photoelastic fringes obtained with a white circular polariscope are shown in Fig. 6.1 and indicate that the linear elastic solutions provide an excellent description of the elastic fields generated by inclusions up to a distance so close to the edges of the inclusions that fringes result unreadable (even with the aid of an optical microscope). By comparison of the photos shown in Fig. 6.1 with Fig. 1 of Noselli et al. (2010), it can be noted that the stress fields correctly tend to those relative to a rigid line inclusion (*stiffener*) when the aspect ratio of the inclusions grows, and that the stress fields very close to a thin inhomogeneity are substantially affected by boundary layers depending on the (rectangular or rhombohedral) shape.

6.2 Theoretical linear elastic fields near rigid polygonal inclusions

The stress/strain fields in a linear isotropic elastic matrix containing a rigid polygonal inclusion are obtained analytically through both an asymptotic approach and a full-field determination. Considering plane stress or strain conditions, the displacement components in the $x - y$ plane are

$$u_x = u_x(x, y), \qquad u_y = u_y(x, y), \tag{6.1}$$

corresponding to the following in-plane deformations $\varepsilon_{\alpha\beta}$ (α, $\beta = x, y$)

$$\varepsilon_{xx} = u_{x,x}, \qquad \varepsilon_{yy} = u_{y,y}, \qquad \varepsilon_{xy} = \frac{u_{x,y} + u_{y,x}}{2}, \tag{6.2}$$

---

line-inclusion.

[2]The experimental methodology introduced here for rigid inclusions can be of interest for the experimental investigation of the interaction between inclusions and defects, such as for instance cracks, for which analytical solutions are already available (for cracks, see Piccolroaz et al. 2012 a; b; Valentini et al. 1999).
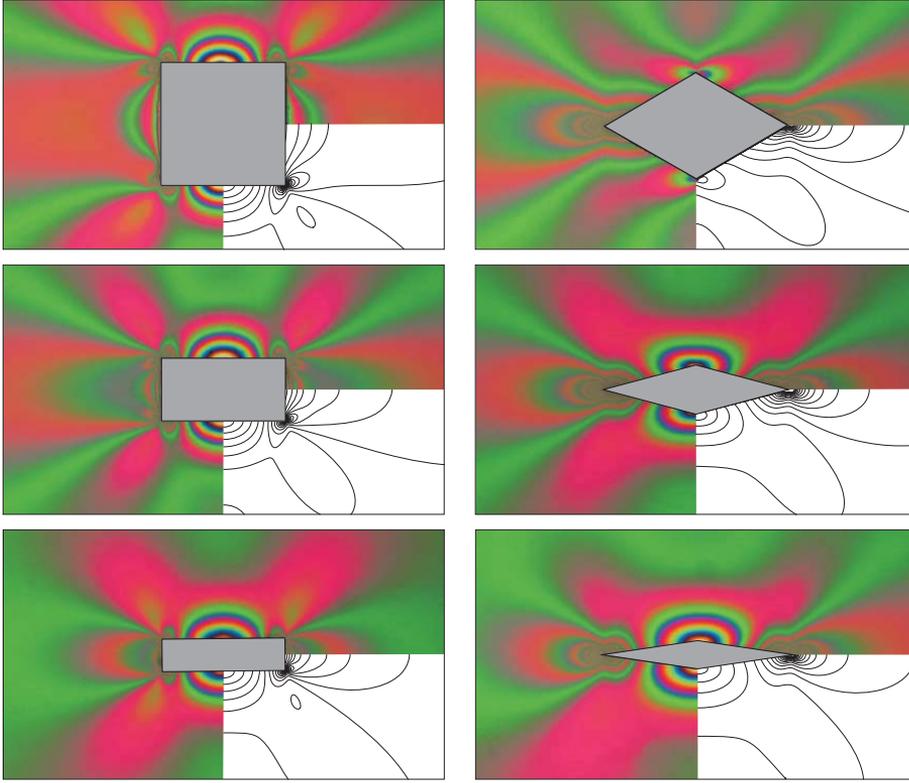
Figure 6.1: Photoelastic fringes revealing the stress field near stiff (made up of polycarbonate, Young modulus 2350 MPa) rectangular (large edge l_x =20 mm, edges aspect ratios 1, 1/2, 1/4) and rhombohedral (large axis l_x =30 mm, axis aspect ratios 2/15, 4/15, 9/15) inclusions embedded in an elastic matrix (a two-component epoxy resin, Young modulus 22 MPa, approximatively 100 times less stiff than the inclusions) and loaded with uniaxial tensile stress σ_{xx}^{∞} =0.28 MPa, compared to the elastic solution for rigid inclusions (in plane stress, with Poisson's ratio equal to 0.49).

which, for linear elastic isotropic behaviour, are related to the in the in-plane stress components $\sigma_{\alpha\beta}$ (α, β=x, y) via

$$\varepsilon_{xx} = \frac{(\kappa+1)\sigma_{xx} + (\kappa-3)\sigma_{yy}}{8\mu}, \qquad \varepsilon_{yy} = \frac{(\kappa+1)\sigma_{yy} + (\kappa-3)\sigma_{xx}}{8\mu}, \qquad \varepsilon_{xy} = \frac{\sigma_{xy}}{2\mu},$$

$$(6.3)$$

where μ represents the shear modulus and $\kappa \geq 1$ is equal to $3-4\nu$ for plane strain or $(3-\nu)/(1+\nu)$ for plane stress, where $\nu \in (-1, 1/2)$ is the Poisson's ratio. Finally, in the absence of body forces, the in-plane stresses satisfy the equilibrium equation (where repeated indices are summed)

$$\sigma_{\alpha\beta,\beta} = 0. \tag{6.4}$$

6.2.1 Asymptotic fields near the corner of a rigid wedge

Near the corner of a rigid wedge the mechanical fields may be approximated by their asymptotic expansions. With reference to the polar coordinates r, ϑ centered at the wedge corner and such that the elastic matrix occupies the region $\vartheta \in [-\alpha, \alpha]$ (while the semi-infinite rigid wedge lies in the remaining part of plane, Fig. 6.2), the Airy function $F(r, \vartheta)$, automatically satisfying the equilibrium equation (6.4), is defined as

$$\sigma_{rr} = \frac{1}{r}\left(F_{,r} + \frac{F_{,\vartheta\vartheta}}{r}\right), \qquad \sigma_{\vartheta\vartheta} = F_{,rr}, \qquad \sigma_{r\vartheta} = -\left(\frac{F_{,\vartheta}}{r}\right)_{,r}. \tag{6.5}$$

The following power-law form of the Airy function satisfies the kinematic compatibility conditions [Barber, 1993, his eqn (11.35)]

$$F(r, \vartheta) = r^{\gamma+2}\left[A_1 \cos(\gamma+2)\vartheta + A_2 \sin(\gamma+2)\vartheta + A_3 \cos\gamma\vartheta + A_4 \sin\gamma\vartheta\right], \tag{6.6}$$

and provides the in-plane stress components as

$$
\begin{aligned}
\sigma_{rr} &= -(\gamma+1)r^{\gamma}[A_1(\gamma+2)\cos(\gamma+2)\vartheta + A_2(\gamma+2)\sin(\gamma+2)\vartheta \\
&\quad + A_3(\gamma-2)\cos\gamma\vartheta + A_4(\gamma-2)\sin\gamma\vartheta], \\[2mm]
\sigma_{\vartheta\vartheta} &= (\gamma+2)(\gamma+1)r^{\gamma}[A_1\cos(\gamma+2)\vartheta + A_2\sin(\gamma+2)\vartheta \\
&\quad + A_3\cos\gamma\vartheta + A_4\sin\gamma\vartheta], \\[2mm]
\sigma_{r\vartheta} &= (\gamma+1)r^{\gamma}[A_1(\gamma+2)\sin(\gamma+2)\vartheta - A_2(\gamma+2)\cos(\gamma+2)\vartheta \\
&\quad + A_3\gamma\sin\gamma\vartheta - A_4\gamma\cos\gamma\vartheta],
\end{aligned}
\tag{6.7}
$$

where A_1, A_2 and A_3, A_4 are unknown constants defining the symmetric (Mode I) and antisymmetric (Mode II) contributions, respectively, while γ represents the unknown power of r for the stress and strain asymptotic fields, $\{\sigma_{\alpha\beta}, \varepsilon_{\alpha\beta}\} \sim r^{\gamma}$, with $\gamma \geq -1/2$.

Imposing the boundary displacement conditions $u_r(r, \pm\alpha) = u_\vartheta(r, \pm\alpha) = 0$ leads to two decoupled homogeneous systems, one for each Mode symmetry condition, so that non-trivial asymptotic fields are obtained when determinant of coefficient matrix is null, namely (Seweryn and Molski, 1996)

$$(\gamma + 1)\sin(2\alpha) - \kappa\sin(2\alpha(\gamma + 1)) = 0, \quad \text{Mode I};$$

$$(\gamma + 1)\sin(2\alpha) + \kappa\sin(2\alpha(\gamma + 1)) = 0, \quad \text{Mode II}.$$

(6.8)

Note that, in the limit $\kappa = 1$ (incompressible material under plane strain conditions), equations (6.8) are the same as those obtained for a notch, except that the loading Modes are switched. Furthermore, according to the so-called 'Dundurs correspondence' (Dundurs, 1989), when $\kappa = -1$ eqns (6.8) coincide with those corresponding to a notch.

The smallest negative value of the power $\gamma \geq -1/2$ for each loading Mode, satisfying eqn (6.8)$_1$ and (6.8)$_2$, represents the leading order term of the asymptotic expansion. These two values (one for Mode I and another for Mode II) are reported in Fig. 6.2 (left), for different values of κ, as functions of the semi-angle α and compared with the respective values for a void wedge, Fig. 6.2 (right).
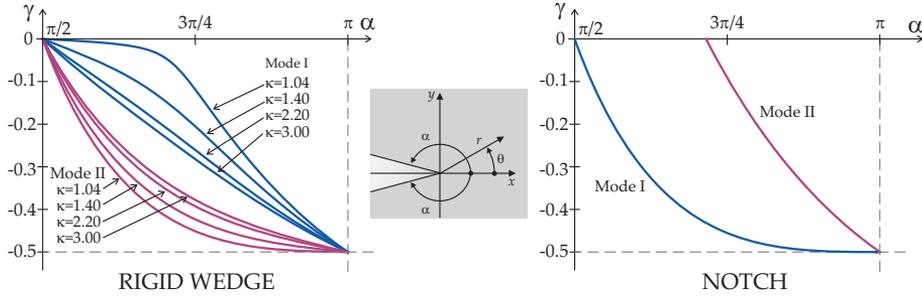
Figure 6.2: The higher singularity power γ for a rigid wedge (left, angle α is the semi-angle in the matrix enclosing the wedge) and for a notch (right, angle α is the semi-angle in the matrix enclosing the notch) under Mode I and Mode II loading and different values of κ.

For the rigid wedge, *similarly to the notch problem*:

- the singularity appears only when $\alpha > \pi/2$ and increases with the increase of α;

- a square root singularity ($\sigma_{\alpha\beta} \sim 1/\sqrt{r}$) appears for both mode I and II when α approaches π (corresponding to the rigid line inclusion model, see Noselli et al. 2010);

while, *differently from the notch problem*:

- the singularity depends on the Poisson's ratio ν through the parameter κ;

- the singularity under Mode II condition is stronger than that under Mode I; in particular, a weak singularity is developed under Mode I when, for plane strain deformation, a quasi-incompressible material (ν close to $1/2$) contains a rigid wedge with $\alpha \in [\frac{1}{2}, \frac{3}{4}]\pi$.

Since the intensity of singularity near a corner is strongly affected by the value of the angle α, it follows that the stress field close to a rectangular inclusion is substantially different to that close to a rhombohedral one. Therefore, strongly different boundary layers arise when a rectangular or a rhombohedral inclusion approaches the limit of line inclusion.

6.2.2 Full-field solution for a matrix containing a polygonal rigid inclusion

Solutions in 2D isotropic elasticity can be obtained using the method of complex potentials (Muskhelishvili, 1953), where the generic point (x, y) is referred to the complex variable $z = x + \mathrm{i}\,y$ (where i is the imaginary unit) and the mechanical fields are given in terms of complex potentials $\varphi(z)$ and $\psi(z)$ which can be computed from the boundary conditions.

In the case of non-circular inclusions, it is instrumental to introduce the complex variable ζ, related to the physical plane through $z = \omega(\zeta)$ with the conformal mapping function ω (such that the inclusion boundary becomes a unit circle in the ζ-plane, $\zeta = e^{\mathrm{i}\theta}$), so that the stress and displacement components are given as

$$
\begin{cases}
\sigma_{xx} + \sigma_{yy} = 4\mathrm{Re}\left[\dfrac{\varphi'(\zeta)}{\omega'(\zeta)}\right], \\[3mm]
\sigma_{yy} - \sigma_{xx} + 2\,\mathrm{i}\,\sigma_{xy} = 2\left[\dfrac{\psi'(\zeta)}{\omega'(\zeta)} + \dfrac{\overline{\omega(\zeta)}}{\omega'(\zeta)^3}\left[\varphi''(\zeta)\omega'(\zeta) - \varphi'(\zeta)\omega''(\zeta)\right]\right], \\[3mm]
2\mu(u_x + \mathrm{i}\,u_y) = \kappa\varphi(\zeta) - \dfrac{\omega(\zeta)}{\overline{\omega'(\zeta)}}\overline{\varphi'(\zeta)} - \overline{\psi(\zeta)}.
\end{cases}
\tag{6.9}
$$

The complex potentials are the sum of the unperturbed (homogeneous) solution and the perturbed (introduced by the inclusion) solution, so that, considering boundary conditions at infinity of constant stress at infinity with the only non-

null component σ_{xx}^{∞}, we may write

$$\varphi(\zeta) = \frac{\sigma_{xx}^{\infty}}{4}\omega(\zeta) + \varphi^{(p)}(\zeta), \qquad \psi(\zeta) = -\frac{\sigma_{xx}^{\infty}}{2}\omega(\zeta) + \psi^{(p)}(\zeta), \qquad (6.10)$$

where the perturbed potentials $\varphi^{(p)}(\zeta)$ and $\psi^{(p)}(\zeta)$ can be obtained by imposing the conditions on the inclusion boundary, which are defined on a unit circle and for a rigid inclusion[3] are

$$\kappa\varphi^{(p)}(\zeta) - \frac{\omega(\zeta)}{\overline{\omega'(\zeta)}}\overline{\varphi^{(p)'}(\zeta)} - \overline{\psi^{(p)}(\zeta)} = \frac{\sigma_{xx}^{\infty}}{2}\left(\frac{1-\kappa}{2}\omega(\zeta) - \overline{\omega(\zeta)}\right),$$
$$\text{for } \zeta = e^{\mathrm{i}\theta}, \ \theta \in [0, 2\pi]. \qquad (6.11)$$

In the case of n-polygonal shape inclusions the conformal mapping which maps the interior of the unit disk onto the region exterior to the inclusion is given by the Schwarz-Christoffel integral

$$\omega(\zeta) = Re^{i\alpha_0}\int_1^\zeta \prod_{j=1}^n \left(1 - \frac{s}{k_j}\right)^{1-\alpha_j} \frac{ds}{s^2} + k_0, \qquad (6.12)$$

where R, k_0, and α_0 are constants representing scaling, translation, and rotation of the inclusion, while k_j and α_j (j=1,..., n) are the pre-images of the j-th vertex in the ζ plane and the fraction of π of the j-th interior angle, respectively. In the following the translation and rotation parameters for the inclusion are taken null, $k_0 = \alpha_0 = 0$.

Assuming that the perturbed potentials are holomorphic inside the unit circle in the ζ-plane, $\varphi^{(p)}(\zeta)$ can be expressed through Laurent series

$$\varphi^{(p)}(\zeta) = R\,\sigma_{xx}^{\infty}\sum_{j=1}^\infty a_j\zeta^j, \qquad (6.13)$$

where a_j (j=1,2,3,...) are unknown complex constants. Furthermore, since the integral expression in eqn (6.12) cannot be computed as closed form for generic polygon, it is expedient to represent the conformal mapping as

$$\omega(\zeta) = R\left(\frac{1}{\zeta} + \sum_{j=1}^\infty d_j\zeta^j\right), \qquad (6.14)$$

where d_j (j=1,2,3,...) are complex constants.

---

[3]Eqn (6.11) holds when rigid-body displacements are excluded.

In order to obtain an approximation for the solution, the series expansions for $\omega(\zeta)$ and $\varphi^{(p)}(\zeta)$ are truncated at the M-th term. Through Cauchy integral theorem, integration over the inclusion boundary of eqn (6.11) yields a linear system for the M unknown complex constants a_j, functions of the M constants d_j, obtained through series expansion of eqn. (6.12). Once the expression for $\varphi^{(p)}(\zeta)$ is obtained, the integral over the inclusion boundary of the conjugate version of the boundary condition (6.11) is used to approximate $\psi^{(p)}(\zeta)$, resulting as

$$\psi^{(p)}(\zeta) = \frac{\sum_{j=1}^{M+2} b_j \zeta^{j-1}}{\sum_{j=1}^{M+2} c_j \zeta^{j-1}} \; R \, \sigma_{xx}^\infty \, \zeta. \tag{6.15}$$

Rectangle   In this case the angle fractions are $\alpha_j = 1/2$ ($j{=}1,...,\,4$) while the pre-images are

$$k_1 = e^{\eta\pi\mathrm{i}}, \qquad k_2 = e^{-\eta\pi\mathrm{i}}, \qquad k_3 = e^{(1+\eta)\pi\mathrm{i}}, \qquad k_4 = e^{(1-\eta)\pi\mathrm{i}}, \tag{6.16}$$

where η (likewise R) is a parameter function of the rectangle aspect ratio l_y/l_x, with the inclusion edges l_x and l_y. Parameters η and R are given in Tab. 6.2.2 for the aspect ratios considered here.

l_y/l_x	**1**	**1/2**	**1/4**
η	0.2500	0.2003	0.1548
R/l_x	0.5902	0.4374	0.3539

Table 6.1: Parameters η and R for the considered aspect ratios l_y/l_x of rectangular rigid inclusions.

The conformal mapping function and perturbed potentials obtained in the

case of rectangle with $l_y/l_x = 1/4$ are reported for $M{=}15$:

$$\omega(\zeta) = \left(\frac{1}{\zeta} + 0.5633\zeta - 0.1138\zeta^3 - 0.0385\zeta^5 - 0.0071\zeta^7 + 0.0042\zeta^9 + \right.$$
$$\left. + 0.0052\zeta^{11} + 0.0022\zeta^{13} - 0.0006\zeta^{15}\right)R,$$

$$\varphi^{(p)}(\zeta) = \left(-0.2420 - 0.0264\zeta^2 - 0.0071\zeta^4 + 0.0003\zeta^6 + 0.0020\zeta^8 + \right.$$
$$\left. + 0.0012\zeta^{10} + 0.0002\zeta^{12} - 0.0001\zeta^{14}\right)R\sigma_{xx}^\infty\,\zeta,$$

$$\psi^{(p)}(\zeta) = \left(-2.4454 - 54.9115\zeta^2 + 6.4081\zeta^4 + 5.5545\zeta^6 + 3.4073\zeta^8 + \right.$$
$$+ 0.6051\zeta^{10} - 1.3007\zeta^{12} - 1.0545\zeta^{14} + 0.2727\zeta^{16}\big)R\sigma_{xx}^\infty\,\zeta/\big(109.8986 -$$
$$- 61.9012\zeta^2 + 37.5162\zeta^4 + 21.1312\zeta^6 + 5.4989\zeta^8 - 4.1163\zeta^{10} -$$
$$- 6.2272\zeta^{12} - 3.1597\zeta^{14} + \zeta^{16}\big).$$

$$(6.17)$$

Rhombus In this case the pre-images are

$$k_1 = 1, \qquad k_2 = \mathrm{i}, \qquad k_3 = -1, \qquad k_4 = -\mathrm{i}, \qquad\qquad (6.18)$$

while the angle fractions are

$$\alpha_1 = \alpha_3 = \frac{2}{\pi}\arctan\left(l_y/l_x\right), \qquad \alpha_2 = \alpha_4 = 1 - \alpha_1. \qquad (6.19)$$

The scaling parameter R is reported in Tab. 6.2.2 for the rhombus aspect ratios l_y/l_x considered here, where l_x and l_y are the inclusion axis.

l_y/l_x	**9/15**	**4/15**	**2/15**
R/l_x	0.3389	0.2841	0.2659

Table 6.2: Parameter R for the considered aspect ratios l_y/l_x of rhombohedral rigid inclusions.

The conformal mapping function and perturbed potentials obtained in the case of rhombus with $l_y/l_x = 2/15$ are reported for $M{=}15$:

$$
\begin{aligned}
\omega(\zeta) = \ & (\frac{1}{\zeta} + 0.8312\zeta + 0.0515\zeta^3 - 0.0086\zeta^5 + 0.0068\zeta^7 - 0.0028\zeta^9 + \\
& + 0.0025\zeta^{11} - 0.0013\zeta^{13} + 0.0013\zeta^{15})R,
\end{aligned}
$$

$$
\begin{aligned}
\varphi^{(p)}(\zeta) = \ & \big(- 0.1628 + 0.0071\zeta^2 + 0.0001\zeta^4 + 0.0009\zeta^6 + 0.0001\zeta^8 + \\
& + 0.0003\zeta^{10} + 0.0001\zeta^{12} + 0.0002\zeta^{14} \big)\, R\,\sigma_{xx}^\infty\,\zeta,
\end{aligned}
$$

$$
\begin{aligned}
\psi^{(p)}(\zeta) = \ & \big(8.1122 + 28.1115\zeta^2 + 1.8150\zeta^4 - 0.6928\zeta^6 + 0.4105\zeta^8 - \\
& - 0.4451\zeta^{10} + 0.1665\zeta^{12} - 0.3417\zeta^{14} + 0.2727\zeta^{16} \big)R\,\sigma_{xx}^\infty\,\zeta/\big(- 53.0727 + \\
& + 44.1156\zeta^2 + 8.2012\zeta^4 - 2.2724\zeta^6 + 2.5225\zeta^8 - 1.3283\zeta^{10} + \\
& + 1.4453\zeta^{12} - 0.9307\zeta^{14} + \zeta^{16} \big).
\end{aligned}
$$

$$(6.20)$$

6.3 Photoelastic elastic fields near rigid polygonal inclusions

Photoelastic experiments with linear and circular polariscope (with quarter-wave retarders for 560nm) at white and monochromatic light[4] have been performed on twelve two-component resin (Translux D180 from Axon; mixing ratio by weight: hardener 95, resin 100, accelerator 1.5; the elastic modulus of the resulting matrix has been measured by us to be 22 MPa, while the Poisson's ratio has been indirectly estimated equal to 0.49) samples containing stiff inclusions, obtained with a solid polycarbonate 3 mm thick sheet (clear 2099 Makrolon UV) from Bayer with elastic modulus equal to 2350 MPa, approximatively 100 times stiffer than the matrix.

Samples have been prepared by pouring the resin (after deaeration, obtained through a 30 minutes exposition at a pressure of -1 bar) into a teflon mold (340 mm × 120 mm × 10 mm) to obtain 3±0.05 mm thick samples. The resin has been kept for 36 hours at constant temperature of 29 °C and humidity of 48%. After mold extraction, samples have been cut to be 320 mm × 110 mm × 3 mm, containing rectangular inclusions with wedges 20 mm × {20; 10; 5} mm and rhombohedral inclusions with axis 30 mm × {18; 8; 4} mm.

---

[4]The polariscope (dark field arrangement and equipped with a white and sodium vapor lightbox at $\lambda = 589.3$nm, purchased from Tiedemann & Betz) has been designed by us and manufactured at the University of Trento, see http://ssmg.unitn.it/ for a detailed description of the apparatus.

Photos have been taken with a Nikon D200 digital camera, equipped with a AF-S micro Nikkor (105 mm, 1:2.8G ED) lens and with a AF-S micro Nikkor (70Ű180 mm, 1:4.5Ű5.6 D) lens for details. Monitoring with a thermocouple connected to a Xplorer GLX Pasco©, temperature near the samples during experiments has been found to lie around 22.5° C, without sensible oscillations. Near-tip fringes have been captured with a Nikon SMZ800 stereozoom microscope equipped with Nikon Plan Apo 0.5x objective and a Nikon DS-Fi1 high-definition color camera head.

The uniaxial stress experiments have been performed at controlled vertical load applied in discrete steps, increasing from 0 to a maximum load of 90 N, except for thin rectangular and rhombohedral inclusions, where the maximum load has been 70 N and 78 N, respectively (loads have been reduced for thin inclusions to prevent failure at the vertex tips). In all cases an additional load of 3.4N has been applied, corresponding to the grasp weight, so that maximum nominal far-field stress of 0.28 MPa has been applied (0.22 MPa and 0.25 MPa for the thin inclusions).

Data have been acquired after 5 minutes from the load application time in order to damp down the largest amount of viscous deformation, noticed as a settlement of the fringes, which follows displacement stabilization. Releasing the applied load after the maximum amount, all the samples at rest showed no perceivably residual stresses in the whole specimen.

Comparison between analytical solutions and experiments is possible through matching of the isochromatic fringe order N, which (in linear photoelasticity)[5] is given by (Frocht, 1965)

$$N = \frac{t}{f_\sigma} \Delta\sigma, \qquad (6.21)$$

where t is the sample thickness, $\Delta\sigma = \sigma_I - \sigma_{II}$ is the in-plane principal stress difference, and f_σ is the material fringe constant, measured by us to be equal to 0.203 N/mm (using the so-called 'Tardy compensation procedure', see Dally and Riley, 1965). These comparisons are reported in Figs. 6.3 and 6.4, where the full-field solution obtained in Section 6.2.2 has been used under plane stress assumption and $\nu = 0.49$. This assumption is consistent with the reduced thickness of the employed samples, much thinner than the thickness of the samples employed by Noselli et al. (2010), who have compared photoelastic experiments considering plane strain.

The results show an excellent agreement between theoretical predictions and photoelastic measures, with some discrepancies near the contact with the in-

---

[5]Differently from Noselli et al. (2010), a constant value for the fringe material parameter f_σ has been considered here since non constant values were found not to introduce significant improvements.

clusions where, the plane stress assumption becomes questionable due to the out-of-plane constraint imposed by the contact with the rigid phase. Moreover, some microscopical view (at $31.5\times$) near the vertices of inclusion, shown in the insets of Figs. 6.3 and 6.4, reveals that the stress fields are in good agreement even close to the corners, where a strong stress magnification is evidenced near acute corners, while no singularity is observed near obtuse corners.

The near-corner stress magnifications and comparisons with the full field solution (evaluated with $M = 15$) are provided in Fig. 6.5, where the in-plane stress difference (divided by the far field stress) is plotted along the major axis of the thin and thick rhombohedral inclusions (Fig. 6.5, upper and central parts, respectively) and along a line tangent to the corner (and inclined at an angle $\pi/6$) of the rectangular thin inclusion. In particular, magnification factors of 5.3 (upper part, $\alpha = 23\pi/24$), 3.8 (central part, $\alpha = 5\pi/6$), and 2.7 (lower part, $\alpha = 3\pi/4$) have been measured.

It is interesting to note that according to the theoretical prediction (Section 6.2.1, Fig. 6.2), the singularity is stronger for acute than for obtuse inclusion's angles and that the stress fields tend to those corresponding to a zero-thickness rigid inclusion (a 'stiffener', see Noselli et al. 2010), when the rectangular (Fig. 6.3) and the rhombohedral (Fig. 6.4) inclusions become narrow (from the upper part to the lower part of the figures).

According to results shown in Fig. 6.2, we observe from Figs. 6.3, 6.4, and 6.5 the following.

- For Mode I loading the stress concentration becomes weak for angles α within $[\pi/2, 3\pi/4]$, see Fig. 6.4 (compare the fields near the two different vertices).

- For Mode II loading the stress concentration is much stronger than for Mode I. Stress concentrations generated for mixed-mode at an angle $\alpha = 3\pi/4$ are visible in Fig. 6.3 near the corners of rectangular inclusions. These concentrations are visibly stronger than those near the wider corner in Fig. 6.4 (upper part), which is subject to Mode I;

- The stress fields evidence boundary layers close to the inhomogeneity, see lower part of Figs. 6.3 and 6.4: These boundary layers are crucial in defining detachment mechanisms and failure modes. Therefore, the shape of a thin inclusion has an evident impact in limiting the working stress of a mechanical piece in which it is embedded. This conclusion has implications in the design of material with thin and stiff reinforcements, which can be enhanced through an optimization of the inclusion shape.
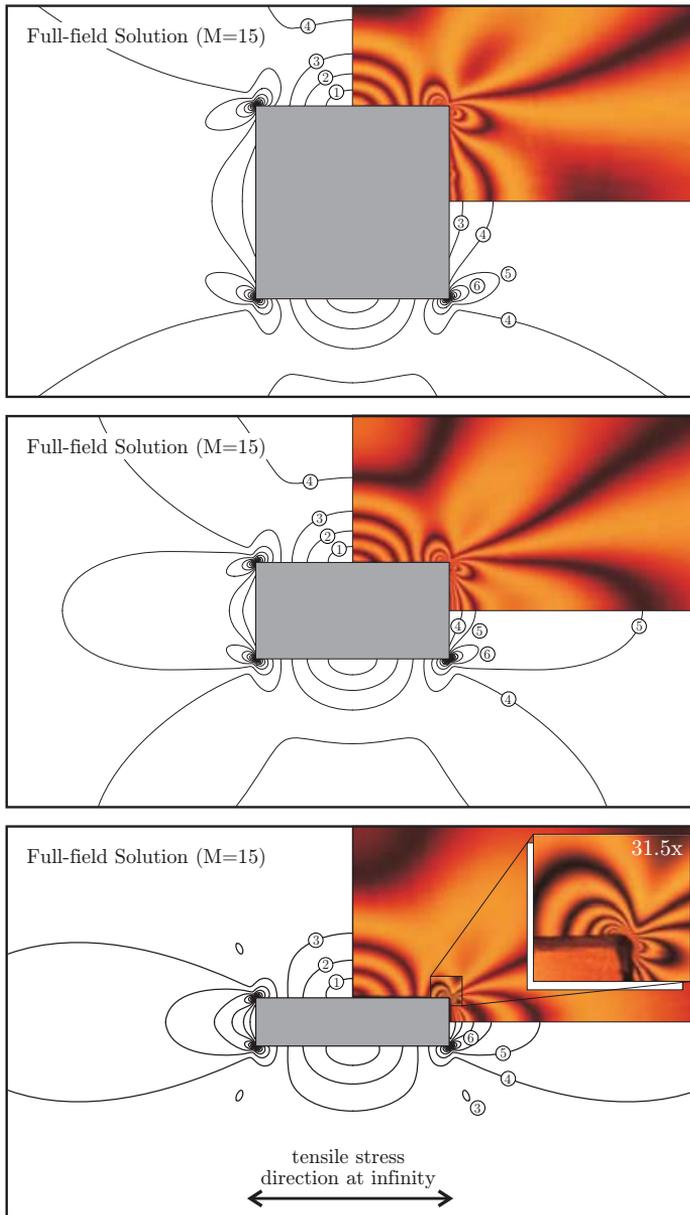
Figure 6.3: Monochromatic photoelastic fringes (with order number enclosed in a circle) revealing the in-plane principal stress difference field near stiff rectangular inclusions (made up of polycarbonate, with large edge $l_x = 20$ mm and aspect ratios $\{1; 1/2; 1/4\}$) embedded in an elastic matrix (a two-component 'soft' epoxy resin, approximatively 100 times less stiff than the inclusion) compared to the elastic solution for rigid inclusions (in plane stress, with Poisson's ratio equal to 0.49), at uniaxial stress $\sigma_{xx}^\infty = 0.28$ MPa (0.22 MPa for the lower part).
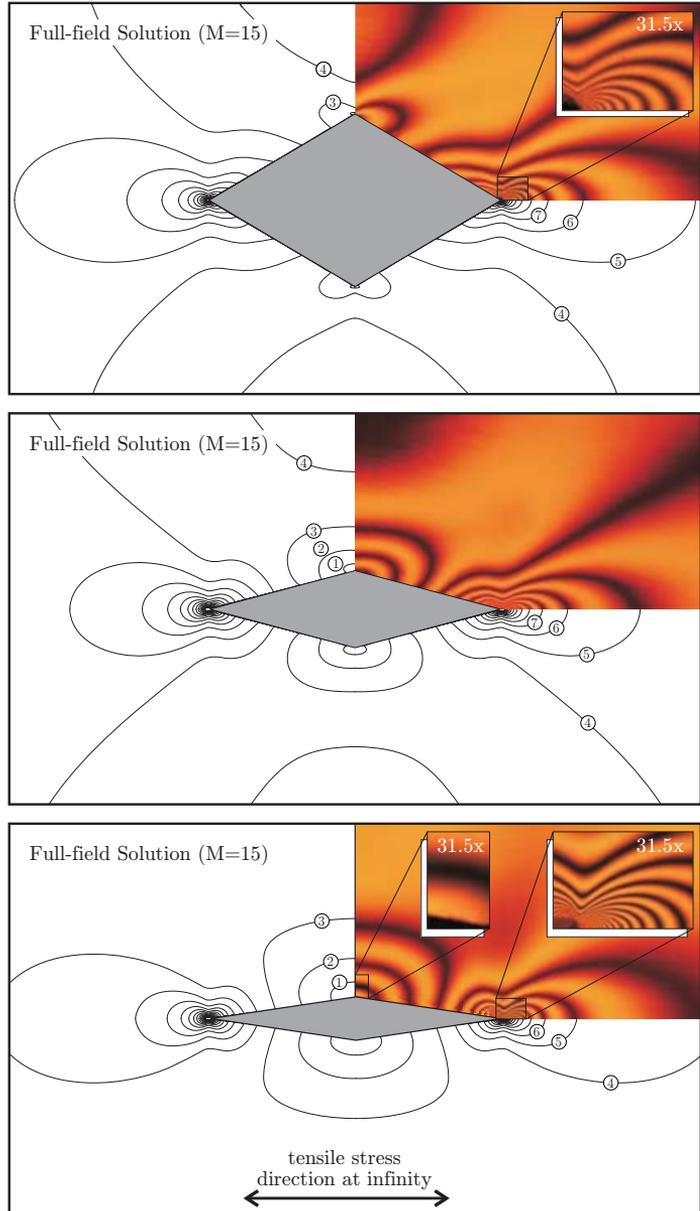
Figure 6.4: Monochromatic photoelastic fringes (with order number enclosed in a circle) revealing the in-plane principal stress difference field near stiff rhombohedral inclusions (made up of polycarbonate, with large axes 30 mm and axis aspect ratios {9/15; 4/15; 2/15}) embedded in an elastic matrix (a two-component 'soft' epoxy resin, approximatively 100 times less stiff than the inclusion) compared to the elastic solution for rigid inclusions (in plane stress, with Poisson's ratio equal to 0.49), at uniaxial stress $\sigma_{xx}^\infty = 0.28$ MPa (0.25 MPa for the lower part).
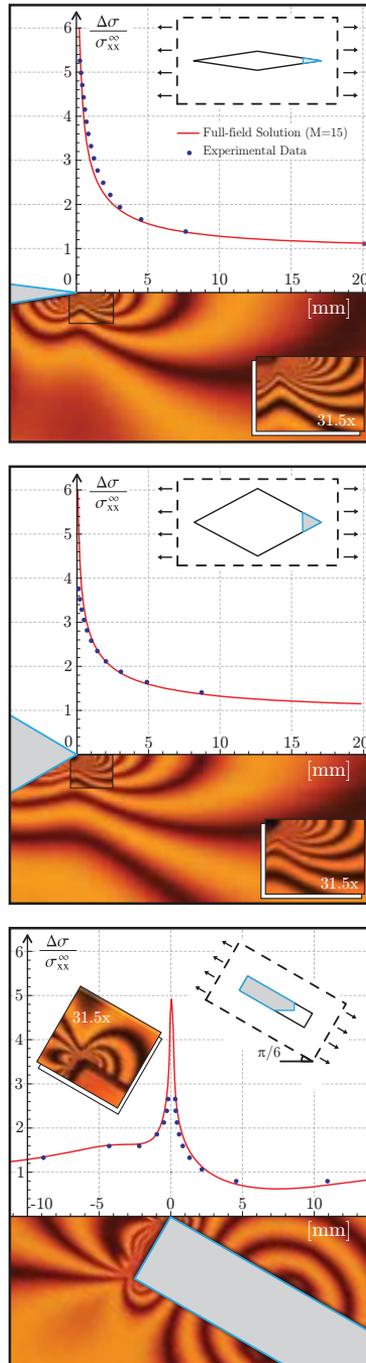
Figure 6.5: Near-corner stress magnification (in-plane stress difference divided by the far field stress) for rhombohedral (upper and central parts, respectively $\alpha = 23\pi/24$ and $\alpha = 5\pi/6$) and rectangular (lower part, $\alpha = 3\pi/4$) rigid inclusions. Experimental results are compared with the full-field elastic solution, evaluated with $M = 15$. Magnification factors of 5.3 (upper part), 3.8 (central part), and 2.7 (lower part) are visible.

7

Conclusion

New phenomena opening important perspectives in the design of structures have been shown and experimental evidence of 'classical' features in elasticity has been provided. Our results can be summarized as follows:

- We have theoretically proven and fully experimentally confirmed that elastic structures can be designed and practically realized in which bifurcation can occur with tensile dead loading (Chapter 1). In these structures no parts subject to compression are present. This finding is directly linked to the presence of a junction allowing only for relative sliding between two parts of the mechanical system. These results open completely new and unexpected perspectives, related for instance to the control of the propagation of mechanical waves and to the understanding of certain failure modes within solid materials.

- Effects related to the curvature and the shape of the constraint profile on which an end of a structure has to slide have been shown to be important on bifurcation and instability (Chapter 2). In particular, we have found possibility of buckling both in tension and compression and multiple buckling loads, as for instance in the case of a one-degree-of-freedom structure evidencing two critical loads. Moreover, we have shown that the introduction on a curved constraint profile of an elastic, torsional spring strongly affects the post-critical behaviour of the system and may lead to multiple equilibrium configurations, corresponding to an external force of zero magnitude. Our experiments have confirmed that these effects can be designed to occur in real structural prototypes, so that new possibilities are opened in exploiting simple deformation mechanisms to obtain flexible mechanical systems.

- Eshelbian forces are related to the change in configuration of a mechanical system. We have shown that simple elastic structures can be designed to give evidence to these forces, that can both be calculated and experimentally detected (Chapter 3).

- A number of unexpected features can be observed in the bifurcation and instability behaviour of elastic systems containing elements capable of devel-

oping Eshelby-like forces, as for instance a sliding sleeve. The Eshelby-like force explains surprising equilibrium configurations and concurs in determining restabilization of the straight configuration (Chapter 4).

- A simple physical model has been shown to effectively facilitate the understanding of the linear elastic behaviour of truss structures (Chapter 5). These are elementary structural forms crucial to the understanding of several conceptual models employed in micro- and nano-technologies, for example, crystal lattices and ultralight nanomaterials, and also in biology, for instance, protein materials.

- Photoelastic experimental investigations have been presented showing that the stress field near a stiff inclusion embedded in a soft matrix material can be effectively calculated by employing the model of rigid inclusion embedded in a linear elastic isotropic solid (Chapter 6). The results provide also the experimental evidence of boundary layers, depending on the inhomogeneity shape, which affect the stress fields and therefore define detachment mechanisms and failure modes. Furthermore, the presented methodology paves the way to the experimental stress analysis of more complex situations, for instance involving interaction between cracks or pores and inclusions.

Bibliography

[1] Balabukh, L.I., Vulfson, M.N., Mukoseev, B.V. and Panovko, Ya. G. (1970). On work done by reaction forces of moving supports. In: *Research on Theory of Constructions* **18**, 190–200, Moscow.

[2] Barber, J.R. (1993) *Elasticity*, Kluwer.

[3] D. Bigoni (2012) *Nonlinear Solid Mechanics. Bifurcation Theory and Material Instability*. Cambridge University Press.

[4] Bigoni, D. Dal Corso, F. Bosi, F. Misseroni, D. (2013) Eshelby-like forces acting on elastic structures: theoretical and experimental proof. *Submitted*, http://arxiv.org/abs/1309.2565.

[5] Bigoni, D. and Deseri, L. (2011) *Recent Progress in the Mechanics of Defects*, Springer.

[6] Bigoni, D., Gei, M. and Movchan, A.B. (2008) Dynamics of a prestressed stiff layer on an elastic half space: filtering and band gap characteristics of periodic structural models derived from long-wave asymptotics. *J. Mech. Phys. Solids*, **56**, 2494-2520.

[7] Bigoni, B., Misseroni, D., Noselli, G., and Zaccaria, D. (2012) Effects of the constraint's curvature on structural instability: tensile buckling and multiple bifurcations. *Proc. R. Soc.* A, **468** (2144), 2191–2209.

[8] Bigoni, D. and Noselli, G. (2011) Experimental evidence of flutter and divergence instabilities induced by dry friction. *J. Mech. Phys. Solids*, **59** (10), 2208–2226.

[9] Byrd, P.F and Friedman, M.D. (1971) *Handbook of elliptic integrals for engineers and scientists*. Springer-Verlag.

[10] Broman, A. (1970). *Introduction to Partial Differential Equations: From Fourier Series to Boundary-Value Problems*. Dover.

[11] Brown A.A.D. (1981) *Mechanical springs*. Oxford University Press.

[12] Buehler M.J., Yung Y.C. (2009) Deformation and failure of protein materials in physiologically extreme conditions and disease. *Nature Materials*, **8**, 175-188.

[13] Chang and Conway (1968) A parametric study of the complex variable method for analyzing the stresses in an infinite plate containing a rigid rectangular inclusion. *Int. J. Solid Struct.*, **4** (11), 1057–66.

[14] Charlton, T.M. (1966) *Model analysis of plane structures*. Pergamon Press.

[15] Courant, R. and Hilbert, D. (1953) *Methods of Mathematical Physics*, Wiley.

[16] Cross, H. and Morgan, N.D. (1932) *Continuous frames of reinforced concrete*, J. Wiley & Sons.

[17] Dal Corso, F. and Bigoni, D. (2009) The interactions between shear bands and rigid lamellar inclusions in a ductile metal matrix. *Proc. R. Soc. A*, **465**, 143–163.

[18] Dal Corso, F., Bigoni, D. and Gei, M. (2008) The stress concentration near a rigid line inclusion in a prestressed, elastic material. Part I. Full field solution and asymptotics. *J. Mech. Phys. Solids*, **56**, 815-838.

[19] Dally, J.W. and Riley W.F. (1965) *Experimental stress analysis*. McGraw-Hill.

[20] D'Arcy Thompson, W. (1917) *On Growth and Form*. Cambridge University Press.

[21] Dascalu, C. Maugin G.A., Stolz, C. (2010) *Defect and Material Mechanics*, Springer.

[22] O. Doare and S. Michelin (2011) Piezoelectric coupling in energy-harvesting fluttering flexible plates: linear stability analysis and conversion efficiency. *J. Fluid. Struct.*, **27** (8), 1357–1375.

[23] Dowling, P.J. and Owens, G.W. (1978) Structural model testing of a rising sector flood gate. *Thames Barrier Design Conference Proceedings*, 117-123.

[24] Dundurs, J. (1989) Cavities vis-a-vis rigid inclusions and some related general results in plane elasticity. *J. Appl. Mech.*, **56**, 786-790.

[25] I. Elishakoff (2005) Controversy associated with the so-called 'follower force': critical overview. *Appl. Mech. Rev.*, **58** (2), 117–142.

[26] Eshelby JD (1951) The force on an elastic singularity. *Phil. Trans. Roy. Soc. London A*, **244**, 87–112.

124

[27] Eshelby JD (1956) The continuum theory of lattice defects. In: *Progress in Solid State Physics 3* (eds. F. Seitz and D. Turnbull) 79–144, Academic Press, New York.

[28] Eshelby JD (1970) Energy relations and the energy-momentum tensor in continuum mechanics, In: *Inelastic Behaviour of Solids* (eds. M. Kanninien, W. Adler, A. Rosenfield, and R. Jaffee), 77–115, McGraw-Hill, New York.

[29] Eshelby JD (1975) The elastic energy-momentum tensor, *J. Elasticity* , **5**, 321–335.

[30] Evan-Iwanowski, R.M. (1956) Stress solutions for an infinite plate with triangular inlay. *J. Appl. Mech.* , **23**, 336.

[31] Feodosyev, V.I. *Selected Problems and Questions in Strength of Materials.* MIR, Moscow, 1977.

[32] Frocht, M.M. (1965) *Photoelasticity.* J. Wiley and Sons, London.

[33] Gajewski, A. and Palej, R. (1974) Stability and shape optimization of an elastically clamped bar under tension (in Polish). *Rozprawy Inzynierskie - Engineering Transactions*, **22**, 265-279.

[34] Gáspár, Zs. (1984) Buckling model for a degenerated case. *News Letter of the Technical University of Budapest*, **4**, pp. 5Ű8.

[35] Gdoutus, E.E. (1982) Photoelastic analysis of the stress field around cuspidal points of rigid inclusions. *J. Appl. Mech.* , **49**, 236-238.

[36] Gei, M., Movchan, A.B. and Bigoni, D. (2009) Band-gap shift and defect-induced annihilation in prestressed elastic structures. *J. Appl. Phys*, **105**, 063507.

[37] Godden, W.G. (1962) Demonstration models for teaching structural mechanics. *Eng. Experiment Station* Circular No. 78, University of Illinois.

[38] Gurtin ME (2000) *Configurational forces as basic concept of continuum physics.* Springer, Berlin, New York, Heidelberg.

[39] Hilson, B. (1972) *Basic structural bahaviour via models.* J. Wiley & Sons, New York.

[40] Kienzler, R. and Herrmann, G. (2000) *Mechanics in Material Space.* Springer, New York, Berlin, Heidelberg.

[41] O.N. Kirillov and F. Verhulst (2010) Paradoxes of dissipation-induced destabilization or who opened Whitney's umbrella? *Z. Angew. Math. Mech.*, **90** (6), 462–488.

125

[42] W.T. Koiter (1996) Unrealistic follower forces. *J. Sound and Vibration*, **194** (4), 636–638.

[43] Lamb, H. (1928) *Statics.* Cambridge University Press.

[44] Lim, J. and Ravi-Chandar K. (2007) Photomechanics in dynamic fracture and friction studies. *Strain*, **43**, 151Ű-165.

[45] Lim, J. and Ravi-Chandar, K. (2009) Dynamic Measurement of Two Dimensional Stress Components in Birefringent Materials. *Exper. Mech.*, **49**, 403-416.

[46] Love, A.E.H. (1927) *A treatise on the mathematical theory of elasicity.* Cambridge University Press.

[47] Majidi, C. (2007) Remarks on formulating an adhesion problem using Euler's elastica (draft). *Mec. Res. Comm.* , **34**, 85-90.

[48] Majidi, C., O'Reilly, O.M., Williams, J.A. (2012) On the stability of a rod adhering to a rigid surface: Shear-induced stable adhesion and the instability of peeling. *J. Mech. Phys. Solids*, **60**, 827–843.

[49] Maugin, G.A. (1993) *Material Inhomogeneities in Elasticity*, Chapman and Hall, London.

[50] Maugin G.A., (2011) *Configurational forces: Thermodynamics, physics, mathematics and numerics*, Chapman & Hall, CRC -Taylor and Francis, New York.

[51] Movchan, A.B. and Movchan, N.V. (1995) *Mathematical Modeling of Solids with Nonregular Boundaries*, CRC Press.

[52] Muskhelishvili, N.I. (1953) *Some Basic Problems of the Mathematical Theory of Elasticity.* P. Nordhoff Ltd., Groningen.

[53] Noselli, G., Dal Corso, F. and Bigoni, D. (2010). The stress intensity near a stiffener disclosed by photoelasticity. *Int. J. Fract.*, **166**, 91–103.

[54] J.T. Oden and J.A.C. Martins (1985) Models and computational methods for dynamic friction phenomena. *Comput. Meth. Appl. Mech. Engrg.*, **52** (1–3), 527–634.

[55] Piccolroaz, A., Mishuris, G., Movchan, A., and Movchan, N. (2012) Perturbation analysis of Mode III interfacial cracks advancing in a dilute heterogeneous material. *Int. J. Solid Struct.*, **49**, 244-255.

[56] Piccolroaz, A., Mishuris, G., Movchan, A., and Movchan, N. (2012) Mode III crack propagation in a bimaterial plane driven by a channel of small line defects. *Comput. Materials Sci.*, **64**, 239-243.

126

[57] Pippard, A.J.S. (1947) *The experimental study of structures.* Edward Arnold & Co, London.

[58] Reedy, E.D. and Guess, T.R. (2001) Rigid square inclusion embedded within an epoxy disk: asymptotic stress analysis. *Int. J. Solid Struct.*, **38**, 1281-1293.

[59] Savin, G.N. (1961) *Stress concentration around holes.* Pergamon Press.

[60] Schaedler, TA, Jacobsen, AJ, Torrents, A, Sorensen, AE, Lian, J, Greer, JR, Valdevit, L, Carter, WB (2011) Ultralight Metallic Microlattices. *Science*, **334**, pp. 962-965.

[61] Schubnel, A., Nielsen, S., Taddeucci, J., Vinciguerra., S. and Rao, S. (2011) Photo-acoustic study of subshear and supershear ruptures in the laboratory, *Earth Planetary Sci. Letters* **308**, 424-432.

[62] Seweryn, A., Molski, K. (1996) Elastic stress singularities and corresponding generalized stress intensity factors for angular corners under various boundary conditions. *Eng. Fract. Mech.*, **55**, 529–556.

[63] Y. Sugiyama, K. Katayama and S. Kinoi (1995) Flutter of a cantilevered column under rocket thrust. *J. Aerospace Eng.*, **8** (1), 9–15.

[64] Tarnai, J. (1980). Destabilizing effect of additional restraint on elastic bar structures. *Int. J. Mech. Sci.*, **22**, 379–390.

[65] Temme, N.M. (1996) *Special functions.* John Wiley and Sons, New York.

[66] Templeton, E. L., Baudet, A., Bhat, H.S., Dmowska, R., Rice, J.R., Rosakis, A.J. and Rousseau, C.-E. (2009), Finite element simulations of dynamic shear rupture experiments and dynamic path selection along kinked and branched faults, *J. Geophys. Res.*, **114**, B08304.

[67] Theocaris, P.S. (1975) Stress and displacement singularities near corners. *J. Appl. Math. Phys. (ZAMP)*, **26**, 77-98.

[68] Timoshenko, S.P. and Gere, J.M. (1961) *Theory of elastic stability.* McGraw-Hill, New York.

[69] M. Valentini, S.K. Serkov, D. Bigoni and A.B. Movchan (1999) Crack propagation in a brittle elastic material with defects. *J. Appl. Mech.* **66**, 79-86.

[70] van Brunt, B. (2005) *The calculus of variations.* Springer.

[71] Wahl, A.M. (1963) *Mechanical springs*, McGraw-Hill.

[72] Ziegler, H. (1977) *Principles of structural stability.* Birkäuser Verlag.

[73] Zyczkowski, M. (1991) *Strength of structural elements.* Elsevier.

[74] Zaccaria, D., Bigoni, D., Noselli, G. and Misseroni, D. (2011) Structures buckling under tensile dead load. *Proc. R. Soc. A*, 2011, **467**, 1686-1700.